Faculty of Sciences
Department of Physics and Astronomy

Search for Scalar Top Quark Partners and Parton Shower Tuning in Modelling Top Quark Pairs

By

Nicolas Bulté

Promotor: Dr. Efe Yazgan

A thesis presented for the degree of
Master of Science in Physics and Astronomy

June 2016

Acknowledgements

To start with, I would like to express my gratitude towards Prof. Dirk Ryckbosch for his efforts into bringing me towards the point where I finalise my studies. Five years ago, when I was unsure whether physics was a good fit for me, he told me that all it takes is a decent dose of enthusiasm and motivation. Bearing this in mind I took on the challenge and ended up in my final year, writing a thesis within the field of elementary particle physics. I was given the unique opportunity to stay and work at CERN gaining valuable skills and experience, from which I will be able to profit from for the rest of my life.

Further, I want to thank Prof. Didar Dobur for her endless patience and efforts into teaching me how experimental particle physics is conducted in practice. Also for the many hours she spent explaining me difficult concepts, providing me with feedback and learning me how to perform better as an experimental physicist.

Next, I want to thank Dr. Efe Yazgan for always being there when I was in need of assistance, for his thorough help, feedback and guidance and for making my research count. He taught me how scientific research is conducted within an international setting which made writing this thesis an invaluable experience.

Another big thanks go to Michael Sigamani, Ward Van Driessche and Antoine Pingault for taking me in their office and allowing me to see the behind the scenes work of scientific research. I've had a great time there and I truly enjoyed our talks and laugh bursts.

Finally, I want to thank my family for their support during the past five years. For keeping up with me through the stressful periods and for providing me with the opportunities to take on this course of study.

Contents

Chapter 1

The Standard Model

This chapter provides a general outline of the general principles behind the Standard Model (SM), one of the currently most successful theories within the field of physics. The SM is a theory concerning the 3 fundamental interactions of the electromagnetic, weak and strong forces and classifies all subatomic particles known today. The SM explains a wide range of experimental results, stemming from a combined effort of scientists worldwide during the second half of the 20^{th} century. Despite its power to explain and predict, it is incomplete. The shortcomings of the SM will be discussed at the end of this chapter.

1.1 Fundamental Particles

The fundamental particles are divided in 2 groups: the fermions and the bosons, shortly introduced in the following sections.

1.1.1 The Fermions

The first class of particles discussed, the fermions, have spin = 1/2. They are grouped in 3 families according to their masses. Each fermion has a corresponding antifermion. The fermions, in turn, are grouped into 2 classes, the leptons and the quarks, summarised together with some of their properties in Table 1.1. The 6 leptons are the electron (e), muon (μ) and tau-lepton (τ) with corresponding electron- (ν_e), mu- (ν_μ) and tau-neutrinos (ν_τ). The 6 quarks are the up (u), down (d), charm (c), strange (s), top (t) and bottom-quark (b).

Quarks carry apart from electric charge, also a colour charge. Experimentally it is observed that no free colour states exist in nature. This means that quarks (nor gluons, to be explained later) can propagate freely and cannot be observed singularly. Quarks can be bound together forming so-called hadrons (protons, neutrons, pions, ...). The process of forming hadrons is called hadronisation. Leptons on the other hand do not carry colour charge and can certainly be found to propagate freely.

	Fermion Multiplets			T	T_3
Leptons	$\begin{pmatrix}\nu_e\\ e\end{pmatrix}_L$	$\begin{pmatrix}\nu_\mu\\ \mu\end{pmatrix}_L$	$\begin{pmatrix}\nu_\tau\\ \tau\end{pmatrix}_L$	1/2	+1/2 −1/2
	e_R	μ_R	τ_R	0	0
Quarks	$\begin{pmatrix}u\\ d'\end{pmatrix}_L$	$\begin{pmatrix}c\\ s'\end{pmatrix}_L$	$\begin{pmatrix}t\\ b'\end{pmatrix}_L$	1/2	+1/2 −1/2
	u_R	c_R	t_R	0	0
	d_R	s_R	b_R	0	0

Table 1.1: Tabular overview of the fermions comprised within the Standard Model. The subscripts L and R stand for the left- and right handed components, T is the weak isospin and T_3 its third component [1].

1.1.2 The Bosons

Apart from gravitation (which is not comprised within the Standard Model), 3 other fundamental interactions are known. Each of those is mediated by the exchange of one or more vector bosons, which are spin = 1 particles. They are together with their exchange bosons listed below:

- **The strong interaction**: 8 gluons (g) coupling to colour charge.
- **The electromagnetic interaction**: the photon (γ) coupling to electric charge.
- **The weak interaction**: the $W^{\pm}$-bosons and the Z^0-boson coupling to weak charge.

As can be seen from Table 1.1, the quarks carry colour-charge, allowing them to couple to themselves. The W bosons and Z bosons can also couple to themselves, as they carry weak charge. The photon does not share this property as it doesn't carry electric charge.

The only scalar particle, the Higgs-boson, requires some special attention and will be discussed in section 1.3 concerning the Brout-Englert-Higgs Mechanism.

1.2 Fundamental Interactions

The SM is described by a Lagrangian, which describes the whole dynamics of the system. The symmetry group representing the SM Lagrangian is SU(3)×SU(2)×U(1). A symmetry group defines under which transformations a theory is invariant. According to Noether's theorem a conservation law is associated to a physical system for each continuous symmetry of its action [2]. For the SM, the conserved quantities are colour SU(3), weak isospin SU(2) and electric charge U(1).

As was discussed in Sec. 1.1.2, the (gauge-)bosons mediate the SM interactions. In general, gauge-bosons appear as virtual particles between two interaction vertices (as can be schematically depicted by Feynman-diagrams). Depending on which interaction (and the energy-scale at which the interaction occurs) a coupling strength is associated, denoted by α. In this section, each of those fundamental interactions will be discussed in more detail.

1.2.1 The Electromagnetic Force

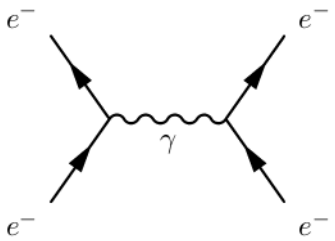

Figure 1.1: A QED process.

The electromagnetic force is the one that acts between electrically charged particles and is fully described by the relativistic quantum field theory of **quantum electrodynamics** (QED), with abelian symmetry group U(1). The gauge-boson mediating the electomagnetic interaction is the massless and electrically neutral photon γ, allowing the interactions up to an infinite range (the forces between particles grow weaker with the distance between them). The photon can interact with every particle carrying an electric charge Q (as can be seen from Fig. 1.1 in which two electrons with Q = -1e interact, exchanging a photon). The coupling strength of the electromagnetic interaction has the value of $\alpha_{\text{em}}(Q^2 = 0) \approx \frac{1}{137}$ [3]. Thanks to the coupling being smaller than 1, this interaction allows calculations in perturbation theory. It needs to be noted still that α_{em} is a running coupling constant, meaning it depends on the value of transferred momentum Q^2. This is a consequence of the fact that the photon isn't capable of undergoing self-interaction, as it doesn't carry any electric charge. This can be understood with the picture that every charged particle is surrounded by a cloud of virtual γ's and e^+e^--pairs which result in a charge screening effect. The higher the transferred momentum, the closer one probes the target under study and the fewer charge screening remains. This results in a higher value of α_{em}.

1.2.2 The Weak Force

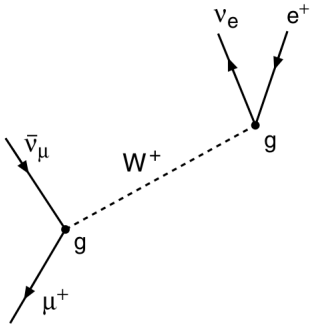

Figure 1.2: A weak interaction process.

The weak interaction is mediated by 3 gauge bosons: the electrically neutral Z^0 boson with mass $M_{Z^0} = 91.2$ GeV/c^2, and the electrically charged W^+ and W^- bosons with $M_{W^\pm} = 80.4$ GeV/c^2. Due to the large masses of the exchange bosons, the weak interaction has a very short range. This allowed Enrico Fermi in the 1940s to develop a theory of interaction described as a point interaction for weak processes. This was implemented in a quantum field theory based on a SU(2) symmetry.

The quantum number that governs the weakly interacting particles is the weak isospin. It is the third component, T_3, that becomes relevant because it is conserved between initial and final states. The left-handed fermions have non-zero T_3: the up-type fermions, have $T_3 = +\frac{1}{2}$ and all down-type fermions have $T_3 = -\frac{1}{2}$.[1] All right-handed fermions have $T_3 = 0$. If one assigns $T_3\,(W^\pm) = \pm 1$, then from Fig. 1.2 one can see that weak isospin is indeed conserved. The coupling strength of the weak interaction is 4 to 5 orders of magnitude smaller than α_{em} at low momentum transfers.

Another important artifact of the weak interaction is the following. Neutral currents through Z^0-exchange couple between quarks of the same flavour whereas charged currents through $W^\pm$-exchange allow coupling between different generations. For leptons, both neutral and charged currents couple to particles inside the same generation. The behaviour for quarks can be understood in terms of the mixing mechanism. When a quark is produced as a mass eigenstate in a certain generation, it decays via the weak interaction as a weak eigenstate which is a superposition of quarks of all three generations. Mathematically the mixing mechanism is described by the Cabibbo-Kobayashi-Maskawa (CKM) matrix, which contains the weak eigenstates in terms of the mass eigenstates, as can be seen from Eq. 1.1.

$$\begin{pmatrix} d' \\ s' \\ t' \end{pmatrix} = V_{\text{CKM}} \cdot \begin{pmatrix} d \\ s \\ t \end{pmatrix} = \begin{pmatrix} V_{ud} & V_{us} & V_{ub} \\ V_{cd} & V_{cs} & V_{cb} \\ V_{td} & V_{ts} & V_{tb} \end{pmatrix} \cdot \begin{pmatrix} d \\ s \\ t \end{pmatrix} \tag{1.1}$$

[1] Anti-fermions get the same T_3-value as their fermion counterparts.

An interesting type of fermions are the **neutrinos** (see Sec. 1.1.1) as they only interact through the weak force and gravity[2], but are not effected by electromagnetic nor strong forces. Their existence was postulated by Wolfgang Pauli in 1930 to explain the occurrence of β-decay

$$n^0 \rightarrow p^+ + e^- + \bar{\nu}_e. \tag{1.2}$$

The combined energies of the proton p^+ and electron e^- do not add up to the energy of the neutron n^0. Therefore Pauli proposed the existence of an electrically neutral neutrino ν_e in order for energy conservation to be satisfied. Note that also spin conservation is now satisfied, where the anti-neutrino is right-handed and the electron left-handed[3].

In 1956, β-capture was proposed to detect neutrinos. Antineutrinos created in a nuclear reactor from β-decay interact with protons according to $\bar{\nu}_e + p^+ \rightarrow n^0 + e^+$. The positron directly annihilates with an electron forming two photons and the neutron can interact with a nucleus, also releasing a photon. This signature is unique for an antineutrino interaction [5]. Later, with the discoveries of the muon and tau-lepton, it was known that neutrinos come in three flavours (ν_e, ν_μ, ν_τ).

Neutrinos can be produced in various ways apart from nuclear reactors. Most neutrinos on Earth originate from nuclear processes inside the Sun (pp chain, ^{7}Be, ^{8}B, etc. [6]). Another very intensive source of neutrinos is a supernova which was measured from the SN 1987A supernova in 1987. It is also thought that a large amount of neutrinos must be present in the Cosmic Neutrino Background (CνB), a remnant from the Big Bang. Due to their incredibly low energies however, the CνB has not yet been observed.

Neutrino-experiments (e.g. IceCube, Soli∂, ...) are widely conducted around the globe: they provide gateways to understand more about the cosmos (from the structure of the universe to dark matter) and provide opportunities to acquire a more thorough understanding about physics beyond the standard model (neutrino-oscillations, reactor anomaly, etc.).

[2]Neutrinos were recently proven to have a small mass, see the paragraph in Sec. 1.4 on neutrino-oscillations, a phenomenon **not** predicted by the SM.

[3]A right-handed particle has its spin in the direction of its momentum whereas a left-handed particle has its spin in the opposite direction to its momentum. One often also speaks of respectively helicity $h = +1$ and $h = -1$. The helicity of the neutrino was determined by Goldhaber in 1958 [4].

1.2.3 The Strong Force

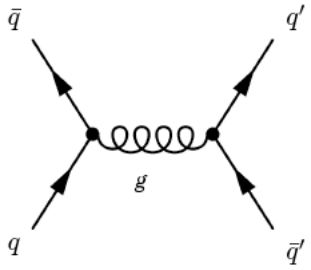

Figure 1.3: A QCD process.

The strong force acts between particles carrying colour charge and is described in the framework of **quantum chromodynamics** (QCD) with non-abelian symmetry group SU(3). The mediating bosons are called the gluons that have spin 1 and couple to colour charge, a conserved quantity for the strong interaction. The 3 possible types of colours are green (g), red (r) and blue (b) and their respective anticolours. Each type of quark and gluon carry a non-zero colour charge. A quark carries one of 3 colours whereas a gluon carries a colour-anticolour combination. In total there are 8 gluons.

Gluons carry colour charge themselves, allowing them to emit other gluons. This property, which is absent in QED, yields the following picture. When the momentum transfer Q^2 increases, gluons start to fluctuate more and more in secondary gluons and cause an anti-screening effect [1]. Because of this, at close distances, the gluon sees less colour charge. This means that the coupling strength grows weaker for higher energy-scales that explains the running of α_s.

In the limit $Q^2 \to \infty$, quarks can be considered to be free due to the very low interquark coupling. This limit is called **asymptotic freedom**. At large distances however, the interquark coupling increases so strongy that it's impossible to detach quarks from hadrons, this principle is called **confinement** and can be understood from a fluxtube being formed between two particles holding colour charge (Fig. 1.4).

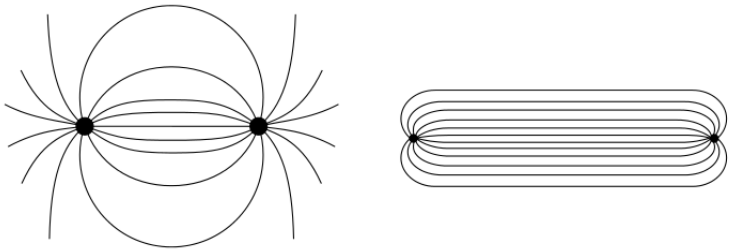

Figure 1.4: Left: Electromagnetic field lines for two separated electrically charged particles. The further apart the particles go, the weaker the field gets ($V(r) \sim 1/r$). Right: Strong interaction field lines in the form of a flux tube. The further apart the particles go the stronger the field gets ($V(r) \sim r$) [1].

Confinement originates from the potential to rise as $V(r) \sim r$ which means that the longer the fluxtube gets, the more energy is stored in the field. Eventually the fluxtube breaks and creates new $q\bar{q}$ pairs.

From renormalisation group theory in QCD [7], it follows that the strong coupling constant α_S at a particular scale μ_1 can be written into an equation in which it is linked to itself at another scale μ_2

$$\alpha_S(\mu_1^2) = \frac{\alpha_S(\mu_2^2)}{1 - \alpha_S(\mu_2^2)\beta_1 \ln\left(\frac{\mu_1^2}{\mu_2^2}\right)} \tag{1.3}$$

With β_1 given by

$$\beta_1 = \frac{11n_c - 2n_f}{12\pi} \tag{1.4}$$

in which $n_c = 3$ denotes the possible number of colour charges and n_f the number of active quark flavours (this depends on the chosen scale). Here, only one loop is taken into account as can be seen from the computation of β_1 in the renormalisation group equation (with $a_S = \frac{\alpha_S}{\pi}$)

$$\beta(a_s) = -\mu\frac{da_s}{d\mu} = \beta_1 a_s^2 + \beta_2 a_s^3 + ... \tag{1.5}$$

It is this equation that for one loop corrections can be analytically transformed into Eq. 1.3. If one now chooses the scale $\mu_2 = \Lambda_{\text{QCD}}$ such that Eq. 1.3 becomes infinite (or the denominator becomes 0) we find the following relationship

$$\Lambda_{\text{QCD}} = \mu_1 e^{-\frac{1}{2\beta_1 \alpha_S(\mu_1^2)}} \tag{1.6}$$

That way, Eq. 1.3 can be rewritten as

$$\alpha_S(\mu^2) = \frac{1}{\beta_1 \ln\left(\frac{\mu^2}{\Lambda_{\text{QCD}}^2}\right)} \tag{1.7}$$

The constant Λ_{QCD} is the scale at which perturbation theory breaks down. Asymptotic freedom is also evident from the above equation, for $\mu \to \infty$ the coupling constant α_S vanishes.

An overview of different measurements of α_S at the scale of the mass of the Z boson M_Z is given in Fig. 1.5. The current world average is $\alpha_S(M_Z^2) = 0.1184 \pm 0.0007$ [8].

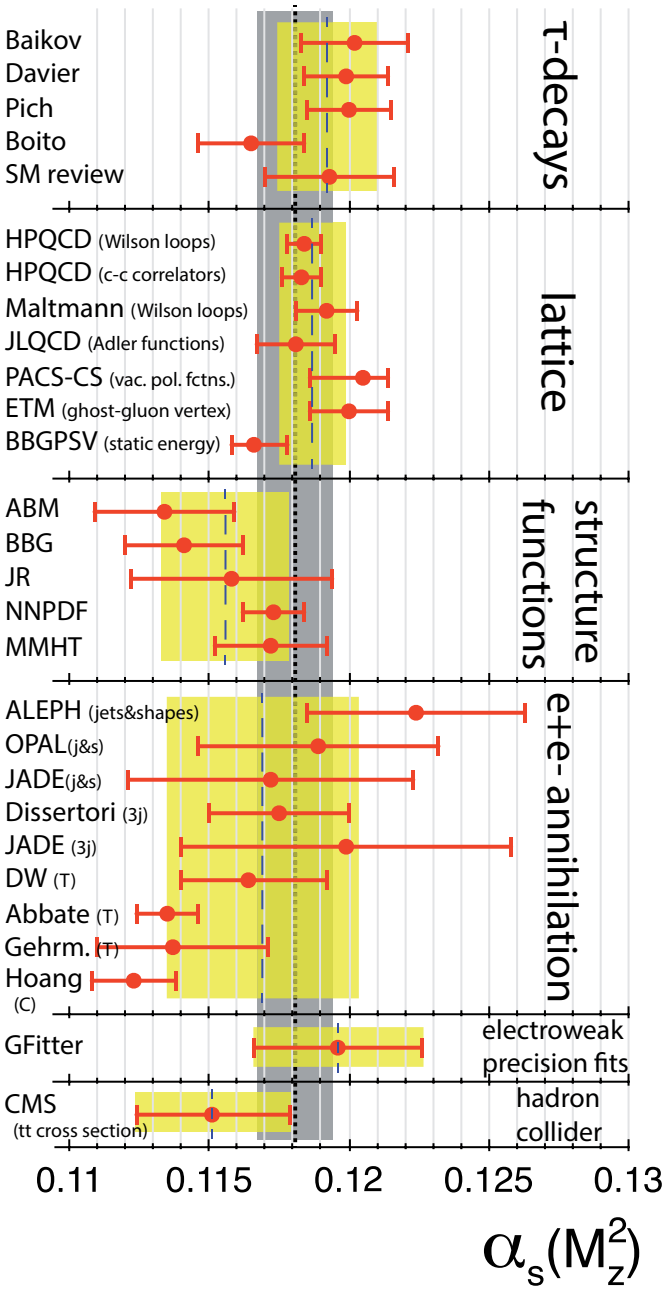

Figure 1.5: Summary of the results various measurements of $\alpha_S(M_Z)$. The world average $\alpha_S(M_Z^2) = 0.1184 \pm 0.0007$ is indicated with the black dotted line and grey uncertainty bands [9].

With the concepts of asymptotic freedom and confinement introduced, for calculations one cannot ignore the very important principles of **factorisation**. The general problem addressed by factorisation is how to calculate high-energy cross sections [10]. A general cross section contains both short range ($\gg Q^2$) and long range ($\ll Q^2$) contributions. The long range part cannot be calculated perturbatively in QCD. Factorisation allows us to derive a prediction for those cross sections by separating long from short range behaviour in a systematic way. A general cross section, e.g. $\sigma_{pp\to t\bar{t}}$, can be written as

$$\sigma_{pp\to t\bar{t}} = \sum_{i,j=\text{partons}} \int_0^1 dx_1 \int_0^1 dx_2 f_i^{\text{PDF}}(x_1, \mu_F^2) f_j^{\text{PDF}}(x_2, \mu_F^2) \sigma_{ij\to t\bar{t}}(\mu_R^2) \tag{1.8}$$

It consists of summing over all possible partons inside the protons that can give rise to the hard scattering process, and integrating over the momentum fractions $x_{1,2}$. The integrandum consists of two Parton Density Functions (PDFs) for each of the two interacting partons i and j. They represent the probability of finding parton i or j carrying a momentum fraction $x_{i,j}$ of the proton, when the proton is probed at a scale μ_F. The PDFs are non-perturbative, process-independent functions that can be obtained from various measurements. To find the PDF at other scales, one can be derived from the other using the DGLAP evolution functions [11]. The integrandum also contains the cross section that only takes the hard scattering into account between both partons and can be written in a perturbative expansion in the running coupling constant α_S [12].

Measuring the $t\bar{t}$ cross-section provides good tests of perturbative QCD and our understanding of the underlying (perturbative) hard scatter cross section. For this however, we need to have reliable PDF sets $f^{\text{PDF}}(x, Q^2)$. Those are acquired from measurements in deep inelastic electron, muon, neutrino and antineutrino scattering experiments and collider data. Dedicated groups have constructed various PDF sets, e.g. NNPDF [13], CTEQ5 [14], CT10, [14], etc.

1.2.4 Electroweak Unification

In the 19^{th} century, Maxwell developed a formalism in which both electricity and magnetism can be described by one framework called electromagnetism. A similar unification was done in the 1960s by Weinberg, Salam and Glashow who combined electromagnetism and the weak interaction into one picture. This **electroweak unification** will be explained in this section.

Earlier was mentioned how the third component of weak isospin T_3 of the W^+ and W^- bosons are +1 and -1 respectively. A third state should therefore exist with $T = 1$, $T_3 = 0$. This state is denoted by W^0 and forms together with W^+ and W^- the weak isospin triplet. One further postulates the existence of a singlet state B^0 with $T = 0$, $T_3 = 0$. The W^0 nor the B^0 are found in nature, they are mathematical constructs that form two other known neutral gauge bosons: the photon and the Z^0. The idea of electroweak unification is to describe the photon and Z^0 as two orthogonal linear combinations of the W^0 and B^0. This is expressed through the so-called electroweak mixing angle θ_W:

$$\begin{aligned} |\gamma\rangle &= \cos(\theta_W)\left|B^0\right\rangle + \sin(\theta_W)\left|W^0\right\rangle \\ \left|Z^0\right\rangle &= -\sin(\theta_W)\left|B^0\right\rangle + \cos(\theta_W)\left|W^0\right\rangle \end{aligned}$$

If we take a look at the dominant Z^0 boson decay modes [8]:

$$\begin{aligned} Z^0 \to\ & e^+e^- && (3.363 \pm 0.004)\% \\ & \mu^+\mu^- && (3.366 \pm 0.007)\% \\ & \tau^+\tau^- && (3.370 \pm 0.008)\% \\ & \bar{\nu}_{e,\mu,\tau}\nu_{e,\mu,\tau} && (20.00 \pm 0.06)\% \end{aligned}$$

we can see how the decay probability into charged leptons is significantly different from the decay probability to neutrinos. Hence the Z^0 cannot just be a neutral W^0 state with equal couplings to all fermions. Its coupling clearly depends on the electric charge, and this is a direct consequence of the fact that the Z^0 has a small electromagnetic component.

1.2.5 Parity and Parity-Violation

An important quantity in subatomic physics is parity P. A parity transformation is defined by

$$\mathrm{P}: \begin{pmatrix} x \\ y \\ z \end{pmatrix} \mapsto \begin{pmatrix} -x \\ -y \\ -z \end{pmatrix} \tag{1.9}$$

in which the spatial coordinates x, y and z flip their signs. It is a quantity that is conserved by electromagnetism, the strong interaction and gravity, but it is violated by the weak interaction. Parity (or P-) violation was proposed by T.-D. Lee and C.-N. Yang and experimentally proven by the Wu experiment conducted by C.S. Wu.

In the Wu experiment, polarised ^{60}Co in a $\vec{B}$ field nuclei were used. These undergo a three stage decay process; namely a nuclear β-decay followed by two high energy photons according to

$$\begin{aligned} {}^{60}\mathrm{Co}(5^+) &\rightarrow {}^{60}\mathrm{Ni}^{**}(4^+) + e^- + \bar{\nu}_e && \text{Weak} \\ {}^{60}\mathrm{Ni}^{**}(4^+) &\rightarrow {}^{60}\mathrm{Ni}^{**}(2^+) + \gamma && \text{Electromagnetic} \\ {}^{60}\mathrm{Ni}^{**}(2^+) &\rightarrow {}^{60}\mathrm{Ni}^{**}(0^+) + \gamma && \text{Electromagnetic} \end{aligned}$$

the numbers between parentheses denote the spin-parity J^P. In the experiment, photons are counted at angles 0° and 90° with respect to the principal axis along the polarisation direction. The photon emission is anisotropic and this anisotropy serves as a measurement of the polarisation: $\epsilon_\gamma = (W(90^\circ) - W(0^\circ))/(W(90^\circ) + W(0^\circ))$. If $\epsilon_\gamma = 0$, then the nuclei have lost all polarisation. The electron counting rate $W_e(\theta)$ is measured and should be equal if parity is conserved by weak interactions for $W_e(0^\circ)$ and $W_e(180^\circ)$. Measuring this can be achieved by flipping the $\vec{B}$ field.

The observation by Wu et al. [15] was that electrons are more likely to be emitted opposite to the field than along it, proving that parity is violated by the weak interaction. Moreover, it seems that parity is maximally violated, leading to the $V - A$ interaction theory proposed by Feynman and Gell-Mann [16].

1.3 The Brout-Englert-Higgs-Mechanism

The Brout-Englert-Higgs-Mechanism was named after the three physicists Robert Brout, François Englert and Peter Higgs, based on their work in the 1960s [17]. This mechanism is essential to explain the generation mechanism of mass for the W and Z gauge bosons, while the photon remaining massless. Furthermore, it predicts the existence of a massive scalar, spin-0 particle: the Higgs boson. As the Higgs boson was eventually discovered at the LHC by the CMS and ATLAS experiments in 2012, it deserves a deeper study of it's theoretical backgrounds.

Out of symmetry considerations, the weak force's gauge bosons should have zero mass, which clearly is not the case. This conundrum is fixed through introduction of a quantum field, the Higgs field, which stretches throughout all space. The masses of the W and Z bosons will arise from breaking the $\mathrm{SU}(2)_L \times \mathrm{U}(1)_Y$ local gauge symmetry of the electroweak sector of the Standard Model. This will be more elaborately discussed below, where most of the discussion is based on [18].

Consider a scalar field ϕ with the potential

$$V(\phi) = \frac{1}{2}\mu^2\phi^2 + \frac{1}{4}\lambda\phi^4 \tag{1.10}$$

with the corresponding Lagrangian

$$\mathcal{L} = \frac{1}{2}(\partial_\mu\phi)(\partial^\mu\phi) - \frac{1}{2}\mu^2\phi^2 - \frac{1}{4}\lambda\phi^4. \tag{1.11}$$

$\frac{1}{2}\mu\phi^2$ represents the mass of the particle, the $\frac{1}{4}\lambda\phi^4$ represents a quartic coupling of the field ϕ with coupling strength $\frac{1}{4}\lambda$. The vacuum state is the lowest energy state of the field ϕ and corresponds to the minimum of the potential. It has its minima at

$$\phi = \pm v = \pm\left|\sqrt{\frac{-\mu^2}{\lambda}}\right|. \tag{1.12}$$

If one considers $\mu^2 < 0$, the field has a non-zero vacuum expectation value. There are two possible vacuum states: $\phi = +v$ and $\phi = -v$. The choice of one of the vacuum states breaks the symmetry of the Lagrangian, this is called **spontaneous symmetry breaking**. If one makes an arbitrary choice of the vacuum state to be $\phi = +v$, small perturbations of the field around the vacuum state can be considered by writing $\phi(x) = v + \eta(x)$. The Lagrangian now becomes

$$\mathcal{L}(\eta) = \frac{1}{2}(\partial_\mu \eta)(\partial^\mu \eta) - \frac{1}{2}\mu^2(v+\eta)^2 - \frac{1}{4}\lambda(v+\eta)^4. \tag{1.13}$$

With the minimum of the potential given by $\mu^2 = -\lambda v^2$, the expression can be written as

$$\mathcal{L}(\eta) = \frac{1}{2}(\partial_\mu \eta)(\partial^\mu \eta) - \lambda v^2 \eta^2 - \lambda v \eta^2 - \frac{1}{4}\lambda \eta^4 + \frac{1}{4}\lambda v^4. \tag{1.14}$$

Comparing this with the Klein-Gordon equation for spin-0 scalar particles

$$\mathcal{L} = \frac{1}{2}(\partial_\mu \phi)(\partial^\mu \phi) - \frac{1}{2}m^2\phi^2 \tag{1.15}$$

it becomes clear that the term proportional to η^2 represents a mass

$$m_\eta = \sqrt{2\lambda v^2} = \sqrt{-2\mu^2}$$

and therefore the Lagrangian 1.15 in terms of the excitations about the minimum describes a massive scalar field. If we apply the same principles of spontaneous symmetry breaking to a complex scalar field, more interesting properties emerge. With a field

$$\phi = \frac{1}{\sqrt{2}}(\phi_1 - i\phi_2) \tag{1.16}$$

the Lagrangian becomes

$$\mathcal{L} = \frac{1}{2}(\partial_\mu \phi)^*(\partial^\mu \phi) - \mu^2(\phi^*\phi) + \lambda(\phi^*\phi)^2 \tag{1.17}$$

$$= \frac{1}{2}(\partial_\mu \phi_1)(\partial^\mu \phi_1) + \frac{1}{2}(\partial_\mu \phi_2)(\partial^\mu \phi_2) - \frac{1}{2}\mu^2(\phi_1^2 + \phi_2^2) - \frac{1}{4}\lambda(\phi_1^2 + \phi_2^2)^2. \tag{1.18}$$

This Lagrangian is invariant under $\phi \rightarrow \phi' = e^{i\alpha}\phi$ and therefore possesses a global U(1) symmetry. Depending on the sign of μ^2, the potential has a different shape. For $\mu^2 < 0$ it has an infinite set of minima denoted by the dashed circle line in Fig. 1.6 (b). Nature will choose one of the vacuum states, causing to spontaneously break the U(1) symmetry. If one chooses a vacuum state (ϕ_1,ϕ_2) = (v,0) and expands the scalar field ϕ as $\phi_1(x) = \eta(x) + v$ and $\phi_2(x) = \xi(x)$ one gets for ϕ and the Lagrangian $\mathcal{L}$

$$\phi = \frac{1}{\sqrt{2}}(\eta + v + i\xi) \tag{1.19}$$

$$\mathcal{L} = \frac{1}{2}(\partial_\mu \eta)(\partial^\mu \eta) + \frac{1}{2}(\partial_\mu \xi)(\partial^\mu \xi) - V(\eta, \xi) \tag{1.20}$$

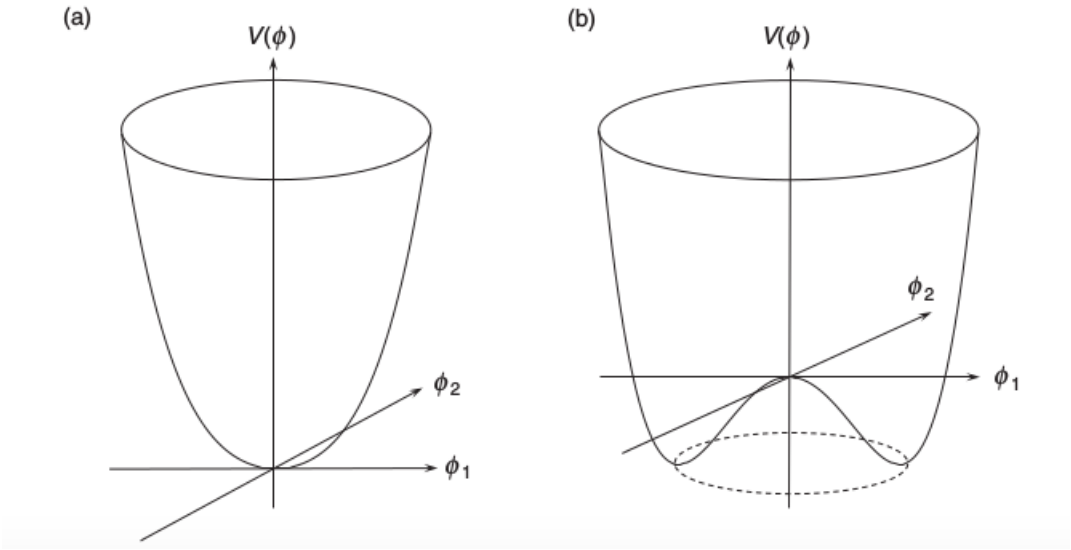

Figure 1.6: The potential $V(\phi) = \mu^2(\phi^*\phi) + \lambda(\phi^*\phi)^2$ for two different values of μ^2: (a) $\mu^2 > 0$ and (b) $\mu^2 < 0$.

with

$$V(\eta, \xi) = -\frac{1}{4}\lambda v^4 + \lambda v^2\eta^2 + \lambda v\eta^3 + \frac{1}{4}\lambda\eta^4 + \frac{1}{4}\lambda\xi^4 + \lambda v\eta\xi^2 + \frac{1}{2}\lambda\eta^2\xi^2 \tag{1.21}$$

Every quadratic term in the field can be interpreted as a mass whereas all higher order terms are interaction terms. This allows the Lagrangian to be rewritten as

$$\mathcal{L} = \frac{1}{2}(\partial_\mu\eta)(\partial^\mu\eta) - \frac{1}{2}m_\eta^2\eta^2 + \frac{1}{2}(\partial_\mu\xi)(\partial^\mu\xi) - V_{int}(\eta, \xi). \tag{1.22}$$

This Lagrangian represents a scalar field η with mass $m_\eta = \sqrt{2\lambda v^2}$ and a massless scalar field ξ. This can be understood by looking at the potential in Fig. 1.6 (b), in which it's clear that the excitations η are up the potential walls and those of ξ are along the dashed circle where the potential doesn't change. The massless scalar particle ξ is known as the **Goldstone boson**.

For the complex scalar field, the Lagrangian is not invariant under a local U(1) gauge transformation

$$\phi(x) \to \phi'(x) = e^{ig\chi(x)}\phi(x). \tag{1.23}$$

This can however be solved by introducing the replacement of the derivatives in the Lagrangian by the corresponding covariant derivatives

$$\partial_\mu \rightarrow D_\mu = \partial_\mu + igB_\mu. \tag{1.24}$$

Then the Lagrangian,

$$\mathcal{L} = (D_\mu \phi)^* (D^\mu \phi) - V(\phi^2) \tag{1.25}$$

is gauge invariant if the new gauge field B_μ transforms as

$$B_\mu \rightarrow B'_\mu = B_\mu - \partial_\mu \chi(x) \tag{1.26}$$

If we take into account that

$$F^{\mu\nu} = \partial^\mu B^\nu - \partial^\nu B^\mu \tag{1.27}$$

We find after plugging Eq. 1.20 into the Lagrangian 1.25, that

$$\mathcal{L} = \frac{1}{2}(\partial_\mu \eta)(\partial^\mu \eta) + \frac{1}{2}(\partial_\mu \xi)(\partial^\mu \xi) - \frac{1}{4}F_{\mu\nu}F^{\mu\nu} + \frac{1}{2}g^2 v^2 B_\mu B^\mu - V_{int} + gvB_\mu(\partial^\mu \xi) \tag{1.28}$$

There is a problem with the last term in the above expression, which is a direct coupling between the spin-1 gauge field B and the Goldstone field ξ. This can be eliminated by performing the gauge transformation

$$B_\mu(x) \rightarrow B'_\mu(x) + \frac{1}{gv}\partial_\mu \xi(x). \tag{1.29}$$

The Lagrangian becomes

$$\mathcal{L} = \underbrace{\frac{1}{2}(\partial_\mu \eta)(\partial^\mu \eta) - \lambda v^2 \eta^2}_{\text{massive } \eta} - \underbrace{\frac{1}{4}F_{\mu\nu}F^{\mu\nu} + \frac{1}{2}g^2 v^2 B'_\mu B'^\mu}_{\text{massive gauge field}} - V_{int} \tag{1.30}$$

We notice that the Goldstone field ξ has disappeared. The original gauge transformation of $\phi(x)$ becomes

$$\phi(x) \rightarrow \phi'(x) = e^{-ig\frac{\xi(x)}{gv}}\phi(x) = e^{-i\xi(x)/v}\phi(x). \tag{1.31}$$

In first order, the form $\phi(x) = \frac{1}{\sqrt{(2)}}\left[v + \eta(x)\right] e^{i\xi(x)/v}$ can be rewritten as

$$\phi(x) \approx \frac{1}{\sqrt{2}}\left[v + \eta(x)\right] e^{i\xi(x)/v} \tag{1.32}$$

This yields

$$\phi(x) \to \phi'(x) = \frac{1}{\sqrt{2}} e^{-i\xi(x)/v} \left[v + \eta(x)\right] e^{i\xi(x)/v} = \frac{1}{\sqrt{2}}(v + \eta(x)). \tag{1.33}$$

Choosing the field $\phi(x)$ to be entirely real, i.e.

$$\phi(x) = \frac{1}{\sqrt{2}}(v + \eta(x)) \equiv \frac{1}{\sqrt{2}}(v + h(x)) \tag{1.34}$$

corresponds to the choosing the previously discussed gauge; the unitary gauge. We now notice that the only physical field in the unitary gauge is the remaining Higgs-field $h(x)$. The Goldstone field $\xi(x)$ was "eaten" by the gauge field. If we write $\mu^2 = -\lambda v^2$, the Lagrangian can be finally rewritten as

$$\mathcal{L} = \underbrace{\frac{1}{2}(\partial_\mu h)(\partial^\mu h) - \lambda v^2 h^2}_{\text{massive h}} - \underbrace{\frac{1}{4}F_{\mu\nu}F^{\mu\nu} + \frac{1}{2}g^2 v^2 B_\mu B^\mu}_{\text{massive gauge boson}} + \underbrace{g^2 v B_\mu B^\mu h^2}_{\text{interactions h, B}} - \underbrace{\lambda v h^3 - \frac{1}{4}\lambda h^4}_{\text{self-interaction h}}. \tag{1.35}$$

This Lagrangian describes a massive scalar Higgs field h and a massive gauge boson B, obeying a U(1) local gauge symmetry. We see thus how the Higgs-mechanism effectively generates mass for the gauge bosons and predicts the existence of a massive scalar particle, **the Higgs Boson**. In the Salam-Weinberg model, the mass terms are found by writing the Lagrangian such that it respects the $SU(2)_L \times U(1)_Y$ local gauge symmetry of the electroweak theory by replacing the derivatives by the appropriate covariant derivatives. We omit the calculation and give the results below. The mass terms for the $W^{(1)}$ and $W^{(2)}$ spin-1 fields appear as:

$$\frac{1}{2}m_W W^{(1)}_\mu W^{(1)\mu} \qquad \text{and} \qquad \frac{1}{2}m_W W^{(2)}_\mu W^{(2)\mu} \text{ with} \qquad m_W = \frac{1}{2}g_W v \tag{1.36}$$

The $W^{(3)}$- and B-terms couple together in the Lagrangian and mix. The relationship between the physical fields and the underlying ones in the Lagrangian is

$$\begin{aligned} A_\mu &= \cos\theta_W B_\mu + \sin\theta_W W^{(3)}_\mu \qquad \text{with } m_A = 0 \\ Z_\mu &= -\sin\theta_W B_\mu + \cos\theta_W W^{(3)}_\mu \qquad \text{with } m_Z = \frac{1}{2}v\sqrt{g_W^2 + g'^2} \end{aligned}$$

Where A_μ represents the massless photon, and Z_μ the massive Z-boson. The Brout-Englert-Higgs-Mechanism thus effectively predicts the masses of the gauge bosons, as well as the existence of a massive scalar spin-0 boson. After the discovery of the Higgs boson in 2012 at the CERN LHC, François Englert and Peter Higgs were awarded the 2013 Nobel Prize in physics.

The Brout-Englert-Higgs mechanism can be used to generate the masses for the fermions. Without giving the exact theoretical considerations, a new interaction, the Yukawa interaction, is introduced that provides the coupling between a scalar field ϕ and a Dirac field ψ. Dirac fields describe the fermions with spin-1/2. The Yukawa couplings of the fermions to the Higgs field are given by

$$g_f = \sqrt{2}\frac{m_f}{v} \tag{1.37}$$

with $v = 246$ GeV the vacuum expectation value of the Higgs field. They occur in a Lagrangian of the form

$$\mathcal{L} = -m_f \bar{f} f - \frac{m_f}{v} \bar{f} f h \tag{1.38}$$

1.4 Limitations of the Standard Model

Apart from the great successes of the Standard Model, some fundamental problems still go unexplained. In essence, it is still unsure how the SM behaves at very high energy scales. As accelerators grow stronger, it might become possible to hit up till now unexplored frontiers and new physics start emerging. An overview of the most important indicators that the SM is incomplete, and the challenges it poses for physicists today, is listed below.

General relativity
The Standard Model does not incorporate the fourth fundamental force: the gravitational interaction. In fact, the SM has to become compatible with general relativity, and this is not the case.

Neutrino-oscillations
In the early 2000's the Super-Kamiokande Collaboration [19] and Sudbury Neutrino Observatory (SNO) [20] Collaborations confirmed the occurrence of neutrino-oscillations: the changing of neutrino flavour as neutrinos travel a particular distance. In case of two neutrino generations, the probability of a neutrino ν_α changing flavour to ν_β is given by

$$P_{\alpha\to\beta} = \sin^2(2\theta)\, \sin^2\left(\frac{\Delta m^2 L}{4E}\right) \tag{1.39}$$

with θ the mixing angle between the neutrino flavour- and mass-eigenstates, E its energy, L its distance travelled and Δm its mass difference. This mechanism thus proves

that neutrinos must have a (small) mass. This phenomenon is not predicted by the Standard Model.

The Hierarchy problem

The so-called hierarchy problem boils down to the question why the weak force is 10^{32} times stronger than gravity. In another formulation, one can ask why the Higgs mass is so small as was experimentally found [21], [22]. The Higgs boson has a bare mass[4] that gets corrected for each particle interacting with it [23]. The heavier the particle, the larger this correction. The top quark adds such a large correction that it is at least peculiar why the bare Higgs mass is so different from the measured one.

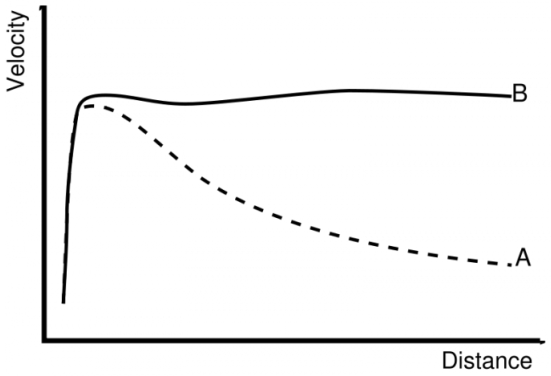

Figure 1.7: Rotational curve of an arbitrary galaxy. A: model without dark matter. B: model with dark matter, as it is measured.

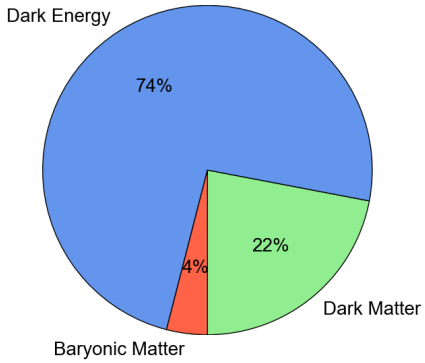

Figure 1.8: Assumed energy distribution of the universe.

Dark Matter and Dark Energy

Dark matter and dark energy are hypothetical substances believed to account for over 96% of all energy in the universe (Fig. 1.8). Dark matter has never been directly observed, as it does not interact electromagnetically, but its existence is inferred from various gravitational effects. One of the most important reasons to believe that there is such a thing as dark matter is that it is a necessary ingredient to explain the observationally measured rotation curves of galaxies, as depicted in Fig. 1.7. It is observed that at large distances from the galaxy center, stars move at larger rotational speeds

[4]The bare mass is the mass of the particle when the scale of distance to it approaches zero. The measured mass is the "dressed" mass, which is an addition to the bare mass because the particle interacts with virtual particle pairs temporarily created by the force field around the particle.

than can be explained from the observed mass distribution. Therefore extra matter is incorporated in the model: dark matter. Another example are the various gravitational lenses that have been observed. Those are massive objects (typically galaxies) bending the trajectories of light coming from behind and distorting the images seen through telescopes. The lens is often observed to be much less heavy than the lensing effect it causes, adding to the belief there is more mass present than can be observed. Other evidence can be found in measured anisotropies in the angular distribution of the Cosmic Microwave Background (CMB) in which cold dark matter is introduced as an explanation of this anisotropy[5]. The Standard Model does not contain any particle candidate that could be explained as being the primary dark matter component, it thus only explains ∼4% of observable matter in the universe. There are models that incorporate DM particles into the SM (e.g. MACROs [25]), however those are less popular.

Matter-antimatter asymmetry
The observable universe is made of primarily matter and contains only small proportions of antimatter. The Standard Model predicts that matter and antimatter should have been created in (almost) equal amounts when the universe was formed. There is no mechanism incorporated within the SM that can explain the observed asymmetry.

All predictions made by the SM have been confirmed, often with high precision. At the time of writing there is no single theory that successfully incorporates all the needed extensions explained above (especially general relativity, which is also highly successful). The most popular extension is Supersymmetry (SUSY) and is very intensively searched for at the LHC. A general introduction to SUSY is given in Chapter 2.

[5]This is often called the ΛCDM model. Recent CMB anisotropies were measured by WMAP [24]

Chapter 2

Supersymmetry

2.1 General introduction

As is alluded in the previous chapter, the Standard Model clearly is an incomplete theory. Up till now, no framework exists to describe the physics at very high energies up to the Planck scale, with $M_P = (8\pi G_{\text{Newton}})^{-1/2} = 2.4{\times}10^{18}$ GeV/c^2, where quantum gravitational effects become important. This was already addressed before in a brief mentioning of the so-called hierarchy problem (Sec. 1.4). The Higgs boson receives quantum corrections to its mass originating from the virtual effects of particles that couple to the Higgs field. This is described in more detail in Ref. [26], where a large part of the discussion in this chapter is based on. Consider for example the loop diagram given in Fig. 2.1. In the Lagrangian a term of the form -$\lambda_f H\bar{f}f$ will originate and yields a correction (after applying the Feynman rules, which is omitted here)

$$\Delta m_H^2 = -\frac{|\lambda_f|^2}{8\pi^2}\Lambda_{\text{UV}}^2 + ... \tag{2.1}$$

with λ_f the Yukawa-coupling. The mass of a fermion is proportional to its Yukawa-coupling meaning that the Higgs boson couples most strongly to the most massive particles.

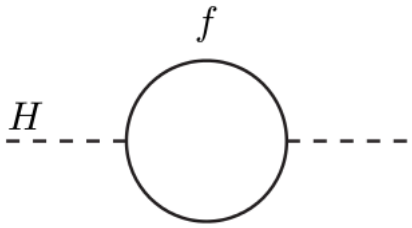

Figure 2.1: One-loop quantum correction to the Higgs squared mass parameter m_H^2.

The negative sign originates from the spin-statistics theorem, which dictates that fermions yield negative contributions whereas bosons yield positive contributions. The factor Λ_{UV} is called the ultraviolet cutoff and denotes the scale up to which the Standard Model is valid. Filling the top quark into the equation yields unnaturally high corrections to M_H^2 at the Planck mass, since the correction depends quadratically on the cut-off. This particular problem can be solved by the principles of **supersymmetry**. It is an extension of the SM that creates superpartners for all Standard Model particles. In our particular example, the addition of supersymmetric partners adds extra terms to Eq. 2.1 and yields cancellation between them, effectively reducing the correction to zero.

Formally, Supersymmetry or SUSY, is a symmetry that relates bosons and fermions. A supersymmetry transformation turns a bosonic into a fermionic state and vice versa. This is done through the introduction of an anti-commuting spinor with

$$\begin{aligned} Q\,|\text{Boson}\rangle &= |\text{Fermion}\rangle \\ Q\,|\text{Fermion}\rangle &= |\text{Boson}\rangle \end{aligned} \tag{2.2}$$

2.2 Supermultiplets

The supersymmetric particles are divided in **supermultiplets** . Each of those contain both boson and fermion states who are superpartners of each other. Because the squared-mass operator -P^2 commutes with the operators Q and $Q^\dagger$ it follows that particles within the same supermultiplet have the same masses. The generators Q and $Q^\dagger$ also commute with the generators of the gauge transformations. This has the consequence that particles within the same supermultiplet must have the same electric charges, weak isospin and color charges. A final very important remark is that it can be proven from quantum mechanical considerations (done in [26]) that the number of degrees of freedom for fermions and bosons must be exactly equal within the same supermultiplet. Therefore one has

$$n_F = n_B. \tag{2.3}$$

This property can then be used to construct two types of multiplets that are used to classify the supersymmetric particles.

Chiral supermultiplets
The first considered supermultiplet consists of a single Weyl fermion (with two spin helicity states; $n_F = 2$) and two real scalars ($n_B = 1$). The two real scalar degrees of freedom are then combined into a complex scalar field. The combination of a two-component Weyl fermion and a complex scalar field is called a chiral supermultiplet.

Gauge supermultiplets
A second possible supermultiplet contains a spin-1 vector boson that is massless (in order for the theory to be renormalizable). Such a boson has 2 helicity states which yields $n_B = 2$. Its superpartner must therefore have two degrees of freedom, $n_F = 2$, and this is again a massless spin-1/2 Weyl fermion. The combination of spin-1/2 gauginos and spin-1 gauge bosons is called a gauge supermultiplet.

In a supersymmetric extension of the SM, each of the already known fundamental particles are classified into a chiral or gauge supermultiplet. They each have a superpartner that has a spin differing by 1/2 unit. Other combinations of spins are possible but those can always be reduced to chiral or gauge supermultiplets [26].

2.3 The Minimal Supersymmetric Model

The Minimal Supersymmetric Model (MSSM) is a minimal supersymmetric extension of the Standard Model. It contains the least number of particles you can add to the Standard Model to make a viable SUSY model. A first step is to categorise the already known SM particles into the SUSY picture, then supersymmetry breaking will be discussed, and a conserved quantity called R-parity will be introduced. This section is based on Ref. [26].

2.3.1 Particle Categorisation

The Standard Model fermions (quarks and leptons) are members of chiral supermultiplets. This is because left-handed fermions couple differently under the gauge group than their right-handed parts. The supersymmetric particles of fermions are spin-0 particles. As a naming convention, the letter "s" is put in front of the SM partner's names ("s" denotes "scalar"). This way, the *sfermions* are subdivided into *squarks* and *sleptons*. Their symbols are the same as those of the SM ones, but they get an extra tilde ($\tilde{}$). For example, the left- and right-handed selectrons are denoted by $\tilde{e}_L$ and $\tilde{e}_R$. The smuons and staus are given accordingly by: $\tilde{\mu}_L$, $\tilde{\mu}_R$, $\tilde{\tau}_L$, $\tilde{\tau}_R$. Only left-handed SM neutrinos exist, the sneutrinos are therefore denoted by: $\tilde{\nu}_e$, $\tilde{\nu}_\mu$, $\tilde{\nu}_\tau$. Finally, the squarks

are given by $\tilde{q}_L$, $\tilde{q}_R$ with $q = u, d, s, c, b, t$. Since the gauge interactions within the chiral supermultiplet are equal, also the left handed squarks couple to the W boson whereas the right handed squarks do not.

The Standard Model vector bosons reside in gauge supermultiplets. The gauge interactions of the $SU(3)_C$ group of QCD are mediated by the gluon g whose supersymmetric partner is the *gluino* $\tilde{g}$. The spin-1 bosons W^+, W^0, W^- and B^0 of the electroweak gauge symmetry $SU(2)_L \times U(1)_Y$ have the *winos* and *bino* as supersymmetric partners: $\tilde{W}^+$, $\tilde{W}^0$, $\tilde{W}^-$, $\tilde{B}^0$. As described in Sec. 1.2.4, electroweak symmetry breaking mixes the W^0 and B^0 eigenstates to give the mass eigenstates Z^0 and γ. The corresponding gaugino mixtures of $\tilde{W}^0$ and $\tilde{B}^0$ are the *zino* $\tilde{Z}^0$ and *photino* $\tilde{\gamma}$.

The Standard Model Higgs boson (spin-0) resides in a chiral supermultiplet. It turns out however, that one Higgs chiral supermultiplet is not enough. This would result in what is called a *gauge anomaly* and would cause an inconsistent quantum theory[1]. It turns out that the problem can be solved by introducing two Higgs multiplets: one with $Y = +\frac{1}{2}$ and one with $Y = -\frac{1}{2}$[2]. They are also both necessary as only a $Y = +\frac{1}{2}$ Higgs chiral supermultiplet can have the necessary Yukawa couplings to give masses to charge +2/3 up-type quarks. The $Y = -\frac{1}{2}$ Higgs chiral supermultiplet in its turn can only provide masses for the -1/3 down-type quarks (and to the charged leptons). The scalar fields with $Y = +\frac{1}{2}$ and $Y = -\frac{1}{2}$ are named H_u and H_d, respectively. The weak isospin components of H_u with $T_3 = (1/2, -1/2)$ have electric charges 1,0 and are denoted by (H_u^+, H_u^0). In a similar way we have (H_d^0, H_d^-). The superpartners then become $\tilde{H}_u^+$,$\tilde{H}_u^0$ and $\tilde{H}_d^0$,$\tilde{H}_d^-$ and are referred to as the *Higgsinos*.

The higgsinos and electroweak gauginos mix with eachother because of electroweak symmetry breaking. The neutral higgsinos ($\tilde{H}_u^0$, $\tilde{H}_d^0$) and the neutral gauginos ($\tilde{B}$, $\tilde{W}^0$) combine to form four mass eigenstates called *neutralinos* ($\tilde{\chi}_1^0$, $\tilde{\chi}_2^0$, $\tilde{\chi}_3^0$, $\tilde{\chi}_4^0$). The charged higgsinos ($\tilde{H}_u^+$, $\tilde{H}_d^-$) and winos ($\tilde{W}^+$, $\tilde{W}^-$) mix to form two mass eigenstates with charge ± 1 called the *charginos* ($\tilde{\chi}_1^+$, $\tilde{\chi}_1^-$, $\tilde{\chi}_2^+$, $\tilde{\chi}_2^-$).

The above discussed sparticles are all the particles comprised within the MSSM and are summarised in Tables 2.1 and 2.2.

[1] Gauge anomalies invalidate the gauge symmetry of a quantum field theory. Gauge symmetries are theories where symmetry transformations are space-time dependent. They are used to generate dynamics, namely the gauge interactions. For a more thorough explanation, refer to [27].

[2] Y stands for weak hypercharge and is given by $Y = 2(Q - T_3)$, with Q the electric charge and T_3 the third component of weak isospin.

Names		spin 0	spin 1/2
squarks, quarks	Q	$(\widetilde{u}_L \;\; \widetilde{d}_L)$	$(u_L \;\; d_L)$
($\times$3 families)	$\overline{u}$	$\widetilde{u}^*_R$	$u^\dagger_R$
	$\overline{d}$	$\widetilde{d}^*_R$	$d^\dagger_R$
sleptons, leptons	L	$(\widetilde{\nu} \;\; \widetilde{e}_L)$	$(\nu \;\; e_L)$
($\times$3 families)	$\overline{e}$	$\widetilde{e}^*_R$	$e^\dagger_R$
Higgs, higgsinos	H_u	$(H^+_u \;\; H^0_u)$	$(\widetilde{H}^+_u \;\; \widetilde{H}^0_u)$
	H_d	$(H^0_d \;\; H^-_d)$	$(\widetilde{H}^0_d \;\; \widetilde{H}^-_d)$

Table 2.1: Chiral supermultiplets in the Minimal Supersymmetric Standard Model. The spin-0 fields are complex scalars, and the spin-1/2 fields are left-handed two-component Weyl fermions [26].

Names	spin 1/2	spin 1
gluino, gluon	$\widetilde{g}$	g
winos, W bosons	$\widetilde{W}^\pm \;\; \widetilde{W}^0$	$W^\pm \;\; W^0$
bino, B boson	$\widetilde{B}^0$	B^0

Table 2.2: Gauge supermultiplets in the Minimal Supersymmetric Standard Model. The spin-1 fields are the SM vector bosons, the spin-1/2 ones are their supersymmetric counterparts [26].

2.3.2 Broken Symmetry

In Sec. 2.2 it was explained how particles within the same supermultiplets must have the same mass, this however requires some extra attention. At the time of writing, not a single superpartner of the SM particles has been discovered. If supersymmetry would be an unbroken symmetry, then there would have to be selectrons $\tilde{e}_L$ and $\tilde{e}_R$ with masses exactly equal to the electron mass $m_e = 0.511$ MeV (this is also the case for all other SM particles). Those sparticles should be easily detectable but they haven't been found. Supersymmetry must thus be a broken symmetry, causing sparticles to have higher masses than their SM counterparts. In other words, this means that the model explaining the symmetry breaking, should have a Lagrangian density that is invariant under supersymmetry, but a vacuum state that is not.

The exact theoretical considerations fall outside the scope of this study, and it is satisfying enough to understand that superpartners will have higher masses than their SM counterparts. The general idea however of supersymmetry breaking is to introduce an effective MSSM Lagrangian consisting of two parts

$$\mathcal{L} = \mathcal{L}_{\text{SUSY}} + \mathcal{L}_{\text{soft}} \tag{2.4}$$

with $\mathcal{L}_{\text{SUSY}}$ containing the gauge and Yukawa interactions, preserving supersymmetry invariance and $\mathcal{L}_{\text{soft}}$ violating supersymmetry. The second part is called *soft* because the breaking terms are constructed such, that they do not introduce quadratic divergences [28]. We also note that there are no theoretical predictions towards the actual masses of SUSY particles, which makes SUSY searches extra challenging.

2.3.3 R-parity

R-parity R_P [29], [30] is a discrete multiplicative symmetry that can be written as

$$R_P = (-1)^{3B+L+2S}, \tag{2.5}$$

with B denoting the baryon number, L the lepton number and S the spin of a particle. It has the property that all SM fields have $R_P = +1$ whereas all the superpartners of SM fields have $R_P = -1$. R-parity is introduced into the MSSM in order to eliminate the possibility of B- and L-number violation. It is mentioned here as R-parity conservation[3] has three very important consequences:

- SUSY particles are always produced in pairs.
- The lightest sparticle with $R_P = -1$, called the *lightest supersymmetric particle* or LSP, must be stable[4]. Considering it to be massive, weakly interacting and electrically neutral, makes the LSP a viable candidate to explain dark matter.

It is clear that R-parity conservation puts some interesting constraints on the possible SUSY Feynman-diagrams. Also note that the LSP behaves like a neutrino and thus escapes detection, it is in general identified with the lightest neutralino $\tilde{\chi}_1^0$.

[3] R-parity conservation is an assumption made in the MSSM, theories with R-parity violation exist too, but aren't considered here.

[4] Because of energy- and R-parity conservation it cannot decay to other SUSY or SM particles.

2.4 SUSY-searches at the LHC

Due to the fundamental differences between the SM and SUSY, it deserves our attention to understand how SUSY-searches at the LHC can be conducted. From theoretical calculations, it seems that squark and gluino production are expected to be dominant processes. Since they are expected to be heavy, they will produce long decay chains eventually leading to a final state with only SM particles and LSPs. Those Standard Model particles will typically be leptons (e or μ), neutrinos, and quarks that hadronise into jets. The LSP is neutral and interacts weakly, causing it to have the same behaviour as the neutrino in a detector in turn causing it to be undetectable.

It becomes clear that one has to construct smart techniques in order for SUSY-signatures to be detectable. Obviously, typical SUSY-processes will have large E_T^{miss} due to the presence of the LSP. This can be exploited by constructing various variables who can discriminate SUSY- from regular SM-processes (an example will be given in the Analysis section). SUSY searches are typically distinguished by the number of leptons required in the final state. We list a few possibilities below.

- Zero-lepton searches typically focus on the escaping dark-matter candidate (the LSP). The cross section for events with large E_T^{miss}, large number of jets and no leptons is very large. Unfortunately, the SM background shares this property, making this a difficult channel to look at.

- One-lepton searches use the fact that SUSY models couple to weak interaction, meaning it is likely that a single lepton ($+ \nu$) is produced.

- A very SUSY-specific signal is the same-sign dilepton channel. A possible process can be understood if we consider the decays $\tilde{g} \to \tilde{t}\bar{t}$ and $\tilde{g} \to \tilde{t}^* t$, which are possible in simple R-parity violating models, and occur with the same probability. Gluino pair-production could lead to events with two same-sign tops. If both decay leptonically a same-sign dilepton signature is obtained. Obviously, opposite-sign dilepton searches are also conducted, this will be more elaborately discussed in Chapter 5

- Multi-lepton searches also exist in which production of charginos and neutralinos are considered, giving rise to 3 leptons.

The above listing shows some of the possible SUSY-search scenarios, and more possibilities exist. This thesis will contain research work within an opposite-sign dilepton analysis in which stop-quark production is the analysed signal in the MSSM, where R-parity conservation is expected.

Chapter 3

The CMS Experiment at the LHC

3.1 The Large Hadron Collider

The Large Hadron Collider is the biggest and most powerful particle accelerator in the world. It is located at CERN (European Organization for Nuclear Research) near Geneva, Switzerland. The accelerator consists of a circular-shaped tunnel with a circumference of approximately 27 km and allows **protons** (as well as heavy ions) to collide at very high center-of-mass energies.

In order to establish proton collisions, two beam pipes are necessary to bend the protons in opposite directions and allow collisions at fixed points along the accelerator. The guidance and bending is done through the use of superconducting dipole magnets to bend, and quadrupole magnets to focus the protons along the optical axis. Superconductivity is necessary as extremely high currents up to $12{\times}10^3$ A are required in the magnet coils to provide high magnetic fields. Higher order magnets are also used to provide additional corrections to the beam.

The design luminosity of the LHC is L = $10^{34}\text{cm}^{-2}\text{s}^{-1}$, achieved from the circulation of protons through the accelerator (about $11{\times}10^3$ turns per second) that are bunched together with bunch spacings of 25 ns. Protons are currently being accelerated to 6.5 TeV each, resulting in a center-of-mass energy of $\sqrt{s}$ = 13 TeV (before this, the LHC also operated at 7 and 8 TeV at respective peak luminosities of 3.7×10^{33} $\text{cm}^{-2}\text{s}^{-1}$ and 7.7×10^{33} $\text{cm}^{-2}\text{s}^{-1}$). This is a never-before achieved energy and provides tremendously exciting research opportunities.

On the LHC-ring (schematically depicted in Fig. 3.1), four main experiments are in-

stalled around the interaction points where the beams collide, namely, ATLAS and CMS; two general purpose detectors, and ALICE and LHCb; conducting heavy-ion and b-physics experiments, respectively. This thesis will be subjected to an analysis situated within the scope of the CMS-experiment, which will be more thoroughly explained in the next section.

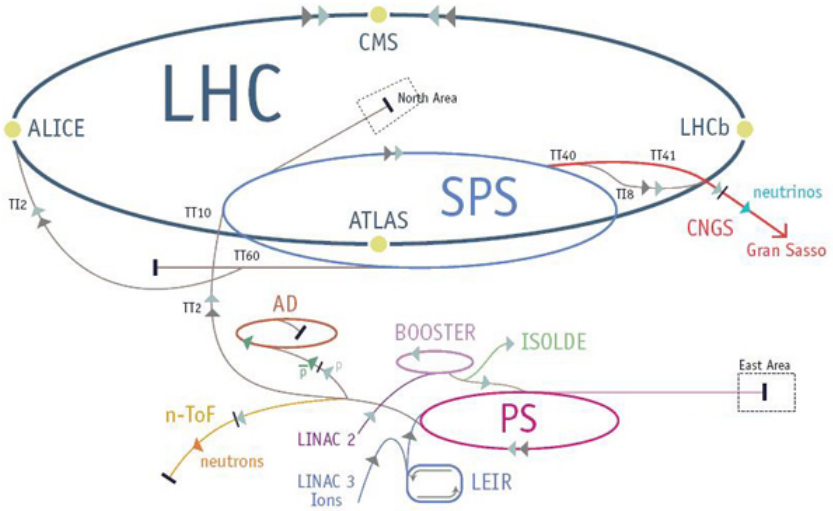

Figure 3.1: Schematic overview of the LHC-complex. Depicted in yellow are the four main experiments. © CERN Collaboration

The injection of protons into the LHC is followed after a gradual increase in their energy using different accelerator structures depicted in Fig. 3.1. The protons originate from a bottle of hydrogen gas, whose electrons are stripped after applying an electric field. They are passed to a Linear Accelerator (LINAC) structure, accelerating the protons to an energy of 50 MeV before entering the booster. The booster accelerates to an energy of 1.4 GeV, which subsequently passes the protons to the Proton Synchrotron (PS) and eventually to the Super Proton Synchrotron (SPS), accelerating respectively to 25 and 450 GeV. Finally, the protons are transferred to the two beam pipes of the LHC, further increasing their energy up to 6.5 TeV at which they collide.

A schematic view of a proton-proton collision is given in Fig. 3.2. Two partons from each of the two protons interact with each other forming a primary, hard-scatter interaction vertex (depicted with the red dot). This process produces a new state that eventually decays into a spray of particles. Those undergo a showering process after

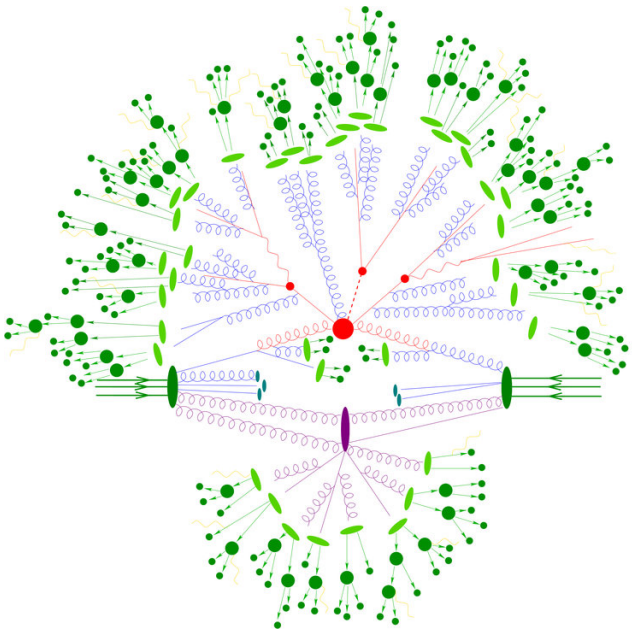

Figure 3.2: Schematic view of a proton-proton collision [31].

which they hadronise into the particles that finally reach the detector.

The huge advantage of a proton-proton accelerator over for example an electron-positron accelerator is that a very wide energy range can be probed. This is a direct consequence of the fact that partons inside the proton carry a fraction of the momentum of the proton, thus allowing collisions to take place at different values of transferred momentum.

With proton-proton collisions, the LHC allows to look at the fundamentals of what matter consists of and helps scientists to gain a deeper and more profound understanding of the fundamental open questions in physics. This concerns the basic laws governing the interactions among elementary particles, the scales at which current theories break down or not, etc.

Apart from proton-proton collisions, the LHC also serves another purpose: **heavy-ion** collisions. Reactions between heavy-ions have proven themselves very useful regarding the investigation of the thermodynamical properties of QCD matter. The difference with protons colliding is not that single protons, but a bunch of protons and neutrons are smashed together to form a very dense nuclear matter system. With these type of collisions, physicists try to investigate the **quark-gluon plasma**.

The quark-gluon plasma is a hypothesized phase of nuclear matter, believed to exist at either very high densities or very high temperatures (or both). If one were to compress a nucleus (without altering the temperature) to very high densities ($\sim$10$\times$), individual nucleons would start overlapping. If one on the other hand would increase the temperature (without altering the density), the individual nucleon-nucleon interactions would increase in such a way, that the collisions between them would make it impossible to assign a quark or gluon to any hadron in particular. The state is said to consist of asymptotically free quarks and gluons.

The discovery of the quark-gluon plasma could provide great confidence in our understanding of strongly interacting matter. Apart from that, it would be a simulation of the universe at a very early stage in its history ($\sim$30 μs after the Big Bang).

At CERN, the LHC operates approximately one month yearly in nuclear collision mode. Pb-nuclei collide at 2.76 TeV per nucleon pair and produce big sprays of strongly interacting particles around the central collision point who are then detected by the detectors installed on the LHC.

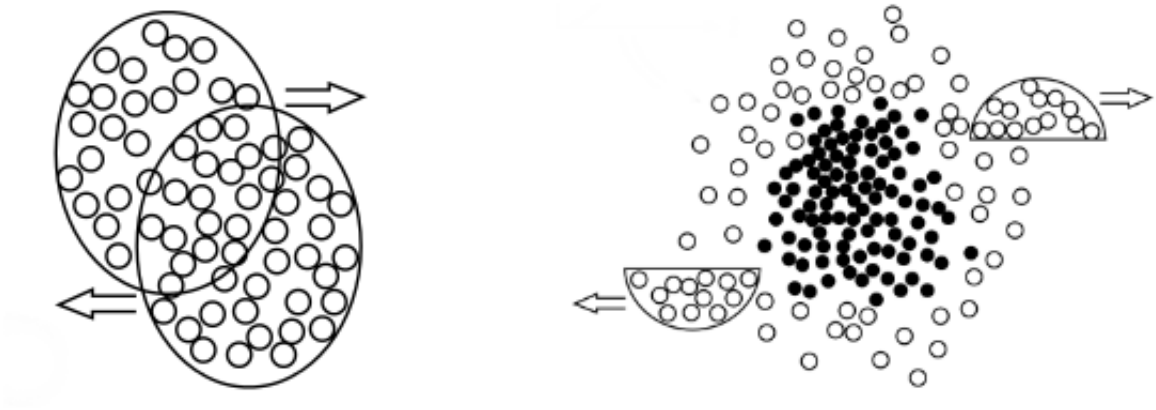

Figure 3.3: Two heavy-ions collide with partial overlap (left). A spray of strongly interacting particles (black dots) are produced (right) [1].

3.2 The CMS-Experiment

The CMS, or Compact Muon Solenoid experiment, is a general purpose particle physics detector situated on the LHC-ring. It is cylindrically shaped with a diameter of 15 m and a length of 28.7 m, weighing 14000 metric tonnes. It gained world fame after it discovered together with ATLAS the Standard Model Higgs-Boson in July 2012. The main objectives of the CMS-experiment are (1) to explore physics at very high energy scales (TeV-range), (2) to test the SM at new energy regimes and phase space regions that have not been explored before, (3) to increase the precision of SM electroweak and QCD parameters, (4) to study the properties of the recently discovered Higgs-boson, (5) to look for physics beyond the standard model, in particular Supersymmetry and (6) to help in providing a possible explanation of dark matter.

The detector has an onion-like structure where each layer serves a different purpose that helps in identification of particles originating from the central collision. The signal from each detector component is then combined in order to reconstruct the original process that took place. This is not an easy task as collisions are happening at a frequency of 40 MHz, making extremely fast electronics and smart algorithms necessary to distinguish the different interactions. The different components of the detector are described below.

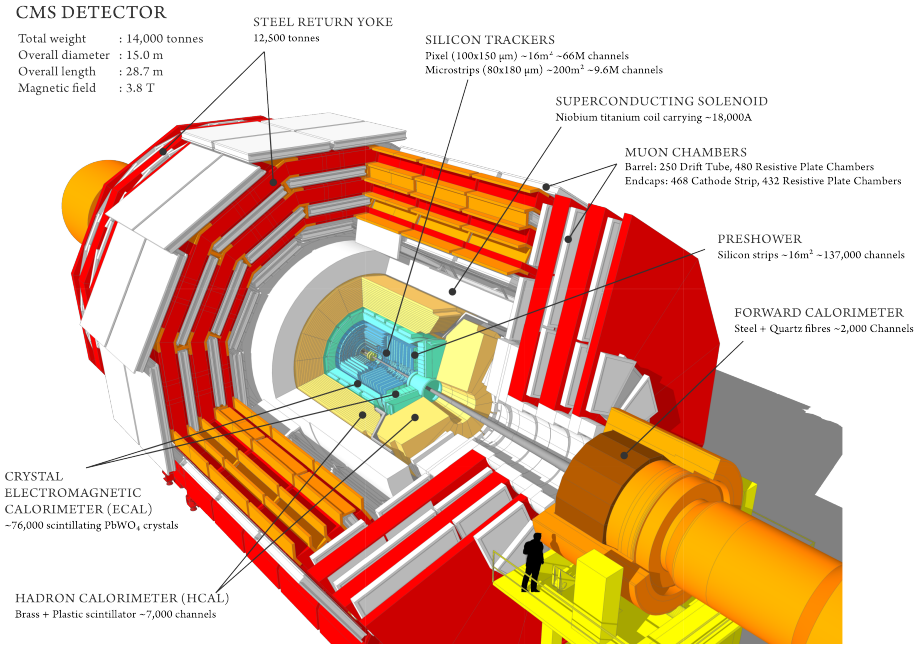

Figure 3.4: Overview of the different sections of CMS. © CMS Collaboration

3.2.1 The Tracker

The tracker sits at the very core of the detector and surrounds the interaction point. It has a length of 5.8 m and a diameter of 2.5 m and covers a pseudorapidity range of $|\eta| < 2.5$[1]. The tracker's function is to provide a precise measurement of the trajectories of charged particles emerging from the interaction point as well as identifying secondary vertices from prolonged b quark and τ-decays. Due to the extremely intense dose of radiation at which the tracker is exposed, it is composed entirely from silicon-based detector technology, as this material provides a very long lifetime.

The tracker consists of two main sections. The most central part is the *pixel detector* consisting of three co-axial cylindrical layers of pixel detector modules, closed of at the side by another two pixel modules. The pixel detector delivers three high-precision space points for each particle trajectory (charged particle trajectories are curved due to the presence of a high magnetic field, to be explained later). It is this precision that allows accurate measurements of secondary vertices as displayed in Fig. 3.5.

In order to detect b quarks (typically necessary for detecting processes as depicted in Fig. 4.3.1) one determines the impact parameters d (the distance of closest approach of a secondary track to the primary vertex) and determines whether they're larger than some reference to be sure the track originated from a secondary vertex. A distribution of L_{xy} (the decay distance in the plane transverse to the beam direction) allows comparison with typical b quark lifetime distributions.

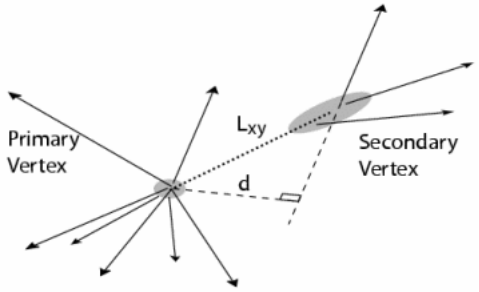

Figure 3.5: Display of a secondary vertex originating from b-quark decay. d and L_{xy} are also depicted. © CDF Collaboration

The second and outermost section of the track system is the *silicon strip tracker* and

[1]The pseudorapidity η is a measure for the angle of a particle relative to the beam-axis and is defined as $\eta = -\ln\left[\tan\left(\frac{\theta}{2}\right)\right]$. It is frequently used as η is boost-invariant, whereas θ isn't. This allows displays of particle energy depositions in so-called lego plots between the two boost invariant quantities η and ϕ, with the latter being the (boost-invariant) angle in the transverse plane. This way, angular differences are not influenced by the boost of the particles.

provides additional resolution to the tracks measured. After the particles leave the pixel detector, they pass through 10 layers of silicon strip detectors, reaching out to a radius of about 1.2 m. Silicon semiconductor technology allows very fast readout capability, which is necessary for collisions happening each 25 ns.

3.2.2 The Electromagnetic Calorimeter

The electromagnetic calorimeter or ECAL surrounds the tracker, with an inner radius of about 1.3 m to an outer radius of about 1.7 m and covers a pseudorapidity range $|\eta| < 3.0$. Its function is to detect those particles that interact electromagnetically; in particular electrons/positrons and photons. It consists of a large collection of lead tungstate crystals ($PbWO_4$) spread over the barrel and two endcaps. These kind of crystals scintillate, meaning they produce light proportional to the energy deposited in the crystal. This light is collected through Avalanche Photo Diodes (APDs) attached to one side of the crystal[2] which eventually produce an electric signal in proportion to the incoming light, thus in proportion to the deposited energy. The crystals have a very short interaction length and can withstand very high doses of radiation.

$PbWO_4$ is an inorganic scintillator crystal with impurities added. When an energetic particle passes, electrons are elevated from valence to the conduction band. The electron is then free to move through the crystal after which it eventually recombines with a hole and produces light. The impurities are necessary to make the recombination more efficient, thus yielding very fast light outputs (See Fig. 3.6). In 25 ns, about 80% of the light produced from the energy deposit is emitted [32].

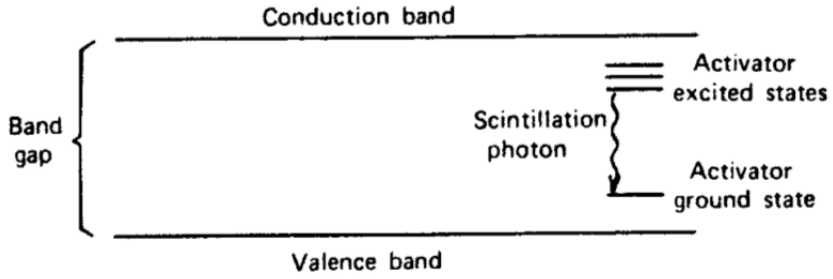

Figure 3.6: Schematic display of the $PbWO_4$ band structure. © G. F. Knoll, Radiation detection and measurement. (2010)

[2]APDs are used for the ECAL barrel section. For the ECAL endcap sections, vacuum phototriodes are used.

At the endcap on the inner side, the ECAL preshower system is installed on both sides. It has a finer granularity; silicon detector strips of 2 mm wide compared to the 3 cm crystals of the rest of the ECAL. One of its important design constraints is to be able to resolve nearby γ's so that the Higgs boson decaying into two photons could be precisely reconstructed. This is studied using the $\pi^0 \to \gamma\gamma$ process which is typically boosted and produces very small decay angles between the 2 photons, thus giving rise to a possible single hit in the 3 cm ECAL crystal. The smaller strips can distinguish between such hits.

3.2.3 The Hadronic Calorimeter

The hadronic calorimeter or HCAL is situated in between the ECAL and the solenoidal magnet (next section) with inner radius of 1.77 m and outer radius of 2.95 m and covers a pseudorapidity range $|\eta| < 3.0$. It is designed to measure mainly the energy of hadrons, interacting strongly with the HCAL material. Due to the larger interaction length of hadrons, the HCAL must be larger than the ECAL.

The HCAL is a sampling calorimeter[3], existing of 36 barrel and endcap wedges. It is made of alternating layers of dense brass (passive) absorber material and (active) plastic scintillator. The idea is that particles hit the absorber material and produce a cascade of shower particles. These deposit energy in the scintillation material again providing an electrical output proportional to the deposited energy. This is done through the use of optical fibres that conduct the light output into readout boxes where photodetectors amplify the signal. The shower has an electromagnetic and hadronic component (see Fig. 3.7). The hadronic component contains mostly $\pi^{\pm}$ and π^0 that decay according to $\pi^{\pm} \to \mu^{\pm} + \nu$ and $\pi^0 \to \gamma\gamma$. The hadronic and electromagnetic components of showers fluctuate grossly event by event.

The HCAL thus provides information on the position of a particle, energy and arrival time. It is made as hermetic as possible, which allows indirect measurements of non-interacting particles. This is thanks to the fact that the sum of all transverse momenta should equal one, which follows from momentum conservation and the knowledge that $\mathrm{p}_T^{\mathrm{initial}} = 0$. The missing transverse momentum is then defined as $\mathrm{p}_T^{miss} = \text{-}\Sigma_i\, p_T^i$, where the sum i runs over all track momenta.

[3]In a sampling calorimeter, the absorber material degrades the energy of the particle hitting the detector and this interaction produces a shower of particles. The absorber is alternated by layers of active material that produces the signals that could be read out.

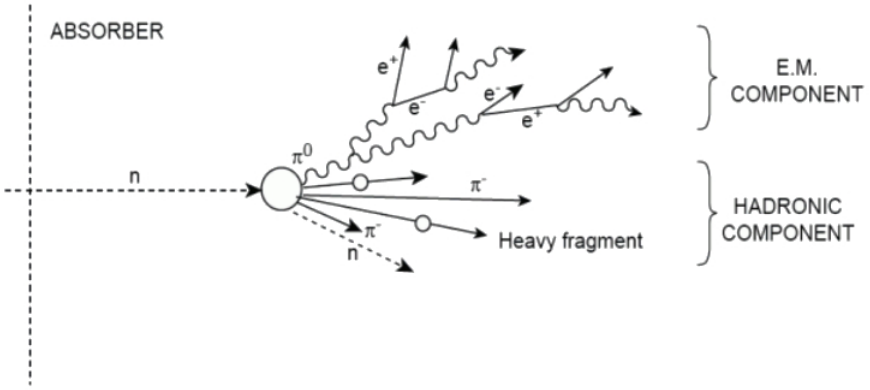

Figure 3.7: A neutron hitting the absorber material and starting a particle shower, with both an electromagnetic and hadronic component. [33]

3.2.4 The Superconducting Solenoidal Magnet

The superconducting magnet for CMS surrounds the tracker, the ECAL and the HCAL. It was designed to reach a 4-T magnetic field originating from a unique 4-layer solenoidal winding of NbTi conductor wires. The magnet is 6.4 m in diameter and 12.5 m in length, it weighs 220 metric tonnes. In order to reach the large magnetic field, very high currents must flow through the solenoidal wires. This is only possible if those wires are superconducting, which needs cooling of the magnet towards cryogenic temperatures of 4.5 K, done using liquid He.

A 4-T magnetic field of this size is truly remarkable. Particles with very high momentum originating from the interaction point are only bent in strong magnetic fields and this allows CMS to pinpoint a particle's momentum with high precision. Fig. 3.8 shows how different particles are bent under influence of the magnetic field, as well as the location of detection.

The solenoid is surrounded by a 12.5 t iron return yoke (displayed in red in Fig 3.4 and 3.8), which contains and guides the magnetic field. It also functions as the main support of the entire detector.

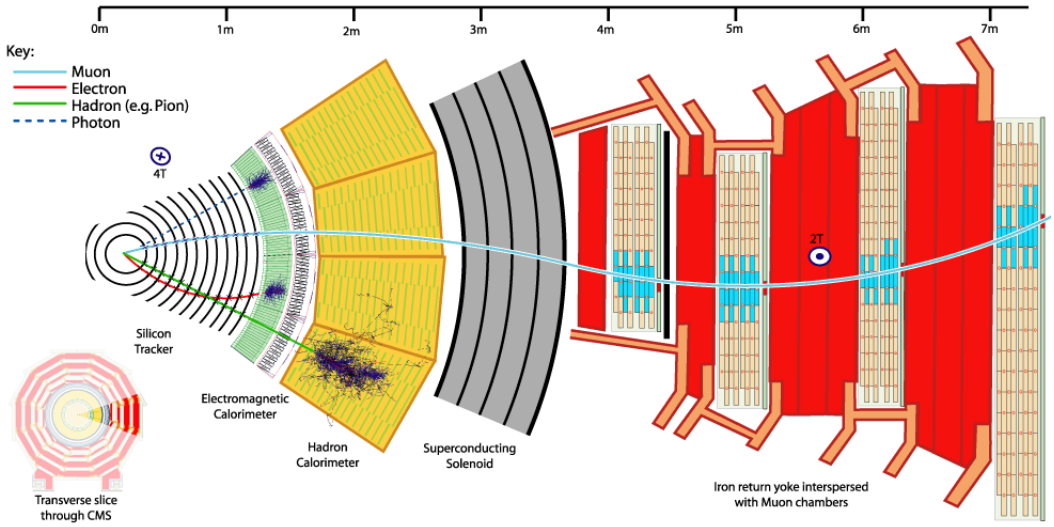

Figure 3.8: Schematic view of CMS along the beam axis. Different particles movement and interaction locations are displayed.

3.2.5 The Muon System

The detection of muons is of particular importance for CMS, as is clear from its name. CMS is designed in such a way that muon detection can be done with very high precision. Muons are not stopped by CMS's calorimeters. The muon system is installed at the outer edge of the detector, where they are likely to be the only particles left to register a signal. A particle is measured by fitting a trajectory to a track from hits created in the four muon stations, which are situated outside the magnet coil and have return yoke plates in between them (denoted in red in Fig. 3.8). This combined with the tracker hits at the core of the detector allows a particle's path to be precisely reconstructed, especially thanks to the high magnetic field to bend even the paths of very high-energy muons.

Hits in the muon chambers originate from a combination of three types of gaseous particle detectors:

(1) **Muon drift tubes**: These are rectangular shaped gaseous volumes (Ar/CO_2) whose edges consist of cathode strips and through which an anode wire runs. A charged particle passing through the volume generates ionisation around the particle track where positive ions and negative electrons respectively move to the

cathode and the anode. Stacking groups of drift tubes on top of each other, allows from timing measurements of charge collection time to reconstruct the path of the muon.

(2) **Cathode strip chambers**: These components are situated at the endcap disks of the detector. They consist of positively-charged anode wires who are perpendicularly crossed with negatively-charged cathode strips, all confined within a gas volume ($Ar/CO_2/CF_4$). Due to the particular setup of those chambers and the electrical fields applied, electrons generated from the ionisation process trigger an avalanche-effect allowing precise measurements of the particle's position.

(3) **Resistive plate chambers**: These components are installed both on the barrel and endcap sections of CMS. They consist of two parallel plates, a positively charged anode and a negatively charged cathode, both made of high resistivity material, separated by a gas volume ($C_2H_2F_4$/i-C_2H_{10}). They are also operated in avalanche mode and provide very fast detector timing.

3.2.6 Triggering and Data Acquisition

When bunch crossings take place each 25 ns, about 1 million pp collisions take place every second[4]. It is technically impossible to detect and read out all the data from each individual collision. Apart from technical reasons, plenty of those collisions are worthless as they might be low-energy collisions for instance, instead of highly energetic, and would be rejected from all interesting analyses in event selection. One clearly needs techniques to only select those events that are potentially interesting. Due to the tremendously high frequency of collisions, new events are happening, when the previous one did not even leave the detector yet. This is called **pile-up** and complicates the selection of interesting events, degrades measurements and sensitivity to new physics searches if analyses are not accoumpanied with sophisticated pile-up mitigation techniques.

Everything that gets measured by CMS needs to pass a set of initial criteria before further, more strict selection criteria are imposed on events in the high level trigger and in specific analyses. This process is called **triggering**. The triggering happens in two stages in CMS. The first stage is the Level 1 (L1) trigger [34] and the second stage is the High Level Trigger (HLT) [35], [36]. The L1 trigger makes use of the calorimetry and muon systems. Its decision is based on the presence of particle candidates such as electrons, muons, photons and jets above certain E_T or p_T tresholds. It effectively

[4]On average about 20-30 protons collide each bunch crossing.

reduces the 40 MHz event rate to 100 kHz. The HLT filters the rate even further to 100 Hz. The CMS DAQ/HLT system has the following functionality

- Read-out after a Level-1 trigger accept.
- Execute physics selection algorithms on the events that are read out. Accept those events that are physically most interesting.
- Forward these events towards mass storage for offline computing.

The HLT selection algorithms [36] use info from calorimeters, muon systems and pixel detectors. Then, the algorithms do primary vertex and full track reconstruction and b-tagging using secondary vertex identification (Fig. 3.5). It needs to be noted however, that to minimize the CPU required by the HLT, the algorithms only reconstruct the information partially. Full event reconstruction is done in offline computing.

Chapter 4

Modelling and Analysis Software

This chapter will provide an overview of the software used in this thesis to perform the necessary physics analyses. A general outline of the CMS Software (CMSSW) Application Framework will be given as well as an introduction to Monte Carlo (MC) event generators. An overview of the different data-types that are relevant may be beneficial:

- **RAW**: Detector data after it passed the L1 trigger and HLT selection criteria (see Sec. 3.2.6).
- **RECO**: Reconstructed objects (tracks, vertices, jets, leptons, etc.) from all stages of reconstruction.
- **AOD**: Subset of RECO data that is relevant for physics research in a convenient and compact format.
- **GEN**: Generated Monte Carlo (MC) data.
- **SIM**: Energy depositions of MC particles in the detector.
- **DIGI**: SIM hits converted into digitised detector response. This is the equivalent of RAW data, but here with simulated MC data.

4.1 CMSSW Application Framework

CMSSW [37] is a framework that provides the ability to deploy reconstruction and analysis software in order for physicists to be able to perform an analysis. It is built around an Event Data Model (EDM). An *event* in this context denotes a C++ object of

all RAW and reconstructed data for one particular collision. All the objects in such an event, are stored in a particular format called ROOT files. ROOT is an object-oriented framework aimed at solving the data analysis challenges of high-energy physics [38].

An important software toolkit used in CMSSW is `GEANT4` (GEometry ANd Tracking) [39]. It is a platform for simulation of passage of particles through matter. It is used in a large variety of high-energy physics experiments. For CMS in particular, it allows MC data to be reconstructed as if it were real data. This means effects taking into account the geometry of the detector that can influence the reconstructed events are included.

As was mentioned in Sec. 3.2.6, the 40 MHz event rate is reduced to about 100 Hz of RAW data events. This data is then processed towards RECO data objects. The latter dataset is still very large and contains irrelevant information for physics analyses and gets reduced to AOD data (Analysis Object Data).

4.2 Particle-flow Event Reconstruction

Particle-Flow (PF) [40, 41] is an algorithm to reconstruct all stable particles in an event by combining the kinematical information from the different CMS detector parts. Photons deposit their energy in the ECAL and are thus reconstructed from ECAL clusters. The energy of electrons is determined from a combination of the electron momentum acquired by the tracker, the energy deposited in the ECAL cluster and the total energy originating from Bremsstrahlung photons that are compatible with the electron track. The energy of muons is determined from curvature measurements of its track, obtained from tracker and muon system information. The energy of charged hadrons is measured from a combination of tracker and ECAL and HCAL cluster information, when both values are found to be compatible[1] And finally, the energy of neutral hadrons is obtained from ECAL and HCAL clusters.

4.3 Monte Carlo Event Generators

MC generators are indispensable in hadron collider physics research. They comprise of a set of models to simulate actual events from a particular process. For the LHC, when

[1] If the calorimeter response is to be too small, a cleaning procedure is performed to remove potential spurious or mis-reconstructed tracks. If, on the other hand, the calorimeter response is too large, the PF algorithm assigns the energy excess to a photon and possibly a neutral hadron.

two protons collide, a few very important things must be taken into account in order to produce a viable simulation of the interaction event. First of all, a **hard scattering process** must be implemented. This is the interaction between two partons (quarks or gluons) from each of the two protons. The hard scattering occurs at high momentum transfer and is described by the **matrix element** (ME). Furthermore, it can be computed in the perturbative regime thanks to the running of α_S (Sec. 1.2.3). Afterwards, the process of **parton showering** (PS) will start. This means that quarks and gluons originating from the hard scattering are propagated and radiate additional quarks and gluons and finally undergo hadronization. Here, a transition from perturbative to non-perturbative regime occurs since every additional radiation lowers the amount of transferred momentum. The sequential steps in this process can be modelled using dedicated Monte Carlo programs. This means the modelling is done in a probabilistic way, which is an accurate description of what happens in nature. An introduction on two concrete and distinct examples of MC programs, `POWHEG` and `PYTHIA`, will be given in order to gain a better understanding of their functionality and use.

4.3.1 Powheg

`POWHEG` [42], [43] is a Matrix Element (ME) Monte Carlo event generator. Given a particular process, e.g. $pp \to t\bar{t}$, it will generate all the possible Feynman diagrams that can give rise to the $t\bar{t}$ state at a particular order in perturbation theory[2]. It must be noted that this type of MC generators work in the perturbative regime. As was mentioned in Sec. 1.2.3, the strong coupling constant α_S is a running constant, meaning it becomes smaller the larger the amount of transferred momentum gets. As `POWHEG` simulates the collision of quarks or gluons from a pp collision, there is no momentum lost to radiative processes yet, so the value of transferred momentum is very high. A scattering event in this regime is called a **hard-scattering**.

`POWHEG` is able to calculate matrix elements up to Next-to-Leading-Order (NLO). This means that the generator also takes hard parton emission into account. Examples of LO and NLO diagrams are given in Figs. 4.1 and 4.2. They display examples of $t\bar{t}$-production diagrams, the f and $\bar{f}$ are a fermion and an anti-fermion[3]. Although the diagrams seem simple, NLO diagrams provide difficulties in theoretical calculations.

[2]To view which processes can be computed with `POWHEG`, see [44].

[3]The W-boson has multiple ways of decaying, e.g. $W \to l\nu$ or $W \to q\bar{q}'$

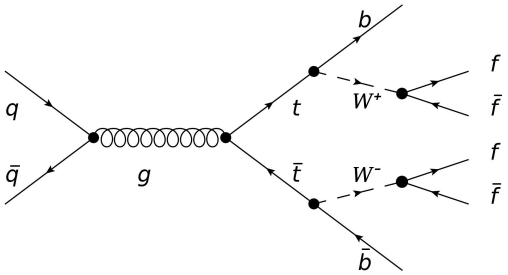

Figure 4.1: First order (LO) $t\bar{t}$ production process without additional radiations.

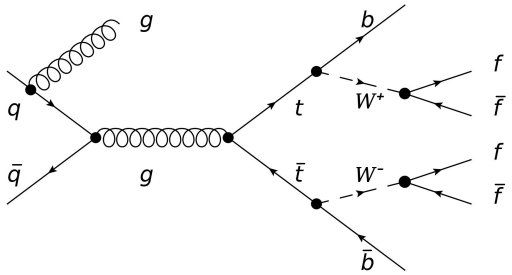

Figure 4.2: Example of a $t\bar{t}$ production process with a gluon radiating from one of the initial quarks. The gluon gives rise to an extra vertex, causing the diagram to be at NLO.

NLO diagrams provide not only positive, but also negative contributions to the cross-section. This makes it difficult to implement full NLO processes in MC generators. Another difficulty exists when the ME generator (e.g. `POWHEG`) is made to match with a PS code (e.g. `PYTHIA`). This is called **merging**, and will be explained in Sec. 4.3.2.

4.3.2 Pythia

`PYTHIA` [45] is used to generate high-energy-physics events: sets of outgoing particles produced from the interactions between two incoming particles. It comprises a collection of physics models for the evolution of a hard scattering process to a complex multihadronical final state[4]. The complexity stems also from the fact that many processes must be taken into account.

First of all, the original Feynman-diagrams receive *Strahlung-modifications*, in which $e \to \gamma e$ or $q \to gq$ type of processes result in additional final-state particles. Second, there are higher-order Feynman diagrams which sometimes combine to cancel divergences, resulting in perturbative techniques to become necessary. Typically this is only done up to one *loop*, which is referred to as an NLO-approximation. Third, due to confinement of quarks and gluons, no coloured particles can propagate freely. Therefore they must hadronize in colourless final states. This finally results in a collection of jets composed of photons, hadrons and leptons.

[4]Note that `PYTHIA` usually does not simulate the interaction itself but is typically used for the PS.

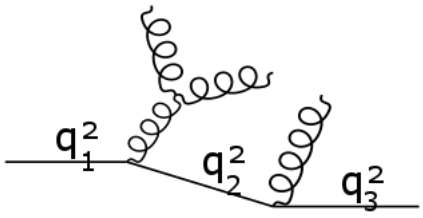

Figure 4.3: An example of a PS process calculated in PYTHIA. Starting of with a transferred momentum of q_1^2, the parton radiates gluons losing momentum to q_2^2, q_3^2, etc. Once the parton lost enough momentum and passed a certain cut-off momentum, it is left to hadronise into a colourless final state.

The entire problem can be summarised in two steps: first, the hard process is used as input to generate the corrections described in the previous paragraph and second it is left to hadronize. It is the task of PYTHIA to generate events (using MC techniques) such that its output (after simulation of the detector using GEANT4) is very similar to real data as measured by CMS. In typical data analysis, this is a very important aspect of the conducted study, since such generated events provide a tool for devising analysis strategies that can be used on real data. Furthermore they are of essential importance as they allow to model SM processes, make SM parameter predictions, and model backgrounds.

It was alluded in Sec. 4.3.1 that difficulties exist when the ME generator functions at NLO. Since PYTHIA indeed produces a PS it is possible that a PS produced from a LO diagram, coincides with a diagram produced in NLO (for an example of a PS, see Fig. 4.3). The concept of **merging** [46] solves this by including algorithms in the MC generators to prevent double counting, so that the same diagrams aren't added to the phase space[5].

4.3.3 Tuning of event-generators: Professor

Monte-Carlo event-generators use various approximations. To ensure the validity of those approximations, **tuning** is done on its parameters, to find a match between the predicted set of events compared to what's measured in data. With Eq. 1.8, we alluded that there was a perturbative and non-perturbative part to be taken into account to compute the cross section. Both the perturbative and the non-perturbative parts

[5]The phase space is the mathematical space of all possible momenta of all the outgoing particles.

could be tuned. The UE has many parameters that can not be calculated theoretically, therefore tuning becomes necessary to have these parameters implemented correctly. PS programs also have some tunable, free parameters such as α_S^{ISR}. There's multiple ways for doing so: either one does it manually which requires great skill and luck, or one does it using dedicated programs optimised for tuning MC-generators in the most efficient way.

Professor [47] is a program dedicated to tune model parameters of MC event-generators to experimental data by parametrising the per-bin generator response to parameter variations and numerically optimising the parametrised behaviour. Typical event-generators have $\mathcal{O}$(10-30) parameters that are relevant for collider physics simulations. It goes without saying that sampling in a multi-dimensional hyperspace is computationally very costly. If P is the number of parameters to be tuned, then for each variation of the P-element parameter vector $\mathbf{p} = (p_1, ..., p_P)$ a new event-generator computation would be necessary. The idea here, would be to define a goodness of fit (GoF) function between a limited set of MC data and the actual real data, and then to minimise that function corresponding to an optimal parameter vector $\mathbf{p}_{\mathrm{best}}$. A more elaborate discussion on the functioning of Professor can be found in appendix A.

Chapter 5

Analysis Part I: Search for Scalar Top Quark Partners

5.1 Introduction

The first part of the analyses done in this thesis revolves around a SUSY search for stop quark ($\tilde{t}\tilde{t}^*$) production conducted in the opposite sign dilepton channel at the LHC at $\sqrt{s} = 13$ TeV pp collisions. We look for the signal in which both W bosons decay leptonically (i.e. to ee, $\mu\mu$ or $e\mu$), hence the name: dilepton channel. It is depicted in Fig. 5.1.

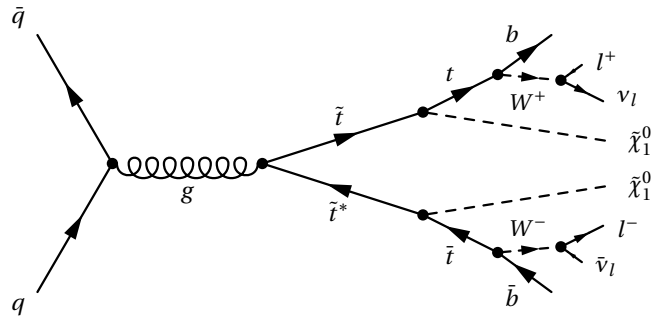

Figure 5.1: A hypothetical $\tilde{t}\tilde{t}^*$ pair is produced after a pp collision at the LHC. When assuming R-parity conservation, the stop quarks are produced in pairs and decay to a top quark and a neutralino (the latter is the LSP, invisible in our detector). The W bosons, originating from top quarks, both decay leptonically.

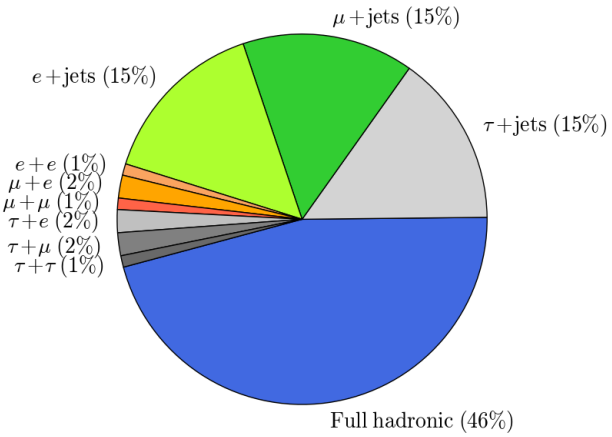

Figure 5.2: Branching fractions of top quark decay. Each time the decays of the two W bosons are denoted. Full hadronic means both the W-bosons decay into two quarks and thus produce jets. Note that the decay of the unstable τ-lepton as $\tau \to e/\mu + \nu_{e/\mu}$ has not been included.

The branching fractions of the top quark decay are given in Fig. 5.2. It is clear that the dilepton channel accounts for only a small fraction of top pair decays (9%). The full hadronic channel for example, accounts for a branching of 46%. There are plenty of processes that have large jet activity making it difficult to discriminate signal from background. The dilepton channel on the other hand produces electrons or muons[1]. Those are very easily detectable with the CMS ECAL (Sec. 3.2.2) and Muon systems (Sec. 3.2.5).

In SUSY-searches, there is another very important difference compared to regular SM-searches. There are no a priori predictions on the masses of the supersymmetric particles. This means that the energy available for the top quarks depends on the masses of the stop $\tilde{t}$ and neutralino $\tilde{\chi}_1^0$, which aren't known. One therefore always has to make a prediction on the mass difference $\Delta(m_{\tilde{t}}, m_{\tilde{\chi}_1^0})$. Depending on this mass difference, more or less energy will be available for top quark production and this will have a consequence on how energetic its decay products are.

A particularly difficult signal region to search for is the compressed signal, for which $\Delta(m_{\tilde{t}}, m_{\tilde{\chi}_1^0})$ is small. This means the energy available to the top quark is only 100

[1]The tau-lepton dominantly decays into electrons or muons through $\tau^- \to \nu_\tau + e^-/\mu^- + \bar{\nu}_e/\bar{\nu}_\mu$ and $\tau^+ \to \bar{\nu}_\tau + e^+/\mu^+ + \nu_e/\nu_\mu$.

GeV/c^2 compared to the 173.3 GeV/c^2 needed to produce it on-shell. The top quark will therefore be off-shell and produces very soft b quarks, leptons and neutrinos.

Due to the presence of two LSPs and two neutrinos from W decay, the signal has a large amount of E_T^{miss}, which will typically contain more E_T^{miss} than regular SM processes which can be exploited by constructing a particular type of variable, $M_{T2}(ll)$. This variable will provide a way of making a distinction between the signal region and the background region.

5.2 $M_{T2}(ll)$

We now introduce an important variable for this study called $M_{T2}(ll)$ [48] offering the possibility of selecting a signal region. The variable is defined by

$$M_{T2}^2(ll) = \min_{\mathbf{p}_{l1}^{\text{miss}}+\mathbf{p}_{l2}^{\text{miss}}=E_T^{\text{miss}}} \left(\max\left[M_T^2\left(\mathbf{p}_T^{l1}, \mathbf{p}_{l1}^{\text{miss}}\right), M_T^2\left(\mathbf{p}_T^{l2}, \mathbf{p}_{l2}^{\text{miss}}\right)\right]\right) \tag{5.1}$$

and is constructed as listed below. Note that the condition $\mathbf{p}_{l1}^{\text{miss}} + \mathbf{p}_{l2}^{\text{miss}} = E_T^{\text{miss}}$ means that $|\mathbf{p}_{l1}^{\text{miss}}| + |\mathbf{p}_{l2}^{\text{miss}}|$ must equal $E_T^{\text{miss}} = |\mathbf{p}_T^{\text{miss}}|$. The variable $\mathbf{p}_T^{\text{miss}}$ is defined in Sec. 3.2.3.

(**1**) The E_T^{miss} is partitioned into two hypothetical neutrinos with $\mathbf{p}_{l1}^{\text{miss}}$ and $\mathbf{p}_{l2}^{\text{miss}}$.

(**2**) The transverse mass M_T is computed for each lepton with one of the hypothetical neutrinos.

(**3**) The maximum of those two values is stored, the other is discarded.

(**4**) This is repeated for every partition of E_T^{miss} and then the minimum is taken. That value is the event's $M_{T2}(ll)$.

Note that if in the computation for $M_{T2}(ll)$ a maximum of 0 GeV/c^2 is found for a given partition of E_T^{miss}, $M_{T2}(ll) = 0$ GeV/c^2 will be kept. For a particular set of events this will always be the case when the E_T^{miss} lies within the smaller angle subtended by the $\mathbf{p}_T$ of the two leptons. For those events, a partition will be encountered with the two neutrinos aligned with the $\mathbf{p}_T$ of the leptons causing to yield a value of $M_T = 0$ GeV/c^2. Therefore a peak in the $M_{T2}(ll)$ spectrum at 0 GeV/c^2 will be typically seen.

For dileptonic $t\bar{t}$ and WW events (some of our SM backgrounds), it can be shown [49] that $M_{T2}(ll)$ has the same property for leptonic and single W events, namely that the

distribution has an endpoint at the mass of the W boson. However, two neutralinos as illustrated in the process in Fig. 5.1 give rise to additional E_T^{miss}. This will cause the partitioning of E_T^{miss} in Eq. 5.1 to create more energetic neutrinos than they actually are, thus causing $M_{T2}(ll)$ to possibly have a higher value than for example a regular $t\bar{t}$ process.

For top squark pair events, the distribution in $M_{T2}(ll)$ will depend on the value of $\Delta(m_{\tilde{t}}, m_{\tilde{\chi}_1^0})$. For large top squark masses, the neutralinos are boosted and this additional E_T^{miss} will push the $M_{T2}(ll)$ distribution past the value of M_W. If the mass difference between the top squark and top quark is small, the neutralinos will be produced relatively at rest and will cause the $M_{T2}(ll)$ distribution to look like the one found from SM $t\bar{t}$ events.

5.3 Analysis strategy

This section will provide an overview of the analysis strategy taken to construct an optimal selection[2]. The selection requires $p_T^{\text{lepton}} > 20$ GeV/c, $|\eta| < 2.4$, `miniRelIso` < 0.2 (see Sec. 5.5), $d_{xy} < 0.05$, $d_z < 0.1$ for the leptons, and $p_T^{\text{jet}} > 30$ GeV/c, $|\eta| < 2.4$ for the jets. An overview of the Feynman diagrams of the most important MC generated backgrounds (processes that give rise to the same signature as the signal) is given on page 56[3] .

It is easily seen from the Feynman diagram in Fig. 5.1 that we will have to put requirements on N_{jets} and $N_{\text{b-jets}}$. Therefore, at least two jets are required of which at least one is b-tagged.

The most dominant background consists of Drell-Yan (DY) production: two leptons with opposite signs originate from Z boson decay. It needs to be drastically reduced by applying specific cuts. A regular DY process does not have any E_T^{miss}. It is possible however, that a gluon radiates from the initial incoming quark pair. This produces a jet opposite to the lepton pair, as depicted in Fig. 5.3. If the p_T of this jet is over- or undermeasured in the detector, fake E_T^{miss} is reconstructed.

[2]The selection should leave the number of signal events as untouched as possible, but should reduce backgrounds as much as possible.

[3]The backgrounds from QCD- and $t\bar{t}$ + X production (with X a W or a H boson) are not given there but are also present in the analysis. They are very similar to process **(3)**, but with a W- or H-boson radiated from the top quark instead of a Z^0 boson.

Since we require at least two jets, it is possible that two gluons are radiated from the incoming quark pair, and thus their energies get overmeasured[4]. Depending on over- or undermeasurements, the E_T^{miss} is opposite to the jet or aligned with the jet. By requiring $\cos(\phi_{E_T^{\text{miss}}} - \phi_{\text{jet}_{1,2}}) < \cos(0.25)$, events with jets aligned and opposite to the E_T^{miss} will be omitted from the analysis. A second pair of cuts that effectively reduces DY is cutting directly on E_T^{miss} and the E_T^{miss}-significance (see Ref. [50]). The latter is defined by

$$E_T^{\text{miss}}\text{-significance} = \frac{E_T^{\text{miss}}}{\sqrt{H_T}} \tag{5.2}$$

with H_T equal to the sum of the p_T of all reconstructed jets. $\sqrt{H_T}$ is a measure for the resolution of the reconstructed E_T^{miss}. The chance that invisible particles contributed to E_T^{miss} is significantly higher if the value of E_T^{miss} is larger than its resolution. Requiring the event to have an E_T^{miss}-significance larger than a certain treshold reduces the DY background as the E_T^{miss} will be of the order of the resolution. This won't affect our signal as it should have a large E_T^{miss} due to the neutralinos.

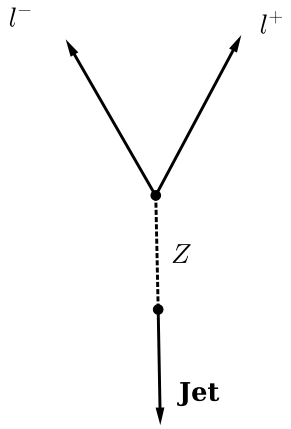

Figure 5.3: A jet radiating in the opposite direction of the lepton pair can get over- or undermeasured and account for *fake* E_T^{miss}. If the jet energy is overmeasured, we have $\Delta(\phi_{E_T^{\text{miss}}}, \phi_{\text{jet}}) \approx \pi$. If it is undermeasured, we have $\Delta(\phi_{E_T^{\text{miss}}}, \phi_{\text{jet}}) \approx 0$

[4]Jet mismeasurements occur from noise effects, varying detector response, pile-up contributions, etc.

To veto events in which the leptons originate from Z decay, a Z-veto cut is applied. Concretely, we require $|m_{ll} - m_Z| > 15$ GeV/c^2 for same flavour (SF) leptons with m_{ll} equal to the invariant mass constructed from both leptons. As the prompt leptons coming from W decay are highly energetic, a reconstructed invariant mass cut of $m_{ll} > 20$ GeV/c^2 is required.

All the applied cuts (including some that weren't mentioned, but are trivial) and their effect on the backgrounds and signal are given in Table 5.1 in a cutflow diagram. Notice how all backgrounds are efficiently reduced by the $M_{T2}(ll)$-cut except for $t\bar{t}$ + jets, $t\bar{t}$ + Z and $t\bar{t} + X$. The latter two are easily explained as they are irreducible backgrounds. This can be understood by looking at the $t\bar{t} + Z$ diagram **(5)** on page 56. The diagrams for $t\bar{t}$ + X are not given, but contain $t\bar{t} + W$ and $t\bar{t} + H$ production. If the Z boson or H boson decay gives rise to two neutrinos, then these backgrounds mimic our signal precisely causing them to end up in the high $M_{T2}(ll)$-tails. The presence of the $t\bar{t}$ + jets background is not easily explained and requires more attention (Sec. 5.4).

Cut	DY	$t\bar{t}$ + jets	$t\bar{t} + Z$	$t\bar{t} + X$	Single t
Two well reconstructed leptons	13333791.3	218650.8	496.2	884.5	20550.0
Opposite Sign ($e^{\pm}e^{\mp}, \mu^{\pm}\mu^{\mp}, e^{\pm}\mu^{\mp}$)	13281921.7	214128.7	450.0	687.6	19900.4
$m_{ll} > 20$ GeV/c^2	13189194.4	208590.9	439.6	673.3	19413.5
$\lvert m_{ll} - m_Z \rvert > 15$ GeV/c^2 for SF	1185896.0	185391.0	222.1	436.5	17378.8
≥ 2 jets	52475.3	137452.0	204.8	399.7	6497.2
≥ 1 b-tags	5048.1	108792.2	155.2	315.3	4567.2
$E_T^{\text{miss}} > 80$ GeV	84.2	44724.8	76.9	163.6	1940.3
$E_T^{\text{miss}}/\sqrt{H_T} > 5$	61.0	41028.4	63.3	130.1	1814.0
$\cos(\phi_{E_T^{\text{miss}}} - \phi_{\text{jet}_{1,2}}) < \cos(0.25)$	46.9	38318.5	58.2	119.1	1699.0
$M_{T2}(ll) > 140$ GeV/c^2	0.4	2.9	1.6	1.1	0.6
Cut	W + jets	Diboson	Triboson	QCD	Signal
Two well reconstructed leptons	5554.2	39734.0	142.7	255025.4	296.8
Opposite Sign ($e^{\pm}e^{\mp}, \mu^{\pm}\mu^{\mp}, e^{\pm}\mu^{\mp}$)	3679.0	38301.2	132.1	233498.5	293.5
$m_{ll} > 20$ GeV/c^2	3357.3	37437.8	131.1	37467.9	291.1
$\lvert m_{ll} - m_Z \rvert > 15$ GeV/c^2 for SF	3140.3	18819.1	48.1	36338.5	261.1
≥ 2 jets	928.4	2475.6	28.4	1860.0	206.0
≥ 1 b-tags	86.7	206.7	5.6	67.3	168.7
$E_T^{\text{miss}} > 80$ GeV	16.8	54.7	2.7	0.0	149.8
$E_T^{\text{miss}}/\sqrt{H_T} > 5$	14.9	50.4	2.4	0.0	146.3
$\cos(\phi_{E_T^{\text{miss}}} - \phi_{\text{jet}_{1,2}}) < \cos(0.25)$	13.3	47.8	2.3	0.0	136.4
$M_{T2}(ll) > 140$ GeV/c^2	0.1	0.3	0.0	0.0	26.1

Table 5.1: Cutflow-diagram of the applied cuts in the selection for the OS dilepton $\tilde{t}\tilde{t}^*$-search. The numbers represent the number of MC events produced. The signal is found on the bottom right, the precise value of $\Delta(m_{\tilde{t}}, m_{\tilde{\chi}_1^0})$ is not given here as it is of less importance. © Schöfbeck R.

(1) Drell-Yan production

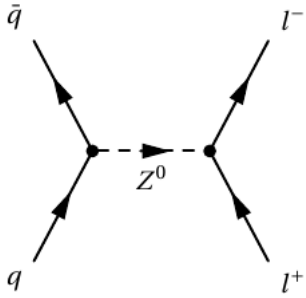

(2) $t\bar{t}$ + jets production

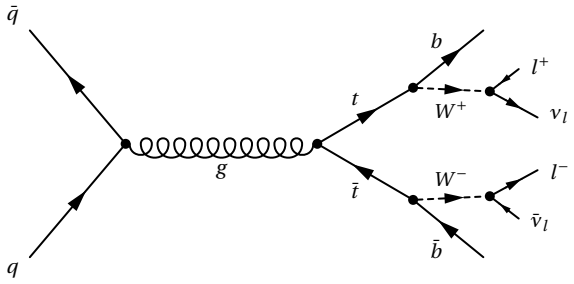

(3) Single top production

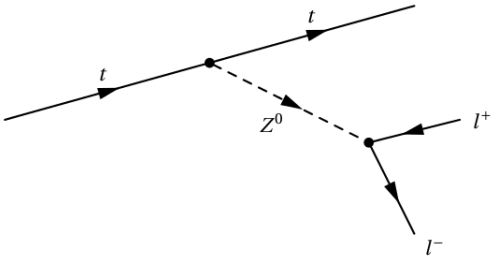

(4) W + jets production

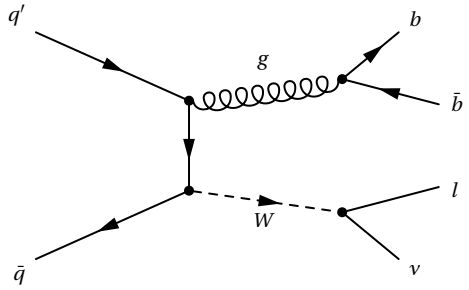

(5) $t\bar{t}$ + Z production

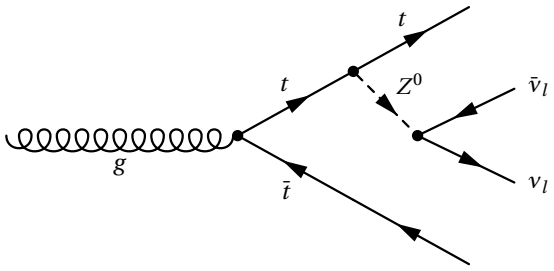

(6) Diboson production

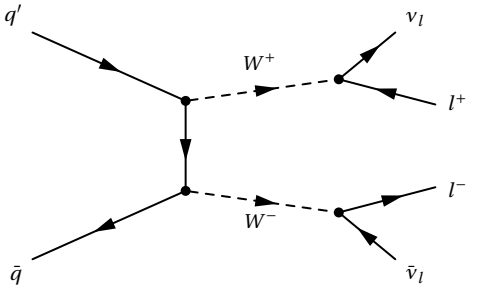

(7) Triboson production

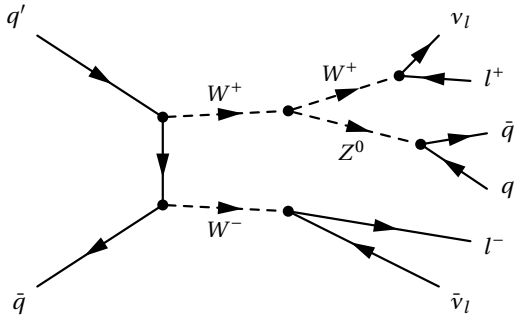

5.4 $M_{T2}(ll)$-tail events study for the $t\bar{t}$ + jets background

The large amount of $t\bar{t}$ + jets events in the tails of $M_{T2}(ll)$ is worrying. This is due to the fact that following from Eq. 5.1 no $t\bar{t}$ events should end up in the high tails since the only E_T^{miss} can originate from the two neutrinos. We define the high-tail region as $M_{T2}(ll) > 140$ GeV/c^2. For this region an explicit check will be done to find out what the kinematics of $t\bar{t}$ + jets events exactly look like in full detail. The $t\bar{t}$ + jets background in function of $M_{T2}(ll)$ is displayed in Fig. 5.4.

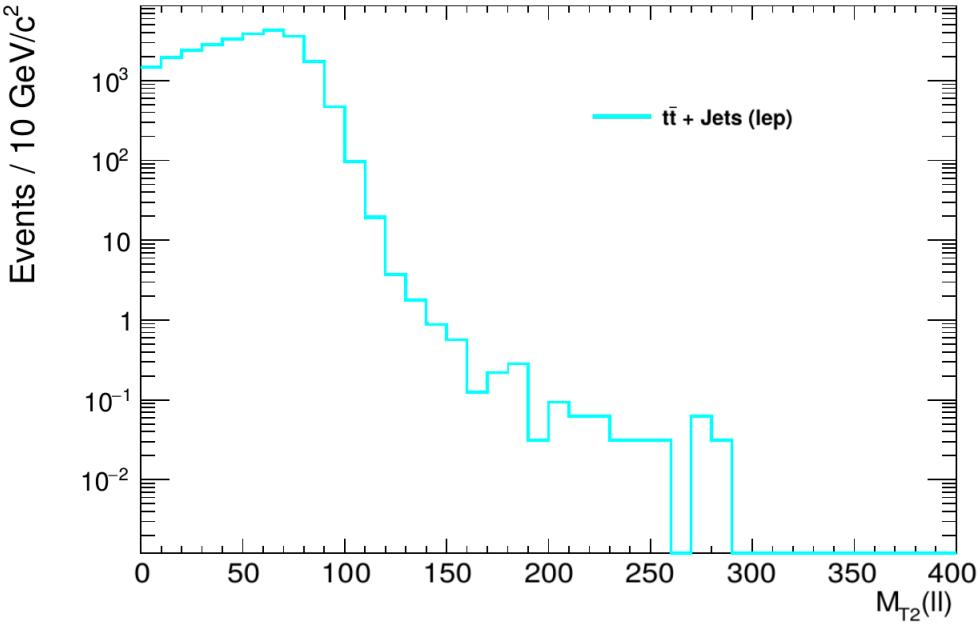

Figure 5.4: Number of $t\bar{t}$ + jets events in function of $M_{T2}(ll)$. The expected cut-off around 80 GeV/c^2 is visible (notice the log scale), however there are still events surviving into the high-tail region (> 140 GeV/c^2).

A huge advantage in this study, is that in MC we have access to the generated particle's kinematical information (GEN info), which is not the case in data. We can thus explicitly see if something went wrong in the process of reconstructing the particles. In reconstruction (RECO), the interactions in the detector are also accounted for, which inevitably causes incorrect reconstructions of particles. We are particularly interested in the leptons that were selected as the prompt leptons to see whether they are in fact the decay products of the W bosons. If not, we are selecting the wrong leptons to compute the event's $M_{T2}(ll)$ and that could explain why we see events ending up in the high tails.

GEN - Level

Access to **simulated** kinematical information.
→ Monte Carlo ✓

$\Longleftrightarrow$

RECO - Level

Access to **reconstructed** kinematical information.
→ Monte Carlo ✓
→ Data ✓

In the tail-region ($M_{T2}(ll) > 140$ GeV/c^2), 37 $t\bar{t}$ + jets events are counted. For those events, the GEN-information is matched to the RECO-information, of which an example is displayed in Table 5.2. This means that for each of the two RECO leptons, the corresponding GEN lepton is identified. For the GEN leptons, the `PdgIds`[5] of the mother particles are checked (the one from which the lepton decayed). Once these are found and one or more are not a W boson, the mother particle (e.g. a b quark) is again

RECO Leptons			
Lepton	p_T GeV/c	ϕ	η
(1) μ	90.660	0.294	0.937
(2) e	63.470	0.314	1.637

GEN Leptons						
Lepton	p_T GeV/c	ϕ	η	$\Delta R : l^{\mathrm{RECO}}_{(1)}$	$\Delta R : l^{\mathrm{RECO}}_{(2)}$	Mother
(1) μ	89.290	0.294	0.937	**0.000**	0.699	W
(2) e	37.590	0.314	1.637	0.701	**0.002**	b

GEN Quarks					
Quark	p_T GeV/c	ϕ	η	$\Delta R : l^{\mathrm{RECO}}_{(1)}$	$\Delta R : l^{\mathrm{RECO}}_{(2)}$
b	131.86	0.340	1.647	0.712	**0.029**

Table 5.2: Example of how the GEN-RECO matching for a high-tail $M_{T2}(ll)$ $t\bar{t}$ + jets event is done. First the RECO leptons are matched to the GEN leptons, based on demanding $\Delta R = \sqrt{\Delta\phi^2 + \Delta\eta^2} \approx 0$. Then the `PdgId` of the GEN leptons is checked to what the mother particle of the leptons is. If it is found that this is a b quark and $\Delta R(l^{\mathrm{RECO}}|b) < 0.06$, the b quark is said to be matched to the lepton, indicating that the lepton originated from a b-decay. The matched leptons and b quark are shown by the interconnecting lines.

[5]The `PdgIds` are the conventional numbering IDs for all elementary particles set by Particle Data Group [51].

matched to its corresponding lepton based on the fact that their separation should not be larger than $\Delta R = 0.06$.

Of the 37 high-tail events, 29 out of 37 events have at least one selected lepton decayed from a b quark and not a W boson and 8 out of 37 events are originating from W decay. This means that ≈80% of $M_{T2}(ll)$ tail events are fakes; namely wrongly selected leptons or **fakes**.

5.5 Reduction of the $t\bar{t}$ + jets background

In order to reduce the fakes in the high tails of $M_{T2}(ll)$, an efficient way of making a distinction between leptons originating from a W boson compared to a b quark decay must be found. A first suggestion is to use the `Reliso0X` variable. It is constructed for every selected lepton by drawing a circle of $\Delta R = 0.\text{X}$ in the angle space with center around the lepton's track and by computing

$$\text{RelIso0X} = \frac{\sum_{i \in \text{all RECO particles}} p_T^i}{p_T^{\text{lep}}} \tag{5.3}$$

where i only runs over p_Ts that are inside the predefined circle as shown in Fig. 5.5 (a). Since leptons that originate from b quarks will typically have lots of jet activity in their vicinity, a `RelIso0X` $< Y$ cut can reduce the contribution of those leptons. A rather small cone (also referred to as `MiniRelIso`) does not help reducing the fakes in the tails. The idea is that a lepton can be accidentally[6] radiated away from the jet activity (see Fig. 5.5 (b)) and a small cone cannot catch enough jet tracks for the event to fail the cut. If one however adds a `Reliso04` < 0.12 cut, where a larger cone size of 0.4 is chosen, approximately 80% of fakes in the tails can be reduced [52]. The problem with this approach, however, is that this also touches prompt leptons (those who originate from W decay). It seems that the `RelIso04` < 0.12 cut is not a good choice after all. A new variable, that leaves the prompt leptons untouched, but removes specifically those originating from semileptonic b quark decay, must be constructed.

[6]This might seem to be unlikely, but we are looking at events in high tails of $M_{T2}(ll)$, so we expect things to be unlikely!

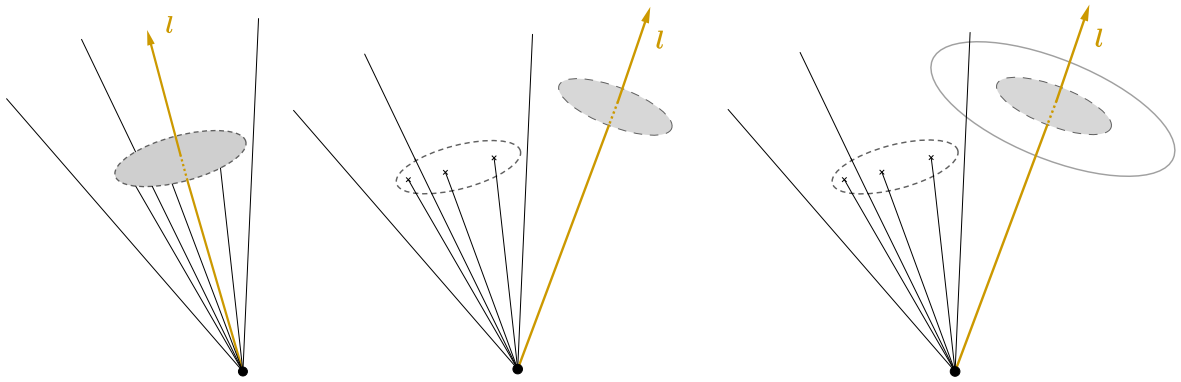

(a) (b) (c)

Figure 5.5: Display of the RelIso0X approach with conesize 0.X for (a) a lepton near jet activity (usual case), (b) a lepton radiated away from jet activity with conesize 0.X and (c) a lepton ejected away from jet activity with a conesize 0.Y > 0.X.

This new approach is to construct the `MultiIsoV2` variable, defined as

$$\texttt{MultiIsoV2} = \texttt{MiniRelIso} < \text{A} \;\&\&\; (\texttt{ptRatioV2} > B \parallel \texttt{ptRelV2} > \text{C})\,. \tag{5.4}$$

It contains three components, explained below:

- `MiniRelIso`: This is the same principle as `RelIso`, but corrected for boosts. The cone size gets a p_T dependence: the higher the p_T of the lepton is, the smaller the cone size necessary to catch jet activity as the jet will have a much smaller opening angle.
- `ptRatioV2`: It is defined as $p_T^{lep}/p_T^{\text{Jet}}$, where the closest jet to the lepton is considered. If the lepton has a significantly larger p_T than the jet, chances are small it originated from the b quark.
- `ptRelV2`: It is defined as $\|\vec{p}_T^{\,lep} - \vec{p}_T^{\,\text{Jet}}\|$ and is displayed in Fig. 5.6a. The larger this value, the further the lepton will be separated from the jet, so the smaller the chances are it originated from the b quark.

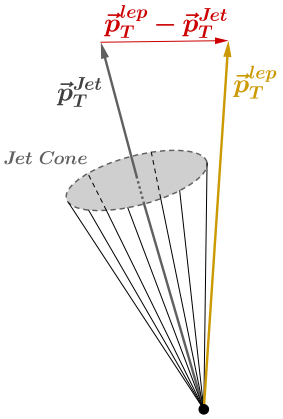

(a) Display of how `ptRelV2` is computed.

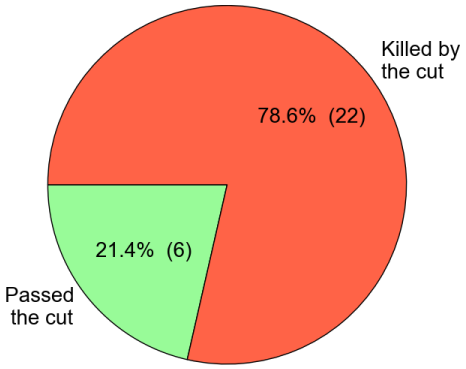

(b) Approximately 80% of fake high tail $t\bar{t}$ + jets events are killed by the `MultiIsoV2` cut.

Figure 5.6

The `MultiIsoV2` cut acting on the $t\bar{t}$ + jets background is displayed in Fig. 5.7. Here, A, B, C were taken to be respectively 0.09, 0.84, 7.2. It's clear how the low $M_{T2}(ll)$ region gets reduced by about 15%, but from about 110 GeV/c^2 onwards, a clear reduction of tail events becomes visible.

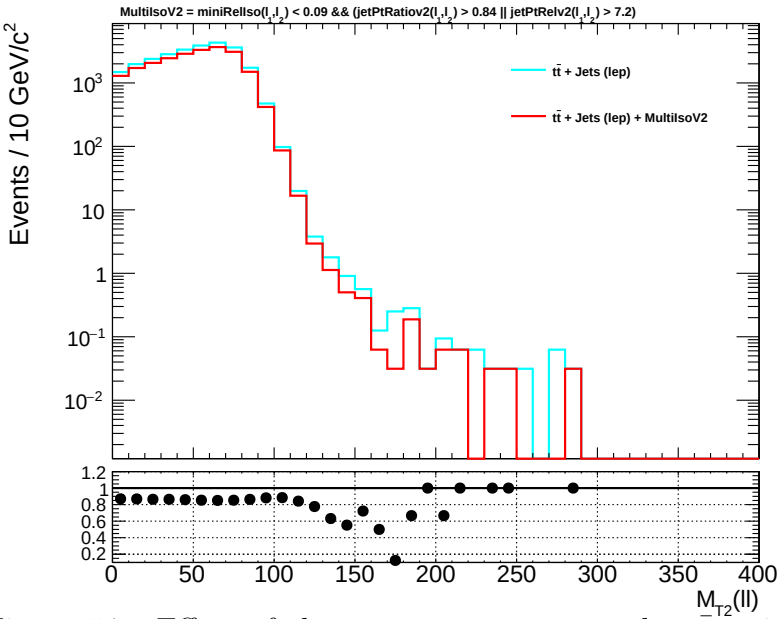

Figure 5.7: Effect of the `MultiIsoV2` cut on the $t\bar{t}$ + jets background in the $M_{T2}(ll)$ distribution before the cut (cyan) and after the cut (red).

`MultiIsoV2` thus effectively reduces fakes in the high $M_{T2}(ll)$ region (≈80%, see Fig. 5.6b). Over the entire $M_{T2}(ll)$ spectrum, the $t\bar{t}$ + jets background is reduced by approximately 48% and the signal only loses about 4% [52].

5.6 Summary and Discussion

In this section, an analysis is presented within the scope of an opposite sign SUSY-search for stop quarks, with the production process depicted in Fig. 5.1. An overview of the analysis strategy is given along with the most important cuts that need to be applied in order to reduce background processes as much as possible. Their effect can be seen in the cutflow-diagram presented in Table 5.1. The various backgrounds that have to be taken into account are presented with their corresponding Feynman diagrams on page 56.

It is noted that the $t\bar{t}$ + jets background requires extra attention. This can be seen from Fig. 5.4 and also from the cutflow-diagram in Table 5.1 where $t\bar{t}$ + jets events appear in the high tails of $M_{T2}(ll)$ (> 140 GeV/c^2). As is explained in Sec. 5.2, events originating from a SM $t\bar{t}$ process shouldn't be found for high values of $M_{T2}(ll)$. To find which selected leptons are present in the high-tails, GEN information is compared to RECO information to identify the mother particles of the selected leptons. An example of this is given in Table 5.2. It is found that 29 out of 37 events in the tails have leptons originating from a b quark instead of a W boson. This means that for those events, the wrong leptons are selected, and should be categorized as fakes.

Two approaches are suggested to reduce the fakes in the tails. The first, adding a `RelIso04` < 0.12 cut, does not turn out to be efficient as also prompt leptons are touched by it. This is presented in [52]. Therefore, a `MultiIsoV2` cut is added instead as defined in Eq. 5.4. This cut seems to be very efficient in reducing the tails and leaves the signal untouched. The $t\bar{t}$ + jets background is reduced by 48% in total with a loss of 80% in the tails and the signal is only reduced by 4% in the tails. This can also be seen from the pie chart in Fig. 5.6b (b) and Fig. 5.7.

Chapter 6

Analysis Part II: Parton Shower Tuning in Modelling Top Quark Pairs

6.1 Introduction

MC event generators in high energy physics employ various physics models to describe a large variety of different types of processes [53]. Their results are used to devise search strategies or background estimates of physical processes to allow theoretical interpretations of experimental results. MC generators should provide a good description of available data, providing confidence in the theoretical models underlying the generator performance. Due to the large amount of data available from the LHC and previous experiments, experimental uncertainties have become more precise. This allows detailed studies on the validity of MC simulations and **tuning** (Sec. 4.3.3) efforts pave the way towards new and more precise predictions. The free parameters of these models need to be tuned from distributions of suitable observables extracted from experimental measurements.

It has been known that the N_{jets} observable as depicted in Fig. 6.1 is not well simulated by `PYTHIA8`, causing inaccurate MC outputs. Overestimation of MC events (generated with `POWHEG`+`PYTHIA8`) with respect to data becomes visible for larger N_{jets} bins. This has also been observed with 13 TeV data (in the dilepton channel [54] and the single lepton channel [55]) as well as with `MADGRAPH5_aMC@NLO`+`PYTHIA8` in both FxFx and MLM configurations[1]. Among others, two main causes for this are identified: (1) The

[1]Those are two merging schemes used in `MADGRAPH5_aMC@NLO` for NLO and LO cases respectively,

matching scheme between POWHEG and PYTHIA8, or (2) some of the PYTHIA8 parameters are not optimal, where a combination of both issues might be a possibility too. In this particular study, an effort is made to explore whether solutions can be found using dedicated tools to perform a tune on one of the parameters in PYTHIA8.

To tackle this issue, α_S^{ISR}, a PYTHIA8 parameter that controls Initial State Radiation (ISR) effects in the parton shower process could be tuned [56]. The tuning tool used is Professor [47], a program for tuning model parameters of MC event generators to experimental data by parametrising the per-bin generator response to parameter variations and numerically optimising parametrised behaviour. More information on the functioning of *Professor* can be found in Appendix A.

The POWHEG event generator provides a matrix element calculation of the $pp \to t\bar{t}$ up to an additional jet (not present in the LO calculation) matched to parton shower MC programs (in our case PYTHIA8).

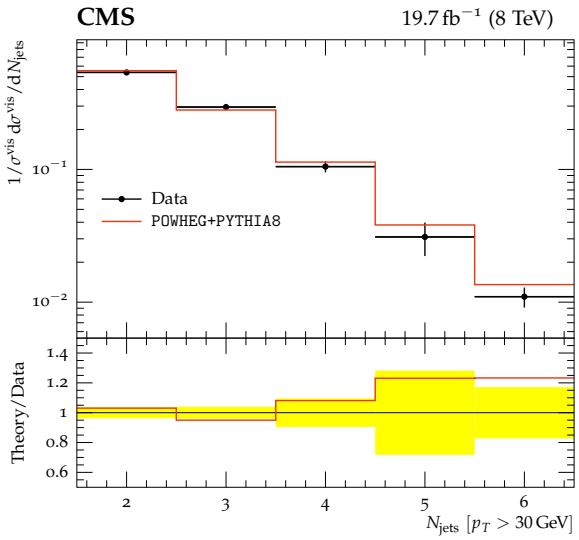

Figure 6.1: Normalised $t\bar{t}$ Cross-section in the dilepton channel in function of N_{jets} ($p_T > 30$ GeV) for $\sqrt{s} = 8$ TeV (black) and the POWHEG+PYTHIA8 MC generator output (red).

see Sec. 4.3.2 for a brief discussion on merging.

6.2 Tuning of α_S^{ISR}

In this study, we tune the `SpaceShower:alphaSvalue` parameter[2] of `PYTHIA8`, here denoted by α_S^{ISR}. 13 MC runs are generated for different values of α_S^{ISR}. The used values are listed in Table 6.1.

Run	0	1	2	3	4	5	6
α_S^{ISR}	0.100	0.105	0.110	0.115	0.120	0.125	0.130
Run	7	8	9	10	11	12	
α_S^{ISR}	0.135	0.140	0.145	0.020	0.050	0.080	

Table 6.1: Tabular overview of 13 MC runs for different values of α_S^{ISR}.

For runs 0-9, $\alpha_S^{\mathrm{ISR}} \in [0.100, 0.145]$ is chosen, since it is expected that α_S^{ISR} would lie in between these bounds. For runs 10-12 however, smaller values are selected to make sure the tuning would not navigate towards them, which would clearly be a wrong result.

Briefly, the *Professor* method goes as follows. A MC response function $MC_b(\mathbf{p})$ is constructed for every observable's bin b. Afterwards, for every point $\mathbf{p}$ in parameter space, a χ^2 function is constructed according to

$$\chi^2(\mathbf{p}) = \sum_{\mathcal{O}} \sum_{b \in \mathcal{O}} \frac{(MC_b(\mathbf{p}) - \mathcal{R}_b)}{\Delta_b^2}, \tag{6.1}$$

where $\mathcal{O}$ denotes the observable, $\mathcal{R}_b$ the data at bin b, and Δ_b^2 the total uncertainty originating from the quadrature sum of MC-uncertainty and data-uncertainty. Note that this formula corresponds to Eq. A.7 from Chapter A, with the weights w_i chosen equal to 1. For every parameter point $\mathbf{p}$, the χ^2 is then interpolated and eventually minimised. The value of $\mathbf{p}$ corresponding to a minimal χ^2, $\mathbf{p}_{\mathrm{best}}$ (here $\alpha_{S,\mathrm{best}}^{\mathrm{ISR}}$) is the final tune.

This study selects four observables to which a tune can be performed. They are N_{jets} for $p_T > 30,\ 60$ and 100 GeV/c and subleading additional[3] jet p_T. Varying the values of α_S^{ISR} for different MC-runs yields a different output in each observable bin. The outliers

[2]For a full list of the `PYTHIA8` parameters, refer to [57].

[3]The subleading additional jet denotes the fourth most energetic jet in the dilepton channel. The two b-jets and one ISR-jet are produced in `POWHEG` (at NLO) and are not sensitive to α_S^{ISR}.

of the α_S^{ISR} variations are called envelopes and are displayed in Figs. 6.2 (a), (b), (c) and (d).

Of the four observables, three are used to conduct three tuning efforts. They are listed below.

1	N_{jets} $[p_T > 30$ GeV$]$
2	N_{jets} $[p_T > 60$ GeV$]$
3	N_{jets} $[p_T > 30$ GeV$]$ and Subleading additional jet p_T

Table 6.2: Different observables used for tuning. They are also displayed in Fig. 6.2.

For each of the three tuning efforts, *Professor* performs a tune towards the observables mentioned in Table 6.2. In case of the N_{jets}-observables, only bins with $N_{\mathrm{jets}} > 3$ are considered in the tuning process, where jets predominantly originate from the parton shower and hence these bins are sensitive to α_S^{ISR}. Note that the distribution N_{jets} ($p_T >$ 100 GeV) displayed in Fig. 6.2 (c) is not used in either of the combinations given in Table 6.2. The CMS analysis code used is from TOP-12-041 [58] along with the *Rivet* routine `CMS_2015_I1397174`.

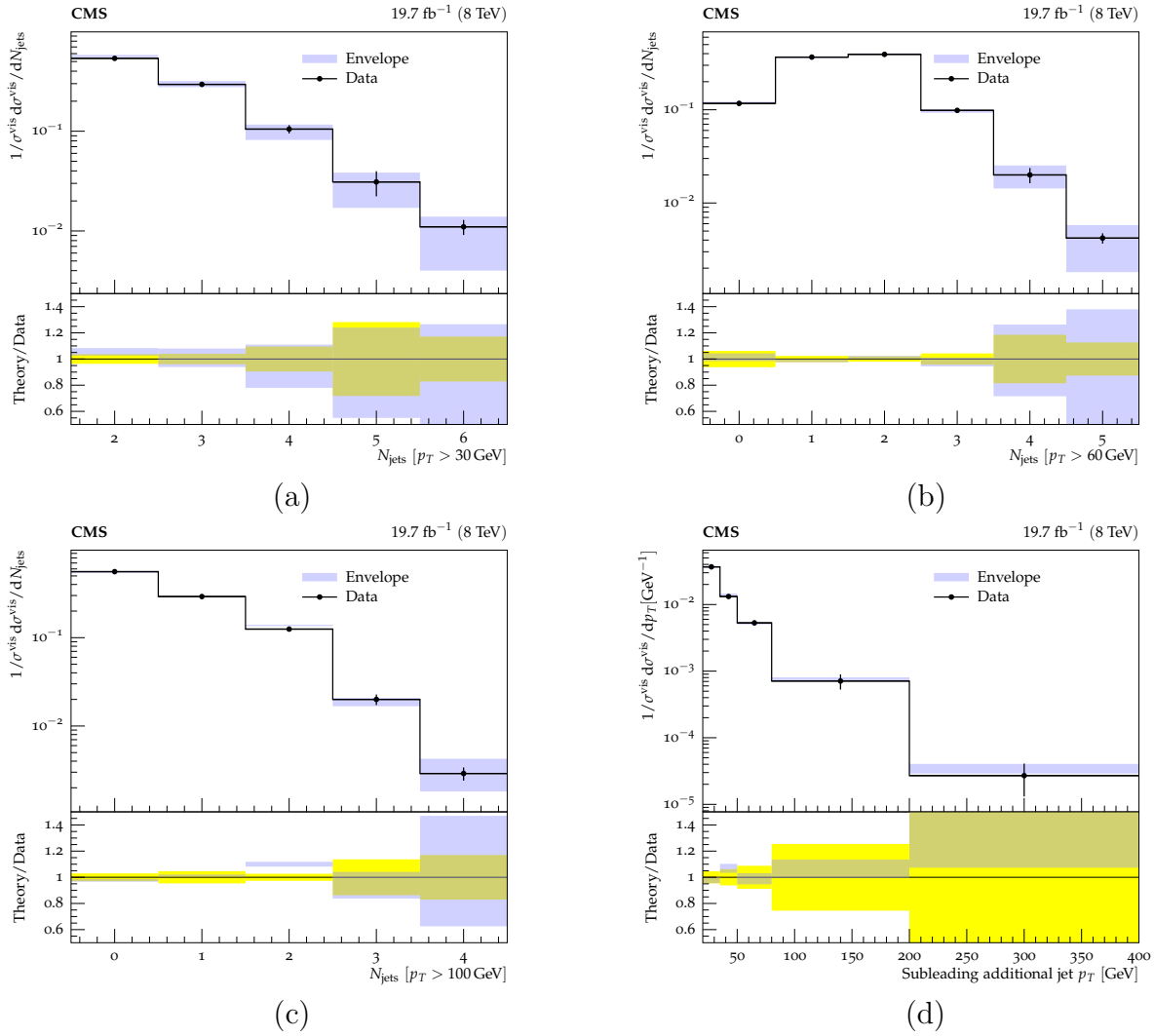

Figure 6.2: Envelope-plots for the four different possible observables that can be used for tuning. The blue bands denote how MC variations in α_S^{ISR} from Table 6.1 overlap with the data. The yellow bands display the data uncertainties.

6.3 Estimation of uncertainty on α_S^{ISR}

Uncertainties on the tuned value of α_S^{ISR} are estimated in two ways. The first method (**1**) is to consider the data uncertainties. For each observable combination, two additional datasets are constructed by varying the central data up with the upper error, and varying it down with the lower error. After this, the three datasets are used to perform three tunes. The resulting tune using the central dataset is the central tune result. The ones resulting from the upwards scaled and downwards scaled datasets are the respective upper and lower bounds of the central tune results[4].

The second method (**2**) is to construct two eigentunes for each tune result[5]. The parameter-space used here is one-dimensional and thus the eigentunes are found by varying the tuned result up and down with the value of the χ^2 (this is the standard *Professor*-prescription). The values of α_S^{ISR} corresponding to those variations are then its upper and lower bounds. The results can eventually be displayed for the studied observables alongside the central tune. A more thorough explanation on the construction of eigentunes is given in Appendix A.3.

6.4 Results

Result	α_S^{ISR} (central)	Uncertainties (**1**)	Percentages
1	0.115	+0.021	18.635%
		-0.019	19.048%
2	0.104	+0.014	13.114%
		-0.012	11.555%
3	0.113	+0.029	25.402%
		-0.021	18.296%

Table 6.3: of the tuning results taking the three different tunings as listed in Table 6.2 as input.

The result of each tuning is summarised in Table 6.3. For each tuning one, the central tuning result is given along with its uncertainties according to method (**1**) described in Sec. 6.3, both in absolute values as percentages. The *Professor* output from taking the eigentunes into account, according to method (**2**), are omitted for this set of tuning

[4]Note that for the upwards and downwards scaled datasets, the uncertainties in data are kept constant.

[5]This can be done using the *–eigentunes* option in the *prof-tune* command.

efforts. The reason for this is that the tuning is done to only one or two distributions at most for typically a low amount of degrees of freedom. Therefore the resulting χ^2 is small and varying up the χ^2 by itself to acquire the errors yields unrealistically low uncertainties on the tuned value of α_S^{ISR}.

The results are displayed in Figs. 6.4, 6.5 and 6.6. The resulting tunes are displayed in Fig 6.3, along with the ATLAS ATTBAR-POWHEG tune [59], the `PYTHIA8` (CUETP8M1) and `PYTHIA6` (CTEQ5M) defaults. Due to the large data-uncertainties on the subleading additional jet p_T observable, it isn't taken into account for the further remaining part of the study. The optimal tuning result is chosen to be combination 1 in which the tuning towards the N_{jets} ($p_T > 30$ GeV) distribution was performed as its result lies well within experimental data-uncertainties independent of the jet p_T treshold. The value of $\alpha_S^{\mathrm{ISR}} = 0.115^{+0.021}_{-0.019}$ is thus considered to be the optimal tune.

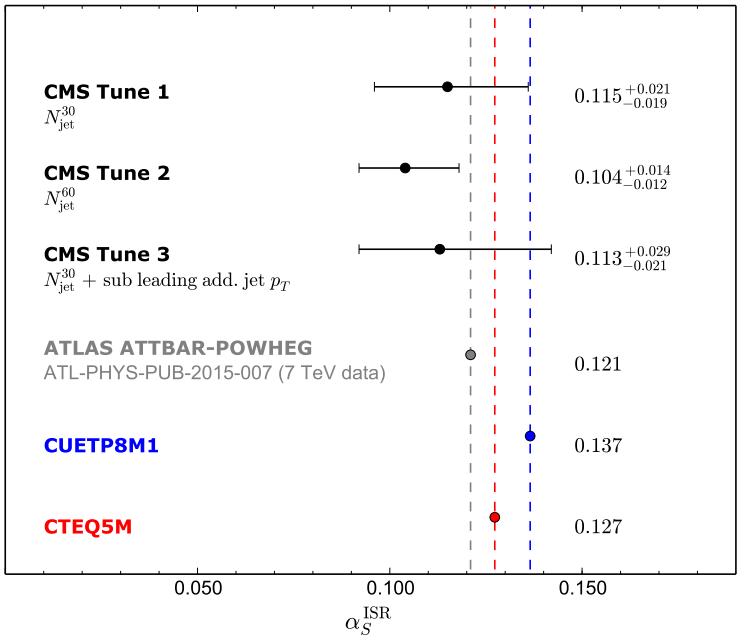

Figure 6.3: Summary of tune results and their uncertainties. Two alternative tunes are presented in addition to the previously described one. The input distribution(s) for each tune is indicated below the label of each tune. The α_S^{ISR} values in the ATLAS ATTBAR-POWHEG tune for `PYTHIA8`, the CMS CUETP8M1 tune for `PYTHIA8` (CMS default in Run II), and the CMS Z2* `PYTHIA6` tune (CMS default in Run I), using the CTEQ5M PDF set, are also displayed.

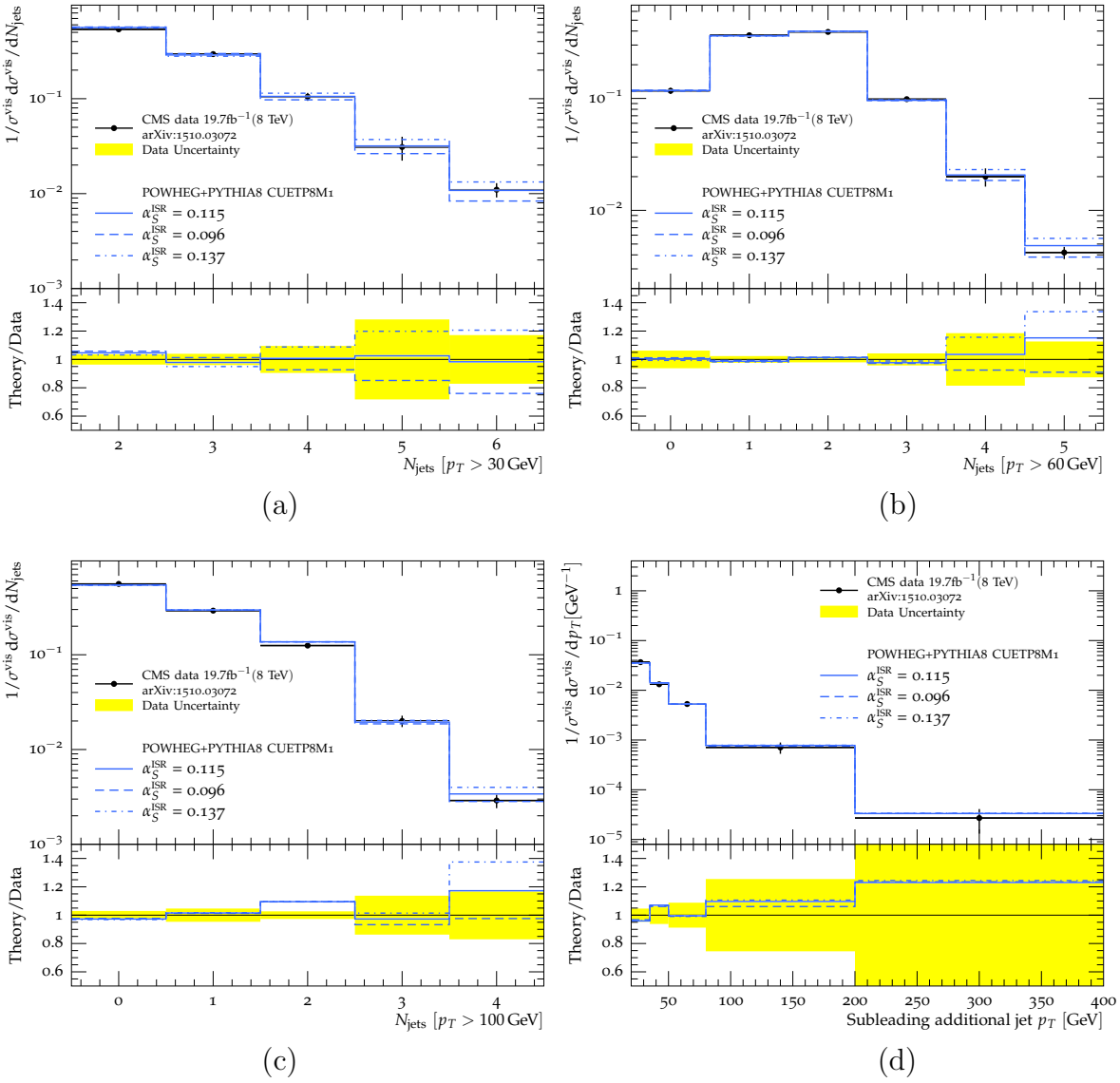

Figure 6.4: Results of $\alpha_S^{\rm ISR}$ tuning 1. Jet multiplicity distribution, $N_{\rm jets}$ (with $p_T^{jet} > 30$ GeV), after tuning $\alpha_S^{\rm ISR}$ with the $N_{\rm jets} > 3$ bins (where jets predominantly originate from the parton shower) is used as input to *Professor* [47]. The unfolded CMS data are shown with total error bars. In each plot, the calculated distribution assuming the tuned $\alpha_S^{\rm ISR}$ is shown (solid line). The calculated distributions with the lower bound (dashed line) and the upper bound (dot-dashed line) of the tuned $\alpha_S^{\rm ISR}$ are also displayed. Beneath each plot is shown the ratio of theory predictions to data. The yellow bands indicate the total data uncertainty.

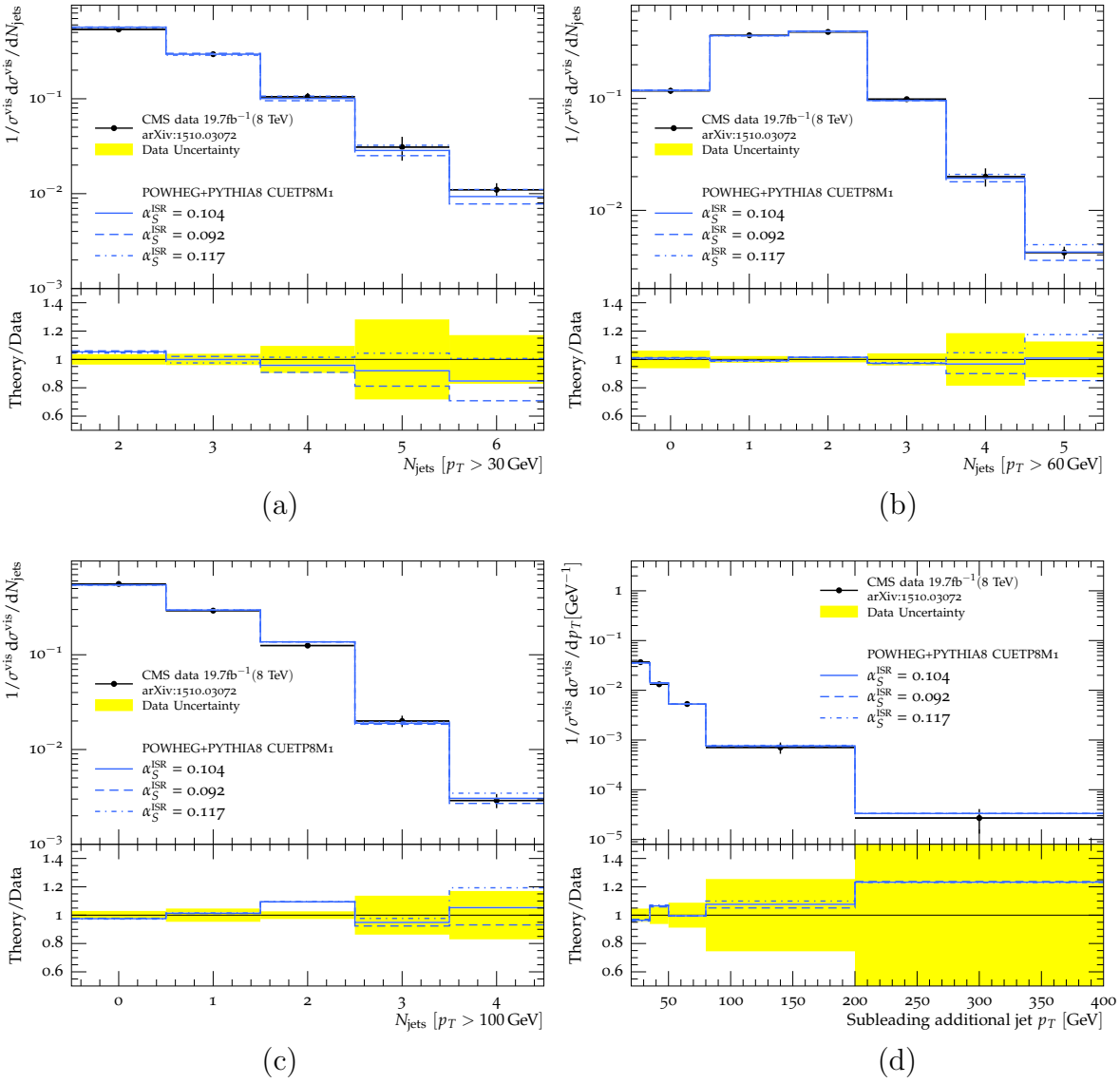

Figure 6.5: Results of $\alpha_S^{\rm ISR}$ tuning 2. Jet multiplicity distribution, $N_{\rm jets}$ (with $p_T^{jet} > 60$ GeV), after tuning $\alpha_S^{\rm ISR}$ with the $N_{\rm jets} > 3$ bins (where jets predominantly originate from the parton shower) is used as input to *Professor* [47]. The unfolded CMS data are shown with total error bars. In each plot, the calculated distribution assuming the tuned $\alpha_S^{\rm ISR}$ is shown (solid line). The calculated distributions with the lower bound (dashed line) and the upper bound (dot-dashed line) of the tuned $\alpha_S^{\rm ISR}$ are also displayed. Beneath each plot is shown the ratio of theory predictions to data. The yellow bands indicate the total data uncertainty.

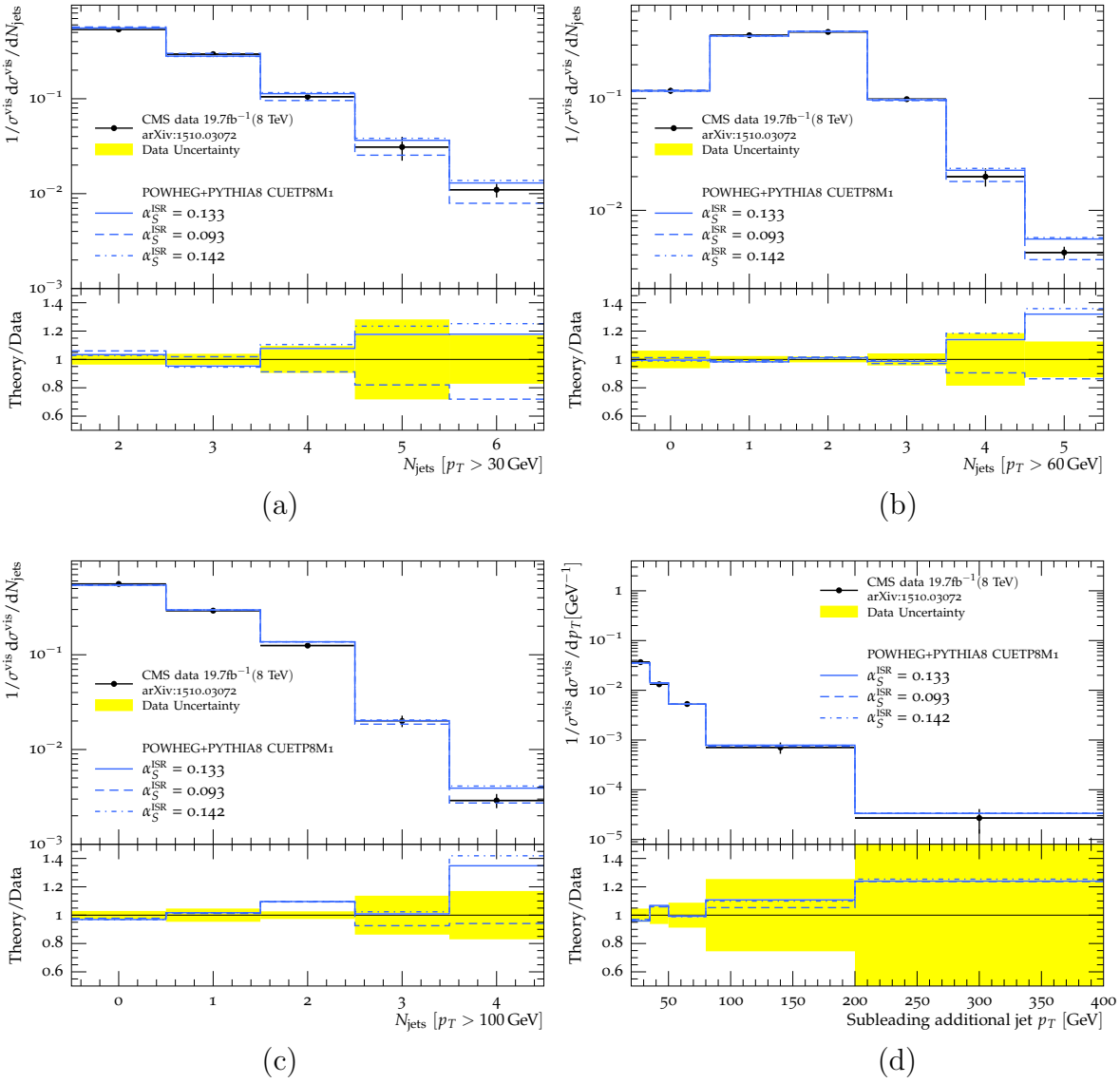

Figure 6.6: Results of α_S^{ISR} tuning 3. Jet multiplicity distribution, N_{jets} (with $p_T^{jet} > 30$ GeV) and Subleading additional jet p_T, after tuning α_S^{ISR} with the $N_{\mathrm{jets}} > 3$ bins (where jets predominantly originate from the parton shower) are used as input to *Professor* [47]. The unfolded CMS data are shown with total error bars. In each plot, the calculated distribution assuming the tuned α_S^{ISR} is shown (solid line). The calculated distributions with the lower bound (dashed line) and the upper bound (dot-dashed line) of the tuned α_S^{ISR} are also displayed. Beneath each plot is shown the ratio of theory predictions to data. The yellow bands indicate the total data uncertainty.

6.5 The renormalisation scale μ_R

From Sec. 6.4, upper and lower bound uncertainties for the optimal α_S^{ISR} were found. It is also possible however, to vary α_S^{ISR} by altering the renormalisation scale μ_R. Up to one loop correction, α_S is given by

$$\alpha_S \approx \frac{1}{\beta(n)\,\ln\left(\frac{\mu_R^2}{\Lambda_{QCD}^2}\right)} \tag{6.2}$$

$$\text{with } \beta(n) = \frac{33 - 2n}{12\pi} \tag{6.3}$$

with n being the number of active quark flavours and Λ_{QCD} the QCD-scale. Using this relation between α_S and μ_R, we can determine the scale variations corresponding to the uncertainties found for α_S^{ISR}. This is displayed in Fig. 6.7. In Eq. 6.2, Λ_{QCD} is first determined for α_S set to the central value and μ_R set to 91.2 GeV (Z boson mass). Then the upper and lower bounds for α_S are filled in and it is checked how much μ_R has to be varied for a fixed Λ_{QCD}. The variations are displayed in the legend of Fig. 6.7 and correspond to 0.33 for the upper bound and 4.10 for the lower bound.

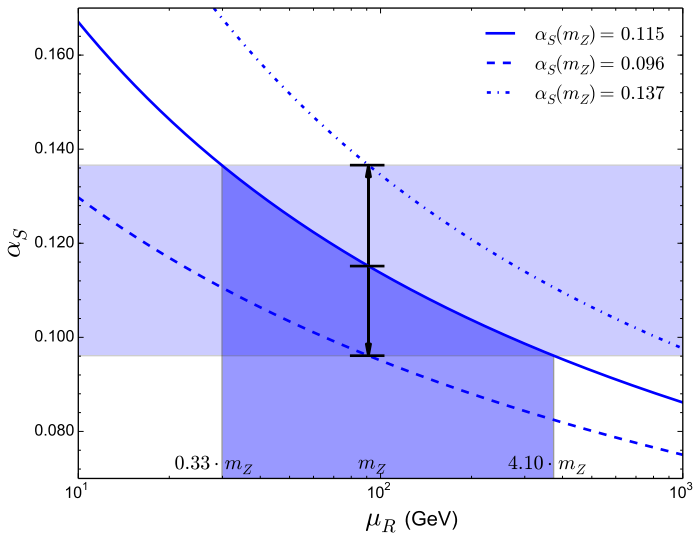

Figure 6.7: α_S as a function of the renormalization scale, μ_R. The uncertainty on the tuned α_S value (0.115) corresponds to variations of μ_R by factors of 0.33 for the upper bound and 4.10 for the lower bound.

6.6 Comparison between Professor Interpolation and MC Output

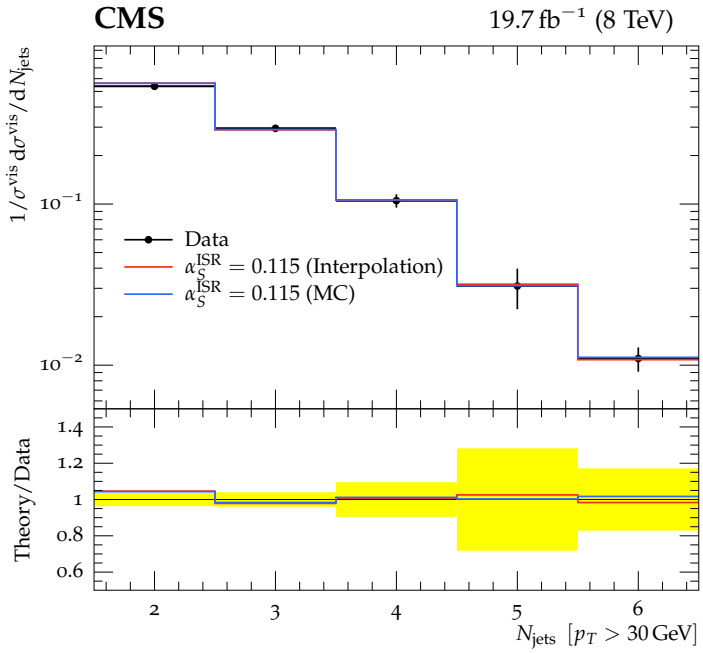

Figure 6.8: Comparison between the *Professor* interpolation and the MC output for tuning result 1 with $\alpha_S^{\mathrm{ISR}} = 0.115$ for the N_{jets} ($p_T > 30$ GeV) distribution. The interpolated results from *Professor* (red) nicely overlap with the MC data (blue) generated for the same value of α_S^{ISR}. The yellow bands denote the data uncertainties.

The *Professor* tuning result 1 is given by $\alpha_S^{\mathrm{ISR}} = 0.115$ and is used as input to a `POWHEG+PYTHIA8` MC run. The *Professor* interpolation and MC output are compared for the N_{jets} ($p_T > 30$ GeV) observable as shown in Fig. 6.8. It is to be seen that both results are nicely in agreement with each other, which provides confidence that *Professor* indeed produces correctly interpolated observable distributions.

6.7 Validation with other Top Quark Distributions

The studied tunes are validated with the TOP-15-011 distributions (with *Rivet* routine CMS_2015_I1370682) [60]. Concretely, it is checked using tune results 1, 2 and 3 (see Fig. 6.3) what the MC output with respect to data is for the observables p_T^t, $\Delta\phi^{t\bar{t}}$, $p_T^{t\bar{t}}$ and $m_{t\bar{t}}$ in the single lepton and dilepton channel.

In the single lepton and dilepton channel, we can see from Figs. 6.9 (a), (b), (c) and (d) that there is a good agreement between the different α_S^{ISR} values. However, as expected, the p_T^t remains unchanged and is still not well described by the MC[6]. Figs 6.10 (a) and (b) show how for the $p_T^{t\bar{t}}$ and $m_{t\bar{t}}$ distributions higher values of α_S^{ISR} are slightly preferred over tune 1. From Figs. 6.10 (c) and (d), the variations in α_S^{ISR} in the $p_T^{t\bar{t}}$ and $m_{t\bar{t}}$ distributions do not seem to have a significant effect on the MC output.

[6]The incorrect description of top p_T is known to be caused by missing higher order effects.

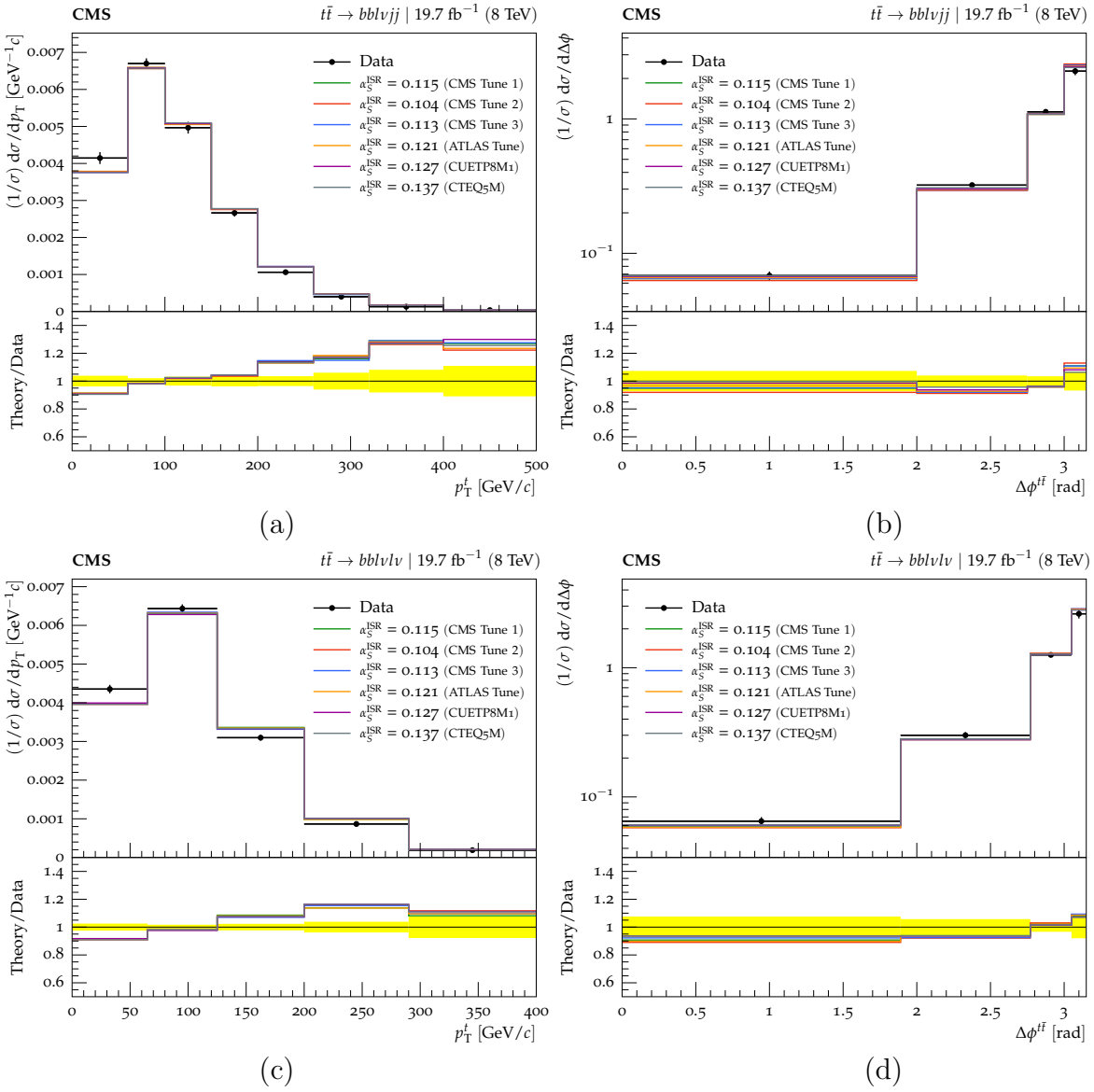

Figure 6.9: Validation of the TOP-15-011 distributions for the variables p_T^t and $\Delta\phi^{t\bar{t}}$ in the single lepton ((a) and (b)) and the dilepton ((c) and (d)) channels for the four different tune results. The ATLAS ATTBAR-POWHEG tune and the `PYTHIA8` (CTEQ5M) and `PYTHIA6` (CUETP8M1) defaults are also displayed.

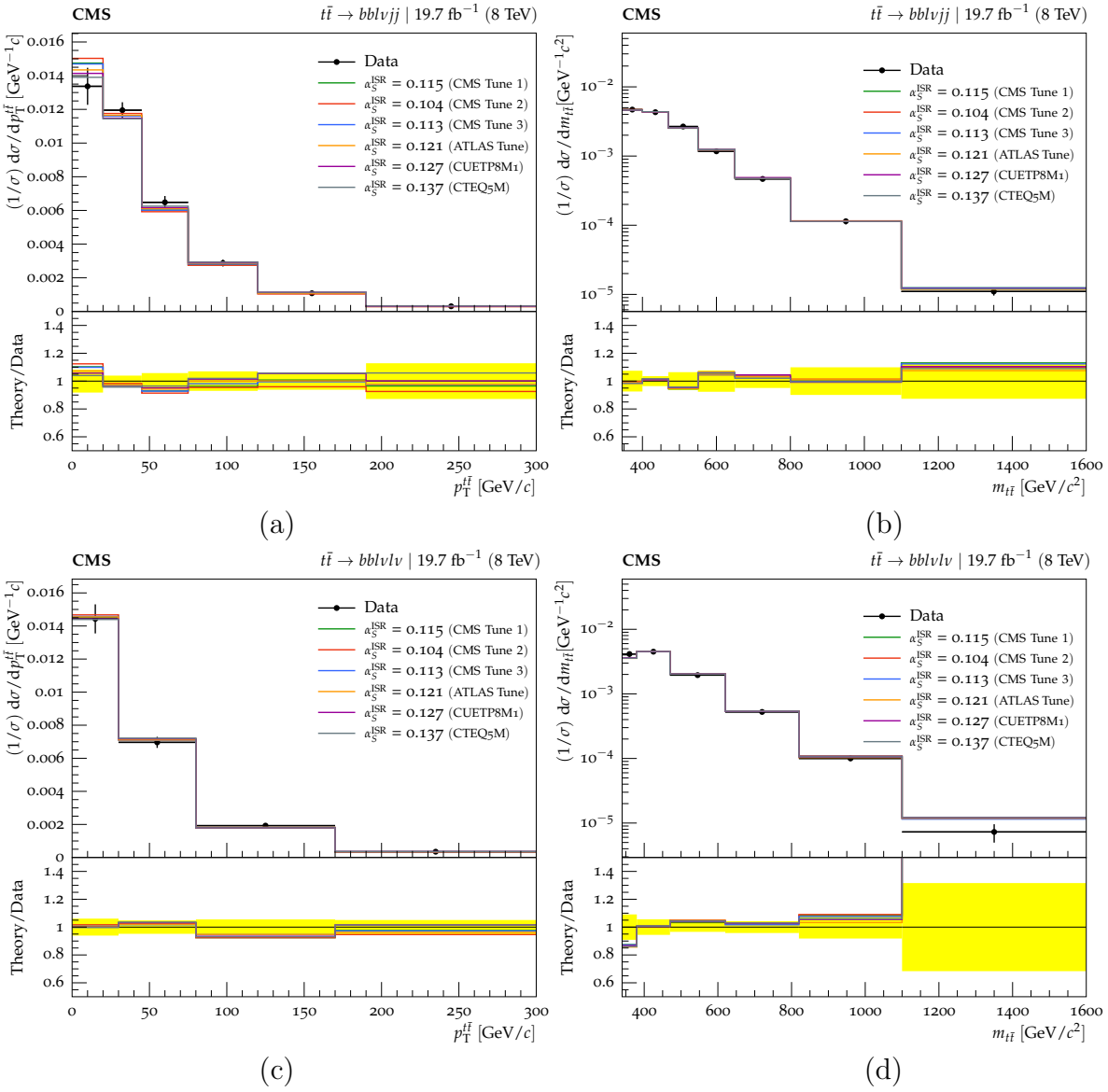

Figure 6.10: Validation of the TOP-15-011 distributions for the variables $p_T^{t\bar{t}}$ and $m_{t\bar{t}}$ in the single lepton ((a) and (b)) and the dilepton ((c) and (d)) channels for the four different tune results. The ATLAS ATTBAR-POWHEG tune and the `PYTHIA8` (CTEQ5M) and `PYTHIA6` (CUETP8M1) defaults are also displayed.

6.8 Summary and Discussion

In this study, the PYTHIA8 parameter α_S^{ISR} is tuned using N_{jets}-distributions. The optimal value is chosen to be $\alpha_S^{\mathrm{ISR}} = 0.115^{+0.021}_{-0.019}$ as its correspondence with data is the best as can be seen from Figs. 6.4 (a), (b), (c) and (d) and it has the lowest uncertainties. Furthermore, within uncertainties it is in agreement with the ATLAS ATTBAR-POWHEG tune (Fig. 6.3 and ref. [59]). The uncertainties seem to correspond to a factor 0.33 and 4.10 for the respective upper and lower bounds of the renormalisation scale μ_R. The different tunes give α_S^{ISR} of the order 0.10-0.11, however when applying these to TOP-15-011 distributions (Figs 6.9 and 6.10), the value of $\alpha_S^{\mathrm{ISR}} = 0.1273$ seems to give a slightly better description. For further tests, the $t\bar{t}$ samples for ICHEP 2016 have been submitted with $\alpha_S^{\mathrm{ISR}} = 0.1273$, with the same value as the PYTHIA6 default (CTEQ5) used in Run I CMS simulations.

CUETP8M1 predictions using underlying event Drell-Yan p_T and rapidity y, are tested with the tuned α_S^{ISR} values. No significant changes have been observed [61]. The main differences have been observed in underlying event observables up to ∼10-15% [61]. This shows that it is desirable to have a new underlying event tune that has a lower α_S^{ISR} value.

Tuning α_S^{ISR} in POWHEG+PYTHIA8 is the most straightforward approach to fix the discrepancies seen in the N_{jets} distributions (e.g. Fig. 6.1). This process however may not be as simple in MADGRAPH5_aMC@NLO+PYTHIA8 since for this case the α_S^{ISR} must be modified in the matrix element as well. The tune found makes the agreement of 13 TeV data with POWHEG+PYTHIA8 as good as 8 TeV with MADGRAPH5+PYTHIA6, i.e. a very good description of all distributions (in the considered low p_T and mass ranges) except for p_T^t, which is due to missing higher order effects. Note also that parton shower α_S^{ISR} tuning should depend on the QCD scale choice and on the hdamp parameter in POWHEG (which is taken to be hdamp $= m_t$). In a finer tuning attempt hdamp and α_S^{ISR} should be tuned simultaneously or consecutively. For instance, one can first tune α_S^{ISR} as has been done in this study and then tune the hdamp variable using the first additional jet p_T distribution as input.

To conclude with, the description of N_{jets} is fixed using a lower α_S^{ISR} value than the PYTHIA8 default of 0.1365. This change does not cause significant alterations and therefore with the lower α_S^{ISR} value all top quark distributions except p_T^t are described well by POWHEG+PYTHIA8. These results are also made public as additional material to [58].

Hoofdstuk 7

Nederlandstalige Samenvatting

7.1 Introductie

Het Standaardmodel (SM) van de elementaire deeltjesfysica is een zeer succesvolle theorie die in staat is om een erg rijk gamma aan experimenten te beschrijven. Het beschrijft de drie fundamentele krachten van het elektromagnetisme, de zwakke kernkracht en de sterke kernkracht, zoals beschreven in Sectie 1.2. De vierde fundamentele kracht, nl. de zwaartekracht, past niet binnen dit framework, vermits het SM niet compatibel is met de algemene relativiteitstheorie. Daarnaast levert het een classificatie van alle fundamentele deeltjes die tot op heden gekend en waargenomen zijn. Deze worden beschreven in Sectie 1.1.

Het waarnemen van deze fundamentele deeltjes gebeurt d.m.v. een groot aantal experimenten verspreid over de ganse wereld. In deze studie wordt toegespitst op het CMS (*Compact Muon Solenoid*) experiment (hoofdstuk 3), uitgevoerd in CERN in Genève, Zwitserland. CMS is een detector die geïnstalleerd is op de LHC (*Large Hadron Collider*), waarmee protonen versneld worden tot enorme snelheden en botsen op welbepaalde interactiepunten aan hoge massacentrumenergieën. CMS is cilindrisch van vorm en bevindt zich rond een dergelijk interactiepunt waar het tracht de vervalproducten van de botsingen te detecteren.

Hoewel het SM erg succesvol is, bestaan er toch vele tekortkomingen en fenomenen die niet verklaard kunnen worden zonder een uitbreiding van de theorie. Enkele van deze tekortkomingen worden gegeven in Sectie 1.4. Een erg populaire theorie die het SM uitbreidt is Supersymmetrie (SUSY), zoals uiteengezet in hoofdstuk 2. SUSY postuleert het bestaan van een superpartner voor alle reeds gekende fundamentele deeltjes.

Hier wordt het Minimale Supersymmetrische Model (MSSM) aangenomen. Dit betreft een minimale uitbreiding van het SM en veronderstelt het behoud van R-pariteit. Deze symmetrie zorgt ervoor dat supersymmetrische deeltjes steeds in paren geproduceerd worden en dat er een lichtst supersymmetrisch deeltje (LSP) bestaat, het neutralino χ_1^0, dat bovendien stabiel is. Bovenstaande inzichten worden in Sectie 2.3 in meer detail uiteengezet. Een SUSY-onderzoek dat in deze thesis gedaan wordt, staat hieronder in Sectie 7.2 beschreven.

Naast de uitbreiding van het SM d.m.v. SUSY, is het in deze thesis ook belangrijk om stil te staan bij Monte Caro (MC) generatoren. Deze zijn onmisbaar bij hoge energie fysica experimenten. MC generatoren bestaan uit een set van modellen die instaan voor het simuleren van evenementen zoals deze die optreden bij botsingen tussen hadronen (of hier, botsingen tussen protonen). Wij spitsen ons toe op twee aparte types van MC generatoren. Ter illustratie bekijken wij `POWHEG` en `PYTHIA`.

`POWHEG` is een Matrix Element (ME) MC generator. Dit betekent dat deze instaat voor het genereren van het initiële *hard scatter* proces waarbij een hoge momentumoverdracht plaatsvindt. Dit is m.a.w. de interactie tussen twee partonen uit elk van beide protonen. Powheg berekent dit proces tot op *Next-to-Leading-Order* (NLO), waarbij het dus een harde partonenemissie in rekening neemt, hetgeen weergegeven wordt in het Feynman diagram in Fig. 4.2.

`PYTHIA` is een MC generator die hoge energie fysica evenementen genereert. Dit zijn sets van deeltjes die geproduceerd werden uit de interactie tussen twee inkomende deeltjes. Het bevat theoretische modellen die de evolutie van een proces met hoge momentumoverdracht simuleren tot een complexe multi-hadronische finale toestand. Deze evolutie wordt *Parton Shower* (PS) genoemd. Een parton verliest immers steeds momentum tijdens diens propagatie doorheen de ruimte (d.m.v. de interacties met quarks en gluonen). Eens een bepaalde drempelwaarde overschreden wordt, treedt hadronisatie op waarbij kleurloze finale toestanden gevormd worden.

Aangezien MC generatoren tal van benaderingen gebruiken, worden parameters scherpgesteld om er voor te zorgen dat de predicties overeenkomen met wat gemeten wordt in data. Dit proces heet *tuning* en wordt gedaan met specifieke programma's. Hiertoe kan *Professor* gebruikt worden, een tuning code die in meer detail beschreven staat in Appendix A. Een concrete toepassing van het scherpstellen van een `PYTHIA8` parameter, nl. α_S^{ISR}, wordt uiteengezet in Sectie 7.3, verder in deze tekst.

7.2 Deel I: Zoeken naar scalaire top quark partners

Deel I van deze studie is een deelonderzoek in een SUSY-analyse m.b.t. het zoeken naar de scalaire superpartner van de top quark bij een massacentrumenergie $\sqrt{s} = 13$ TeV voor proton-proton botsingen. Het gepostuleerde proces wordt gegeven in Figuur 5.1, waarbij specifiek wordt gezocht naar het kanaal waarin beide W bosonen leptonisch vervallen.

Het is de bedoeling bij dergelijke studies dat een signaalregio geconstrueerd wordt. Dit is een bepaald stuk van de faseruimte waar het signaal de achtergrondprocessen gegeven op blz. 56 domineert. De discriminerende parameter die hiervoor gebruikt wordt is $M_{T2}(ll)$ (gedefinieerd door Vgl. 5.1). Het is uiteraard belangrijk dat in de signaalregio de achtergronden, die berekend zijn door Monte Carlo generatoren, correct opgenomen zijn. Zoals aangegeven in Tabel 5.1 en Figuur 5.4, wordt opgemerkt dat de $t\bar{t}$ + jets achtergrond toch voor hoge waarden van $M_{T2}(ll)$ (> 140 GeV/c^2) aanwezig is. Voor een dergelijk SM proces is dit onmogelijk. Een verklaring en oplossing voor het optreden van $t\bar{t}$ + jets evenementen in dit gebied wordt vervolgens uit de doeken gedaan.

In de regio $M_{T2}(ll) > 140$ GeV/c^2 worden de aanwezige $t\bar{t}$ + jets evenementen specifiek uitgezocht. De gereconstrueerde kinematische informatie (RECO) wordt gelinkt aan de gegenereerde kinematische informatie (GEN) om te achterhalen wat de moederdeeltjes zijn van de geselecteerde leptonen. Een voorbeeld hiervan wordt gegeven in Sectie 5.4. Van de 37 gevonden evenementen blijken er 29 afkomstig van b quark verval en niet van leptonisch W boson verval. Dit betekent dat een deel van de $t\bar{t}$ + jets evenementen verkeerdelijk geselecteerd worden in de analyse.

Voor dit probleem worden twee oplossingen vooropgesteld. Ten eerste wordt gekeken of een `RelIso04` < 0.12 cut het probleem zou oplossen. De motivatie voor deze keuze is om de grootte van de fictieve kegel getekend rondom het geselecteerde lepton te vergroten om zo meer jet activiteit op te vangen en zo leptonen van b quark verval (dicht bij jet activiteit) te verwijderen. Dit kan eenvoudig begrepen worden uit Vgl. 5.3 en Figuur 5.5. Het effect hiervan was dat deze methode wel degelijk $\sim$80% van de verkeerdelijk geselecteerde $t\bar{t}$ + jets evenementen reduceert, maar dit echter ook inefficiënt is voor het signaal. De methode bestaat er in om een `MultiIsoV2` cut toe te passen, zoals gedefinieerd in Vgl. 5.4. Deze heeft het gewenste effect om wederom $\sim$80% van de verkeerdelijk geselecteerde leptonen uit de hoge $M_{T2}(ll)$ regio te verwijderen. Dit is

weergegeven in de Figuren 5.6b en 5.7. Daarnaast is het toepassen van deze cut zeer signaalefficiënt, vermits deze slechts een verlies van 4% oplevert.

7.3 Deel II: Scherpstellen van α_S^{ISR} in POWHEG+ PYTHIA8 voor het modelleren van top quark paren

Deel II van deze studie situeert zich rond het zoeken naar oplossingen voor een gekend probleem bij het genereren van $t\bar{t}$ evenementen m.b.v. de MC generatoren `POWHEG+ PYTHIA8`. In Fig. 6.1 wordt aangetoond hoe het resultaat van de simulatie in functie van jet-multipliciteit N_{jets} duidelijk afwijkt van wat gemeten wordt in data. Een oplossing wordt hiertoe voorgesteld waarbij een specifieke parameter in `PYTHIA8`, nl. `SpaceShower: alphaSvalue`, wordt scherpgesteld. Deze wordt in het vervolg van de tekst aangeduid met α_S^{ISR}. Het scherpstellen gebeurt d.m.v. *Professor*, een programma daartoe speciaal ontworpen. Het scherpstellen wordt in het vervolg *tuning* genoemd.

Er worden 13 MC runs gegenereerd voor verschillende waarden van α_S^{ISR} zoals gegeven in Tabel 6.1. Voor deze runs worden drie tunings uitgevoerd naar een bepaalde observabele (of observabelen) zoals aangeduid in Tabel 6.2. Dit gebeurt aan de hand van een χ^2 methode die in meer detail in Appendix A wordt toegelicht. Elk tuning-resultaat staat samengevat in Tabel 6.3 met bijhorende onzekerheden.

Het effect van elke tuning poging op de verschillende observabelen wordt weergegeven in Figuren 6.4, 6.5 en 6.6. Zij worden bovendien vergeleken met de ATLAS ATTBAR-POWHEG tune [59], de `PYTHIA8` (CUETP8M1) en `PYTHIA6` (CTEQ5M) standaarden in Fig 6.3. Hieruit wordt besloten dat tune 1 de meest optimale is vermits deze met het ATLAS-resultaat en de `PYTHIA6` en `PYTHIA8` standaarden in overeenkomst is, de kleinste onzekerheden heeft en de distributies in Fig. 6.4 accuraat beschrijft.

Voor de optimale tune 1 wordt voor diens onzekerheden nagegaan met welke onzekerheden in de renormalisatieschaal deze corresponderen. Dit wordt grafisch weergegeven in Fig. 6.7. De onzekerheden corresponderen met een variatie van de renormalisatieparameter volgens de factoren 0.33 en 4.10.

Toepassing van de gevonden tunes op TOP-15-011 distributies [60] is weergegeven in Figuren 6.9 en 6.10. Hier worden de MC runs voor de verschillende tunes in functie

van de observabelen p_T^t, $\Delta\phi^{t\bar{t}}$, $p_T^{t\bar{t}}$ en $m_{t\bar{t}}$ uitgezet. Ten eerste valt hierbij op dat p_T^t uitermate slecht beschreven wordt. Dit is te wijten aan hogere orde effecten die niet in rekening gebracht zijn en niet opgelost kunnen worden door tuning. Ten tweede valt op dat de MC uitkomsten voor alle tunes voor de overige distributies erg gelijkaardig zijn met elkaar. Op het zicht leren we hier dat de beste overeenkomsten toch bij de hogere waardan van α_S^{ISR} te vinden zijn. Daarom werden de $t\bar{t}$ samples voor ICHEP 2016 aangevraagd met de waarde van $\alpha_S^{\mathrm{ISR}} = 0.1273$, hetgeen dezelfde waarde is van de `PYTHIA6` standaard en dus iets hoger ligt dan de eigen gevonden tunes van orde 0.10-0.11.

Voor een toekomstige poging tot tuning, kan men proberen om α_S^{ISR} gelijktijdig of opeenvolgend te tunen met de `hdamp` parameter in `POWHEG` daar dit gunstige resultaten levert volgens een studie gedaan door de ATLAS collaboratie [59].

Men kan concluderen dat in deze studie de beschrijving van de N_{jets} observable hersteld is door het gebruiken van een lagere α_S^{ISR} waarde dan de standaardwaarde van 0.1365 voor `PYTHIA8`. Deze aanpassing veroorzaakt geen significante veranderingen voor de overige top quark distributies (p_T^t, $\Delta\phi^{t\bar{t}}$, $p_T^{t\bar{t}}$ en $m_{t\bar{t}}$) daar deze nog steeds accuraat beschreven worden door `POWHEG+PYTHIA8` behalve p_T^t. Deze resultaten zijn ook publiek gemaakt als extra materiaal voor [58].

Appendix A

Professor: A tuning tool for Monte Carlo event generators

Professor (PROcedure For EStimating Systematic errORs) is a parametrisation-based tuning tool. This means that the approach taken is to parametrise the generator behaviour by fitting a polynomial to the generator response (here referred to as MC_b) for each observable bin to changes in the P-element parameter vector $\boldsymbol{p} = (p_1, ..., p_P)$. P denotes the amount of parameters that can be changed in the event-generator.

One uses a polynomial of second order to do the bin parametrisation. Say that $\boldsymbol{p}_0$ is a randomly chosen point in parameter space (in between the bounds of a hypercube determined by the user), then the polynomial has the following form:

$$MC_b(\boldsymbol{p}) \approx \alpha_0^{(b)} + \sum_i^P \beta_i^{(b)} p_i' + \sum_{i \leq j}^P \gamma_{ij}^{(b)} p_i' p_j' \tag{A.1}$$

with $\boldsymbol{p}' = \boldsymbol{p}$ - $\boldsymbol{p}_0$. The left side of the above equations denotes the output from the event-generator at parameter point $\boldsymbol{p}$, whereas the right side contains the unknown coefficients $[\alpha, \beta, \gamma]$. The amount of coefficients to be determined depends on the order of the polynomial (here: 2) and the amount of parameters P to be tuned, also referred to as the dimension of the parameter space. For a 2^{nd} order fit, it can be readily computed from Eq. A.1:

$$N_2^{(P)} = 1 + P + P(P+1)/2 \tag{A.2}$$

Once we have a set of functions MC_b, we have a very fast way of predicting the gen-

erator behaviour at a certain point in parameter space $\boldsymbol{p}$, as it is not necessary to run the generator again. This allows one to construct a goodness of fit function which compares the data to the Monte Carlo, and thus to come up with an optimal point $\boldsymbol{p}_{\text{best}}$ of the tuned parameters, even though $\boldsymbol{p}_{\text{best}}$ was not specifically used in the computation.

A.1 Determining the response function $\mathrm{MC}_b(\mathrm{p})$

Given sets of sampled points $\{\boldsymbol{p}\}$ and generator values $\{MC_b(\boldsymbol{p})\}$, eq. A.1 can be transformed into a matrix equation, which is acquired for every bin and for every observable:

$$\mathbf{v}^{(b)} = \widetilde{\mathbf{P}}\mathbf{c}^{(b)} \tag{A.3}$$

$\widetilde{\mathbf{P}}$ contains the variations of the parameter points ($\boldsymbol{p}$ - $\boldsymbol{p}_0$) for different orders. We get in matrix notation, if we presume 2 parameters such that $\boldsymbol{p} = (p_x, p_y)$ and N evaluated parameter points for a certain bin b, that:

$$\underbrace{\begin{pmatrix} v_1 \\ v_2 \\ \vdots \\ v_N \end{pmatrix}}_{\mathbf{v}\text{ (values)}} = \underbrace{\begin{pmatrix} 1 & x_1 & y_1 & x_1^2 & x_1y_1 & y_1^2 \\ 1 & x_2 & y_2 & x_2^2 & x_2y_2 & y_2^2 \\ & & & \vdots & & \\ 1 & x_N & y_N & x_N^2 & x_Ny_N & y_N^2 \end{pmatrix}}_{\widetilde{\mathbf{P}}\text{(sampled parameter sets)}} \cdot \underbrace{\begin{pmatrix} \alpha_0 \\ \beta_x \\ \beta_y \\ \gamma_{xx} \\ \gamma_{xy} \\ \gamma_{yy} \end{pmatrix}}_{\mathbf{c}\text{ (coefficients)}} \tag{A.4}$$

with the values v_i being the generator computed value. This can be understood if we simply look at the equation we get for the first row. With x denoting the first parameter and y denoting the second parameter, we get:

$$v_1 = \alpha_0 + x_1\beta_x + y_1\beta_y + x_1^2\gamma_{xx} + x_1y_1\gamma_{xy} + y_1^2\gamma_{yy} \tag{A.5}$$

with $x_1 = p'_x = p_x - p_{x0}$ and $y_1 = p'_y = p_y - p_{y0}$ both evaluated at point n°1 in parameter space. This is exactly eq. A.1.

With the matrices $\mathbf{v}^{(b)}$ and $\widetilde{\mathbf{P}}$ known, we still need to compute $\mathbf{c}^{(b)}$. This can be done by a so-called pseudo-inversion $\widetilde{\mathcal{I}}$ of $\widetilde{\mathbf{P}}$:

$$\mathbf{c}^{(b)} = \widetilde{\mathcal{I}}[\widetilde{\mathbf{P}}]\mathbf{v}^{(b)} \tag{A.6}$$

Pseudo-inversion is comparable to regular $(n \times n)$-matrix inversion, but here for $(m \times n)$-matrices.

A.2 Goodness of Fit (GoF)

In the previous section, the functions $\mathrm{MC}_b(\boldsymbol{p})$ were determined, giving us the generator response for every point in parameter space for every observable bin. What remains now, is to compute a goodness of fit function that is minimised for a certain parameter point $\boldsymbol{p}_{\mathrm{best}}$, which can be found from extrapolating the GoF function to a minimum. It is possible to add per-observable weights $\mathrm{w}_{\mathcal{O}}$ for each observable $\mathcal{O}$. We choose a χ^2-function defined according to:

$$\chi^2(\boldsymbol{p}) = \sum_{\mathcal{O}} w_{\mathcal{O}} \sum_{b \,\in\, \mathcal{O}} \frac{\left(\mathrm{MC}_b(\boldsymbol{p}) - \mathcal{R}_b\right)^2}{\Delta_b^2} \tag{A.7}$$

where $\mathcal{R}_b$ is the data value for bin b, and the error Δ_b is calculated from the sum in quadrature of the MC-error and the error in the data. It should be noted that determination of the weights is a subjective process and should be chosen according to criteria set by the user.

A.3 Error Estimation: Construction of Eigentunes

Once an optimal set of parameters $\boldsymbol{p}_{\mathrm{best}}$ is found, it remains to find the correct errors on the acquired tunes. The upper and lower bounds we refer to as the **eigentunes**. For simplicity we now consider a two dimensional parameter space $\boldsymbol{p} = (p_x,p_y)$, with optimal tune values (p_x^*,p_y^*). The eigentunes can be constructed by considering a Taylor's expansion around the $\chi^2(\boldsymbol{p})$.

$$\begin{aligned}\chi^2(p_x, p_y) \approx \chi^2(p_x^*, p_y^*) + \frac{1}{2}(p_x - p_x^*)^2 \frac{\partial^2\chi^2}{\partial p_x^2}\bigg|_{(p_x^*,p_y^*)} + \frac{1}{2}(p_y - p_y^*)^2 \frac{\partial^2\chi^2}{\partial p_y^2}\bigg|_{(p_x^*,p_y^*)} \\ + (p_x - p_x^*)(p_y - p_y^*)\frac{\partial^2\chi^2}{\partial p_x \partial p_y}\bigg|_{(p_x^*,p_y^*)}\end{aligned} \tag{A.8}$$

If we compare this formula to the general equation of a rotated ellipse centred about (*a*,*b*)

$$1 = \frac{(x-a)^2}{A^2} + \frac{(y-b)^2}{B^2} + \frac{xy}{C^2}, \tag{A.9}$$

with A and B the lengths of the axes and $\frac{1}{B^4} - 4\frac{1}{A^2}\frac{1}{C^2} < 0$[1], we learn that for a specific value of $\Delta\chi^2 = \chi^2(p_x, p_y)$ - $\chi^2(p_x^*, p_y^*)$ an ellipse in parameter space can be drawn. The standard *Professor* prescription is to choose $\Delta\chi^2 = \chi^2(p_x^*, p_y^*)$. This means the minimum of the χ^2 is shifted up by the value of $\chi^2(p_x^*, p_y^*)$. The outer edges of the ellipse are then taken to be the errors on the tunes as depicted in Fig. A.1

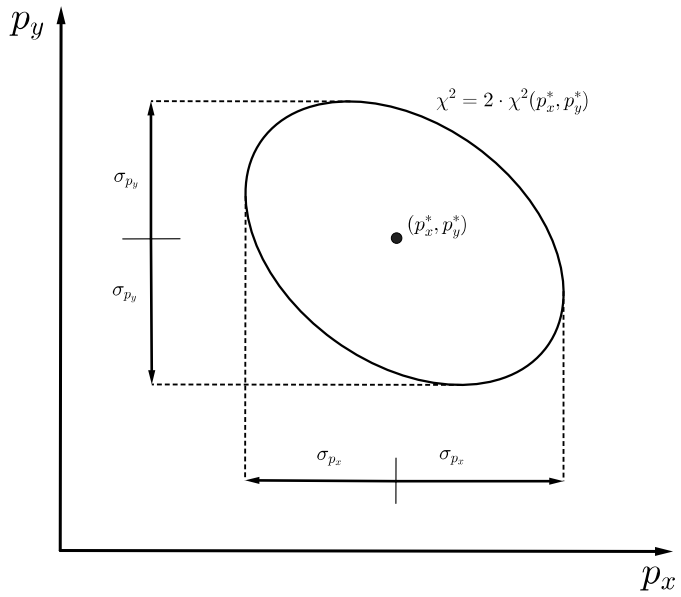

Figure A.1: Ellipse denoting equal values of the χ^2 in parameter space.

The ellipse of equal χ^2 is rotated because of the fact that the parameters p_x and p_y are correlated. This follows from Eq. A.7 in which it is clear that the term containing $\frac{\partial^2\chi^2}{\partial p_x \partial p_y}\Big|_{(p_x^*, p_y^*)}$ becomes zero if a variation of the χ^2 in p_1 does not depend on a variation in p_2 (or vice versa) and would then mean that the ellipse has principal axes parallel to the x- and y-axis.

[1]Write the ellipse equation like $\frac{1}{y^2} = \alpha t^2 + \beta t + \gamma$ with $t = \frac{x}{y}$, and realise that $\alpha t^2 + \beta t + \gamma$ can never be equal to 0, because $\frac{1}{y^2}$ is always positive. This requires a negative discriminant $D = \beta^2 - 4\alpha\gamma$.

Bibliography

[1] B. Povh. *Particles and nuclei an introduction to the physical concepts*. Springer, Berlin, 2008.

[2] Herbert Goldstein. *Classical mechanics*. Addison Wesley, San Francisco, 2002.

[3] Particle Data Group. *PHYSICAL CONSTANTS*, 2016 (accessed May 13, 2016). `http://pdg.lbl.gov/2011/reviews/rpp2011-rev-phys-constants.pdf`.

[4] M. Goldhaber, L. Grodzins, and A. W. Sunyar. Helicity of neutrinos. *Phys. Rev.*, 109:1015–1017, Feb 1958.

[5] C. L. Cowan, F. Reines, F. B. Harrison, H. W. Kruse, and A. D. McGuire. Detection of the free neutrino: a confirmation. *Science*, 124(3212):103–104, 1956.

[6] John N. Bahcall, Aldo M. Serenelli, and Sarbani Basu. New solar opacities, abundances, helioseismology, and neutrino fluxes. *Astrophys. J.*, 621:L85–L88, 2005.

[7] Jamin M. Laach M. *QCD and Renormalization Group Methods*, 2006. `http://www.desy.de/~martillu/rgm06-1.pdf`.

[8] J. et al. Beringer. Review of particle physics. *Phys. Rev. D*, 86:010001, Jul 2012.

[9] K. A. Olive et al. Quantum Chromodynamics (rev.). *Chin. Phys.*, C38:090001, 2014.

[10] John C. Collins, Davison E. Soper, and George F. Sterman. Factorization of Hard Processes in QCD. *Adv. Ser. Direct. High Energy Phys.*, 5:1–91, 1989.

[11] Guido Altarelli and G. Parisi. Asymptotic Freedom in Parton Language. *Nucl. Phys.*, B126:298–318, 1977.

[12] Michał Czakon, Paul Fiedler, and Alexander Mitov. Total Top-Quark Pair-Production Cross Section at Hadron Colliders Through $O(\frac{4}{S})$. *Phys. Rev. Lett.*, 110:252004, 2013.

[13] Richard D. Ball et al. Parton distributions with LHC data. *Nucl. Phys.*, B867:244–289, 2013.

[14] Hung-Liang Lai, Marco Guzzi, Joey Huston, Zhao Li, Pavel M. Nadolsky, Jon Pumplin, and C. P. Yuan. New parton distributions for collider physics. *Phys. Rev.*, D82:074024, 2010.

[15] C. S. Wu, E. Ambler, R. W. Hayward, D. D. Hoppes, and R. P. Hudson. Experimental test of parity conservation in beta decay. *Phys. Rev.*, 105:1413–1415, Feb 1957.

[16] R. P. Feynman and M. Gell-Mann. Theory of the fermi interaction. *Phys. Rev.*, 109:193–198, Jan 1958.

[17] F. Englert and R. Brout. Broken symmetry and the mass of gauge vector mesons. *Phys. Rev. Lett.*, 13:321–323, Aug 1964.

[18] Mark Thomson. *Modern particle physics*. Cambridge University Press, Cambridge, United Kingdom New York, 2013.

[19] Y. et al. Fukuda. Evidence for oscillation of atmospheric neutrinos. *Phys. Rev. Lett.*, 81:1562–1567, Aug 1998.

[20] Q. R. et al. Ahmad. Measurement of the rate of $\nu_e + d \rightarrow p + p + e^-$ interactions produced by ^8b solar neutrinos at the sudbury neutrino observatory. *Phys. Rev. Lett.*, 87:071301, Jul 2001.

[21] CMS Collaboration. Observation of a new boson at a mass of 125 GeV with the CMS experiment at the LHC. *Phys. Lett.*, B716:30–61, 2012.

[22] ATLAS Collaboration. Observation of a new particle in the search for the Standard Model Higgs boson with the ATLAS detector at the LHC. *Phys. Lett.*, B716:1–29, 2012.

[23] Satoshi Iso. What Can We Learn from the 126 GeV Higgs Boson for the Planck Scale Physics? - Hierarchy Problem and the Stability of the Vacuum -. In *Proceedings, KMI-GCOE Workshop on Strong Coupling Gauge Theories in the LHC Perspective (SCGT 12)*, pages 238–246, 2014.

[24] C. L. et al. Bennett. Nine-year Wilkinson Microwave Anisotropy Probe (WMAP) Observations: Final Maps and Results. 208:20, October 2013.

[25] David M. Jacobs, Glenn D. Starkman, and Bryan W. Lynn. Macro Dark Matter. *Mon. Not. Roy. Astron. Soc.*, 450(4):3418–3430, 2015.

[26] Stephen P. Martin. A Supersymmetry primer. 1997. [Adv. Ser. Direct. High Energy Phys.18,1(1998)].

[27] Cheng. *Gauge theory of elementary particle physics*. Clarendon Press Oxford University Press, Oxford Oxfordshire New York, 1984.

[28] Markus A. Luty. 2004 TASI lectures on supersymmetry breaking. In *Physics in $D \geq 4$. Proceedings, Theoretical Advanced Study Institute in elementary particle physics, TASI 2004, Boulder, USA, June 6-July 2, 2004*, pages 495–582, 2005.

[29] Herbert K. Dreiner. An Introduction to explicit R-parity violation. 1997. [Adv. Ser. Direct. High Energy Phys.21,565(2010)].

[30] Rabindra N. Mohapatra. Supersymmetry and R-parity: an Overview. *Phys. Scripta*, 90:088004, 2015.

[31] Tanju Gleisberg, Stefan Hoeche, Frank Krauss, Andreas Schalicke, Steffen Schumann, and Jan-Christopher Winter. SHERPA 1. alpha: A Proof of concept version. *JHEP*, 02:056, 2004.

[32] Amos Breskin and Rüdiger Voss. *The CERN Large Hadron Collider: Accelerator and Experiments*. CERN, Geneva, 2009.

[33] Thomas Ferbel. *Experimental techniques in high-energy nuclear and particle physics*. World Scientific, Singapore River Edge, NJ, 1991.

[34] CMS Collaboration. *CMS TriDAS project: Technical Design Report, Volume 1: The Trigger Systems*. Technical Design Report CMS.

[35] Sergio Cittolin, Attila Rácz, and Paris Sphicas. *CMS The TriDAS Project: Technical Design Report, Volume 2: Data Acquisition and High-Level Trigger. CMS trigger and data-acquisition project*. Technical Design Report CMS. CERN, Geneva, 2002.

[36] CMS Collaboration. The CMS high level trigger. *Eur. Phys. J.*, C46:605–667, 2006.

[37] Xuan Chen. *CMSSW Application Framework*, 2016 (accessed March 3, 2016). https://twiki.cern.ch/twiki/bin/view/CMSPublic/WorkBookCMSSWFramework.

[38] Brun R. and Rademakers F. *ROOT: Data Analysis Framework*. CERN.

[39] S. et al. Agostinelli. GEANT4: a simulation toolkit. *Nuclear Instruments and Methods in Physics Research A*, 506:250–303, July 2003.

[40] CMS Collaboration. Particle-Flow Event Reconstruction in CMS and Performance for Jets, Taus, and MET. Technical Report CMS-PAS-PFT-09-001, CERN, 2009. Geneva, Apr 2009.

[41] CMS Collaboration. Commissioning of the Particle-flow Event Reconstruction with the first LHC collisions recorded in the CMS detector. Technical Report CMS-PAS-PFT-10-001, 2010.

[42] Carlo Oleari. The POWHEG-BOX. *Nucl. Phys. Proc. Suppl.*, 205-206:36–41, 2010.

[43] Paolo Nason. A New method for combining NLO QCD with shower Monte Carlo algorithms. *JHEP*, 11:040, 2004.

[44] The powheg box, available processes. http://powhegbox.mib.infn.it/. (accessed April 20, 2016).

[45] Torbjörn Sjöstrand, Stefan Ask, Jesper R. Christiansen, Richard Corke, Nishita Desai, Philip Ilten, Stephen Mrenna, Stefan Prestel, Christine O. Rasmussen, and Peter Z. Skands. An Introduction to PYTHIA 8.2. *Comput. Phys. Commun.*, 191:159–177, 2015.

[46] Johan Alwall et al. Comparative study of various algorithms for the merging of parton showers and matrix elements in hadronic collisions. *Eur. Phys. J.*, C53:473–500, 2008.

[47] Andy Buckley, Hendrik Hoeth, Heiko Lacker, Holger Schulz, and Jan Eike von Seggern. Systematic event generator tuning for the LHC. *Eur. Phys. J.*, C65:331–357, 2010.

[48] C. G. Lester and D. J. Summers. Measuring masses of semiinvisibly decaying particles pair produced at hadron colliders. *Phys. Lett.*, B463:99–103, 1999.

[49] Alan J. Barr, Ben Gripaios, and Christopher G. Lester. Transverse masses and kinematic constraints: from the boundary to the crease. *JHEP*, 11:096, 2009.

[50] T. Aaltonen et al. Search for Anomalous Production of Events with Two Photons and Additional Energetic Objects at CDF. *Phys. Rev.*, D82:052005, 2010.

[51] Particle Data Group. *MONTE CARLO PARTICLE NUMBERING SCHEME*, 2016 (accessed April 21, 2016). http://pdg.lbl.gov/2002/montecarlorpp.pdf.

[52] Robert Schöfbeck. *Update of the cut-based two lepton stop analysis*, (accessed April 30, 2016). CMS Internal Presentation: https://indico.cern.ch/event/491189/contributions/2001591/attachments/1220190/1783420/16-01-29_TBT_OSDL_DilepStop.pdf.

[53] Judith M. Katzy. QCD Monte-Carlo model tunes for the LHC. *Progress in Particle and Nuclear Physics*, 73:141 – 187, 2013.

[54] CMS Collaboration. Measurement of the differential cross section for $t\bar{t}$ production in the dilepton final state at $\sqrt{s} = 13$ TeV. Technical Report CMS-PAS-TOP-16-011, CERN, Geneva, 2016.

[55] CMS Collaboration. Measurement of the inclusive and differential $t\bar{t}$ production cross sections in lepton + jets final states at 13 TeV. Technical Report CMS-PAS-TOP-16-008, CERN, Geneva, 2016.

[56] Peter Skands, Stefano Carrazza, and Juan Rojo. Tuning PYTHIA 8.1: the Monash 2013 Tune. *Eur. Phys. J.*, C74(8):3024, 2014.

[57] Torbjörn Sjöstrand, Stephen Mrenna, and Peter Z. Skands. *Pythia 8 Manual*, 2016 (accessed May 6, 2016). http://home.thep.lu.se/~torbjorn/pythia81html/Welcome.html.

[58] CMS Collaboration. Measurement of $t\bar{t}$ production with additional jet activity, including b quark jets, in the dilepton decay channel using pp collisions at $\sqrt{s} =$ 8 TeV. http://cms-results.web.cern.ch/cms-results/public-results/publications/TOP-12-041/index.html#AddFig, 2015.

[59] ATLAS Collaboration. A study of the sensitivity to the Pythia8 parton shower parameters of $t\bar{t}$ production measurements in *pp* collisions at $\sqrt{s} = 7$ TeV with the ATLAS experiment at the LHC. Technical Report ATL-PHYS-PUB-2015-007, CERN, Geneva, Mar 2015.

[60] Comparisons of Theory Predictions for the $t\bar{t}$ Process with Data from pp Collisions at sqrt(s)= 8 TeV. Technical Report CMS-PAS-TOP-15-011, CERN, Geneva, 2015.

[61] Grados J. and Gunnellini P. *Sensitivity studies of α_S tunes*, (accessed May 20, 2016). CMS Internal Presentation: https://indico.cern.ch/event/524675/contributions/2148836/attachments/1264431/1871218/Approval.pdf.